Федеральное государственное автономное образовательное учреждение высшего образования «Уральский федеральный университет имени первого Президента России Б.Н. Ельцина»

Уральский энергетический институт

Кафедра «Электропривод и автоматизация промышленных установок»

На правах рукописи

Джассим Хайдер Майтам Джассим

СИСТЕМА УПРАВЛЕНИЯ ЭЛЕКТРОСНАБЖЕНИЕМ КРАНОВ-ШТАБЕЛЕРОВ НА ОСНОВЕ МИКРОГРИД

2.4.3 – Электроэнергетика
2.4.2 – Электротехнические комплексы и системы

ДИССЕРТАЦИЯ
на соискание ученой степени кандидата технических наук

Научный руководитель:
доктор технических наук, профессор
Зюзев Анатолий Михайлович

Екатеринбург – 2025

Federal State Autonomous Educational Institution Higher Education «Ural Federal University named after the first President of Russia B.N. Yeltsin»

Ural Power Engineering Institute

Department of «Electric Drive and Automation of Industrial Plants»

As a manuscript

Jassim Haider Maytham Jassim

MICROGRID-BASED POWER SUPPLY CONTROL SYSTEM FOR STACKER CRANES

2.4.3 – Electrical Energy
2.4.2 – Electrotechnical complexes and systems

DISSERTATION
Degree of Candidate of Technical Sciences

Scientific supervisor:
Doctor of Technical Sciences, Professor
Ziuzev Anatolii Michaelovich

Yekaterinburg – 2025

Dedication

I dedicate this work to my family who supported and motivated me throughout my long years of study, and planted hope and optimism in my spirit. To my mother who with her encouragement and prayers, I was able to achieve my ambitions.

Contents

Introduction

Relevance of the research topic. Electric drives of hoist and transport mechanisms (HTM) have specific features that characterize the design of their power supply systems. These features include the multi-motor (up to 3 or more) drive configuration with motors that significantly differ in power rating. They are also distinguished by the nature of their electric motor loads (reactive torque for transverse mechanisms and active torque for hoist mechanisms). Another important feature is the intermittent short-term operation of electric motors with periods of acceleration, deceleration, and steady-state motion in motoring or regenerative modes, in which the drive system's simultaneous operation is highly anticipated. Taking these features into account, the electric drives of these mechanisms are structured as a multi-drive complex, where the main power supply unit is connected to several power converters driving each motor. This structure is considered an element of Smart-Grid or Microgrid systems, integrating various energy sources including local renewable generators and storage devices to ensure uninterrupted operation. This results in an increased efficiency, stability, and reliability of the overall electrical complex. Of particular interest in this regard are energy storage devices, acting as a buffer between energy generation and consumption in the combined electric complex. They prevent interruptions in the supplied power during emergencies, maintenance, and grid blackouts. Additionally, storage devices are utilized to retrieve the regenerated energy in electromechanical complexes. In HTM electric drives, regenerative modes are quite frequent, such that the regenerated energy is considered a renewable source, available directly at the outputs of the drive power converters. Nevertheless, the energy storage devices integration into the power supply system of an industrial complex requires an accurate description of the power system configuration, since it significantly affects the choice of the implemented energy management algorithm in a Microgrid operational scenario. These algorithms regulate the production, storage, and consumption of energy depending on the state of the power grid and the availability of local resources. Optimal energy utilization in such complexes can only be achieved through the effective employment of energy management algorithms that determine the operating modes of the network.

Battery-integrated power supply systems can be used in electric drives of various mechanisms, many of which are used in critical areas of the economy, biological, and military applications, where interruptions are prohibited. However, in this study, hoist and transport mechanisms, like a warehouse robot or a stacker crane, are more

specifically addressed. These mechanisms are widely used to maneuver materials in warehouses, ports, and manufacturing enterprises. Energy is supplied to the electrical complex through power trolleys or a flexible cable, which have low reliability. The electric drive of the hoist mechanism imposes a significant demand on the local electrical grid during lifting mode, which can lead to a deterioration in the electricity quality. In traditional commercial hoist mechanisms, the regenerated energy during load lowering and braking modes is usually dissipated in the braking resistors. The use of batteries or other energy storage devices increases the overall efficiency of the system by recovering this wasted energy. In this study, the power supply system of an automated stacker crane (ASC) is considered as an example.

Constructing a battery-operated power supply involves many aspects and power components that need to be perceived as one holistic solution. However, research in this field either addresses the system-level energy management algorithms or the implementation of power components and controllers. A complete solution requires the fusing of multiple technologies and power converter topologies to perform design objectives. The battery system is structured in a layer arrangement, with each layer representing a particular system component. Energy management controllers operate as the highest layer, supervising the stored energy capacity and administrating the energy consumption and power direction. This layer implement Microgrid regulators that has the capability of interacting with the power grid parameters to control the active and reactive power of the complex. This is followed by two layers concerning the employed power electronic devices and their regulators. These layers physically interact with the chemical battery module, which is regarded as the fourth layer. This research is interested in the development of technologies and possibilities associated with these layers to enable maximum and flexible utilization.

The degree of development of the research topic. Most of the research in the field of power supply of electric drives of PTM is devoted to the development of hybrid power supply systems for port or container cranes, which are proposed to incorporate various energy storage devices to increase the efficiency of the utilized electrotechnical components. Many scientists have made a significant contribution to the development and research of such systems: M. Flynn, D. Iannuz, P. J. Grbovich, M. Antonelli, etc. The research conducted by A. Meneghetti and P. Simeoni discussed the integration of various local energy sources into the power supply system of warehouse complexes. Among the works of Russian scientists devoted to energy storage devices in electric drives, the publications of V. N. Polyakov and Yu. V. Plotnikov stand out. To the extent of our knowledge, the modernization of the power supply of rack stacker cranes of warehouse complexes using microgrid technologies and battery systems has not been considered before. This lack of research led to the selection of an automated warehouse power supply system for stacker cranes with battery integration for further consideration.

The object of the study is the battery-supported power supply system and its related power converters and energy management controllers integrated into HTM.

The goal of this work is to achieve uninterruptible operation of battery integrated power supply system utilized in electric drives of HTM by developing battery system components.

Based on the analysis provided in chapter (1) and to achieve the formulated research goal, **the following tasks are addressed:**

1. Development of energy management regulators for power supply system of electrical complexes operated as grid-tied and islanded Microgrids, dealing with various energy system operational conditions.
2. The research and development of battery charger topology and controllers that minimize switching losses and maximize voltage regulation range.
3. Development of a real-time battery emulator based on the lithium-ion battery model for testing and validation purposes of battery system components and related technologies.
4. Development of uninterruptible, efficient, and environmentally friendly power supply system for hoist and transport mechanism, working with local energy generators and dealing with various operational conditions.

Provisions Submitted for Defense:

1. Automatic control algorithms for the power supply of HTM electric drive systems, and recommendations for their implementation to ensure the efficient exploitation of accumulated, generated, and recovered energy in the electrical complex.
2. Topology and parameters of the wide-range LLC resonant converter for a battery charger with phase control, allowing the integration of variety battery capacities with different voltage ranges into the proposed power supply system. Compared to other topologies, this converter provides the proposed power supply system with operational flexibility depending on changes in the operating conditions of the electrical complex and customer requirements.
3. The structure of software and hardware real-time battery system emulator, created based on PHiL simulators principles. The test bench is characterized by its energy efficiency and the reconfiguration simplicity of the battery model parameters.
4. The battery-supported power supply system for electric drives of an automated warehouse stacker crane complex, ensuring uninterrupted operation, increased efficiency, and the ability to integrate various local renewable energy sources without sacrificing performance.

Scientific Novelty of this work:

1. Scientific based recommendations on the energy management regulators selection for power supply of automatic stacker crane complex, working as Microgrid in grid-tied and islanded operational conditions. The recommended energy manage-

ment regulator was selected based on the local generators level of availability, the warehouse size and configuration, and the energy station's requirements.

2. Methodology and implementation of a wide regulation range DC-DC resonant converter working with phase shift controller for battery charging application. This topology allows the proposed power supply system to integrate various battery capacities and chemistry while maintaining minimum switching losses.
3. Methodology for synthesizing power components and regulators of a real-time battery emulator based on PHiL technology. The proposed emulator is characterized by its safety, efficiency, and the simplicity of battery parameters adaptation.
4. The battery-integrated power supply system structure of warehouse-based hoist and transport mechanisms, ensuring efficient and uninterrupted operation in islanded and grid-tied Microgrid modes. Based on the availability of local renewable energy resources and the conditions of the power system, the modernized power supply system maintained performance of warehouse complex regardless of changes on the supply side of the power grid.

The degree of reliability of conducted studies results is confirmed by the coincidence of modeled and experimental data obtained on a laboratory Testbench for testing battery chargers, and the oscilloscope data of different operational scenarios in an experimental stacker crane.

The theoretical significance of this work consists of developing battery models in various environments, which allows the comprehension of chemical battery power interactions. Furthermore, this work involved the development and simulation of battery-integrated stacker crane drive systems and their related speed control algorithms which play an important role in the future development of the crane complex. The research also addressed the development and study of various energy management regulators that tackle different external and internal influences and operational modes of electrical complexes. The implementation of these regulators is not limited to the hoist and transport mechanisms but can be employed in numerous technical applications.

The practical significance of this work consists of developing a battery system emulation testbench. This device is utilized to safely test and validate newly designed battery-related technologies like battery managers and chargers. Furthermore, the developed power supply system for automated stacker cranes was proposed as an application example of hoist and transport mechanisms, which enable the integration of various distributed renewable and non-renewable generators into the warehouse complex. The proposed solution was adopted by the advanced development department of "Rukhlo" company, for further implementation in the power supply system of newly designed warehouse complexes. Practical measurements and parameters of the actual stacker crane system were collected for validation, justification, and design establishment.

Methodology and research methods: in this work, experimental and theoretical methods were employed to execute the established tasks and achieve the required

goal. The theoretical methods included provisions related to the theory of electric drive, automatic control system theory, power system and distribution network, renewable energy and Microgrids, numerical integration methods, and the metaheuristic optimization techniques. On the other hand, experimental methods included: computer modeling and analysis of power systems and components, implementation of dynamical real-time systems in different environments, and the development of power converters as power system components and for emulation purposes. LABVIEW 8.0, MATLAB 2022a, and STM32CubeIED programs were used in the practical part of this research.

Conformity of the dissertation to the specialty 2.4.2 "Electrotechnical complexes and systems": The content of the dissertation fully complies with the following points of the specialty passport: point 1. "Development of the general theory of electrical engineering complexes and systems, analysis of system properties and relationships, physical, mathematical, simulation and computer modeling of components ...., electromagnetic energy converters ....., power supply ..."; point 2. "Development of scientific foundations for the design, creation and operation of electrical engineering complexes, ..."; point 3. "Development, structural and parametric synthesis, optimization of electrical engineering complexes, systems and their components, ..."; point 4. "Study of the performance and quality of functioning of electrical engineering complexes, systems and their components in various modes, at ...".

Conformity of the dissertation to the specialty 2.4.3 "Electrical Energy": The content of the dissertation fully complies with the following points of the specialty passport: point 9. "Optimization of the structure, parameters..., mini- and Microgrids"; point 10. "Development of digital and physical methods... and power supply systems"; point 11. "Development of methods for monitoring and analyzing regime..., mini- and Microgrids"; point 16. "Development of methods for analyzing and synthesizing automatic control systems,... in the electric power industry".

The author's personal contribution consists of active participation in the development of all practical and theoretical components of this research work and their resulting publications. The author participated in the theoretical development of and analysis of the proposed Wide range LLC resonant converter. Furthermore, the author participated in the theoretical and practical implementation of the proposed battery emulator testbench and associated developed real-time models.

Implementation of the research results: the results were accepted as possible extension and modification of the work being conducted by ООО "РУХЛО"(г. Екатеринбург) crane system manufacturer.

LIST OF SCIENTIFIC PAPERS PUBLISHED ON THE TOPIC OF THE DISSERTATION

Articles published in peer-reviewed scientific journals accepted by the Higher Attestation Commission of the Russian Federation and the Ural Federal University

Attestation Council:

1. Джассим Х.М. Управление гибридной микросетью с использованием оптимизированного контроллера поддержки сети / Джассим Х.М., Зюзев А.М., Крюков О.В. // Вестник МЭИ. –2023. № 5. –С. 11—19. (0.88п.л./0.6п.л.)
2. Jassim H.M. Fuzzy management controller for autonomous power supply system based on active neutral multilevel inverter / Jassim H.M., Ziuzev A.M. // Perm National Research Polytechnic University Bulletin. Electrotechnics, information technologies, control systems. –2023, № 45 –pp. 5-30. (0.89п.л./0.66п.л.)
3. Jassim H.M. Topologies and Technologies of Electric Vehicle Fast Charging Station: Review and Comparison / Jassim H.M., Ziuzev A., Kostylev A., Mudrov M., Khabarov A. // Perm National Research Polytechnic University Bulletin. Electrotechnics, information technologies, control systems. –2023, № 46, –pp. 5-46. (1.58п.л./1п.л.)
4. Jassim H. M. Power hardware-in-loop emulation of a battery for charging systems and grid applications / Haider M. Jassim, Anatolii Ziuzev, Mikhail Mudrov // Bulletin of the Tomsk Polytechnic University, Geo Assets Engineering. –2024, –Vol. 335, № 4, –pp. 200-211. (0.84п.л./0.7п.л.). (Scopus, Wos) Q3
5. Джассим Х.М. Гибридная система электроснабжения электроприводов кранаштабелера / Джассим Х.М., Мудров М.В., Зюзев А.М. // Электротехнические системы и комплексы. –2024. № 2(63).– С. 34-44. (0.89п.л./0.7п.л.)К2
6. Коптяков А.С. Проектирование и построение резонансного преобразователя LLC с широким диапазоном напряжений для быстрой зарядки электромобилей / Коптяков А.С., Джассим Х.М., Зюзев А.М., Сарапулов С.Ф. // Вестник Пермского национального исследовательского политехнического университета. Электротехника, информационные технологии, системы управления. –2024, № 51, –С. 149–175. (0.9п.л./0.4п.л.)К2

Patents and Certificates of Program Registrations

7. Эмулятор аккумуляторной батареи в реальном времени / Зюзев Анатолий Михайлович, Джассим Хайдер Майтам Джассим, Мудров Михаил Валентинович// Свидетельство о гос. регистрации программы для ЭВМ; УрФУ. № 202461-2062, Дата публикации и номер бюллетеня: 29.01.2024 Бюл. № 2.
8. Эмулятор аккумуляторной батареи на базе микроконтроллера STM32 / Зюзев Анатолий Михайлович, Джассим Хайдер Майтам Джассим, Вакорин Никита Иванович, Мудров Михаил Валентинович //Свидетельство о гос. регистрации программы для ЭВМ; УрФУ. № 2024662960, Дата публикации и номер бюллетеня: 03.06.2024 Бюл. № 6.
9. Устройство для испытаний полупроводниковых преобразователей зарядных устройств аккумуляторных батарей / Зюзев Анатолий Михайлович, Джассим Хайдер Майтам Джассим, Мудров Михаил Валентинович // Патент на изобретение; УрФУ. № 2837554, Дата государственной регистрации: 01.04.2025.

10. Ziuzev A. Power Hardware-in-Loop Implementation for Power Grids and Devices: Report and Review / A. Ziuzev and H. M. Jassim // 2021 XVIII International Scientific Technical Conference Alternating Current Electric Drives (ACED), Ekaterinburg, Russia. –2021, –pp. 1-6. (0.66п.л./0.46п.л.)
11. Jassim H.M. Optimized-Fuzzy Droop Controller for Load Frequency Control of a Microgrid with Weak Grid Connection and Disturbances / H. M. Jassim and A. Ziuzev // 2022 29th International Workshop on Electric Drives: Advances in Power Electronics for Electric Drives (IWED), Moscow, Russian Federation. –2022, –pp. 1-7. (0.76п.л./0.52п.л.)
12. Jassim H.M. Dual Droop-Based Controllers for Hybrid Microgrid with Photovoltaic and Wind Turbine Distributed Generators / H. M. Jassim and A. Ziuzev // 2022 International Ural Conference on Electrical Power Engineering (UralCon), Magnitogorsk, Russian Federation. –2022, –pp. 417-422. (0.69п.л./0.49п.л.)
13. Jassim H.M. Analyzing G2V and V2G Functionalities for Electric Vehicle Charging Station / H. M. Jassim, A. Zyuzev and S. Valtchev // 2022 4th International Conference on Control Systems, Mathematical Modeling, Automation and Energy Efficiency (SUMMA), Lipetsk, Russian Federation. –2022, –pp. 884-890. (0.74п.л./0.58п.л.)
14. Jassim H.M. Control of Grid-tied Three-level Four-leg Inverter Using Sliding Mode Controller Based on Fryze Current Minimization Technique / H. M. Jassim and A. Zyuzev // 2023 Russian Workshop on Power Engineering and Automation of Metallurgy Industry: Research & Practice (PEAMI), Magnitogorsk, Russian Federation. –2023, –pp. 124-129. (0.78п.л./0.54п.л.)
15. Jassim H.M. Supervised Grid-supporting Droop Controllers for Islanded Microgrid Operated by Scattered Parallel Inverters / H. Jassim, A. Zyuzev and A. Kostylev // 2023 XIX International Scientific Technical Conference Alternating Current Electric Drives (ACED), Ekaterinburg, Russian Federation. –2023, –pp. 1-6. (0.66п.л./-0.5п.л.)
16. Jassim H.M. Supervised Droop Controller Based on Virtual Synchronous Generator for Islanded Microgrid / H. M. Jassim, P. Pustokhin and A. Zyuzev // 2023 5th International Conference on Control Systems, Mathematical Modeling, Automation and Energy Efficiency (SUMMA), Lipetsk, Russian Federation. –2023, –pp. 1070-1075. (0.61п.л./0.46п.л.)
17. Pustokhin P. VSM for Microgrid on the Compressor Stations / P. Pustokhin, H. M. Jassim and A. Zyuzev // 2023 Russian Workshop on Power Engineering and Automation of Metallurgy Industry: Research & Practice (PEAMI), Magnitogorsk, Russian Federation. –2023, –pp. 155-159. (0.34п.л./0.14п.л.)
18. Jassim H.M. Investigating the Operating Principles of Vehicle-to-Vehicle Charging / H. Jassim, M. Mudrov and A. Khabarov // 2023 XIX International Scientific

Technical Conference Alternating Current Electric Drives (ACED), Ekaterinburg, Russian Federation. –2023, –pp. 1-6. (0.66п.л./0.55п.л.)

19. Jassim H.M. Hybrid Solar-Based Power Supply for a Stacker Crane System / H. M. Jassim, M. Mudrov and A. Zyuzev // 2024 International Conference on Industrial Engineering, Applications and Manufacturing (ICIEAM), Sochi, Russian Federation. –2024, –pp. 299-304. (0.61п.л./0.45п.л.)
20. Jassim H.M. Fuzzy Management Control of Line-to-Line Power Transfer in Automated Warehouse Application / H. M. Jassim, et al // 2024 International Ural Conference on Electrical Power Engineering (UralCon). –2024, –pp. 299-304. (0.74п.л./0.53п.л.)

Structure of the dissertation: this research consists of five chapters and seven indexes. The dissertation volume is 165 pages, including the introduction and conclusion parts. It contains 101 figures and 8 tables, and 135 references. While the indexes contain 25 figures.

Chapter 1

Analysis of Power Supply Systems for Hoist and Transport Mechanisms

Hoist and transport mechanisms include various applications and material-handling devices like cranes. These mechanisms are employed in maneuvering heavy loads in industry branches: paper and cement, and metallurgy. Energizing these complexes requires an intensive and stable source of energy. For reliable operation, their power supply can not be compromised during grid weakening events or maintenance periods. The utilized power supply system is required to integrate a wide range of distributed generators including renewable sources to reduce the environmental effects of such applications and enable energy autonomy. Compensating for the intermediate nature of the distributed generators and the inconsistency of their generation rates involves employing energy storage devices like battery systems. These systems include several technical layers that ultimately control the stored energy and the direction of supplied power. These systems are, also, essential for retrieving the regenerated energy available during the braking mode of the mechanism electric drive systems. The baseline understanding of battery systems covers multidisciplinary research and stockholders. Unfortunately, studies in this field lack a comprehensive view of addressing battery systems on the component level and system architecture level[1]. Figure 1.1 demonstrates the different layers and technologies involved in the battery-supported power supply system. On the generation side of the figure, power converters (PC) are employed to supply the energy. While control elements (CE) are used to regulate loads. Although it concurs with the categorization illustrated by [1; 2], the structural organization of the proposed battery system is functionally different due to the specificity of the addressed application. In this chapter, a comprehensive review of battery system technological parts is provided as individual elements to fully grasp their basics. This assists in the later development of these layers and technologies to configure the integrated power supply system. Furthermore, technological methods and applications utilized in this research are also reviewed.

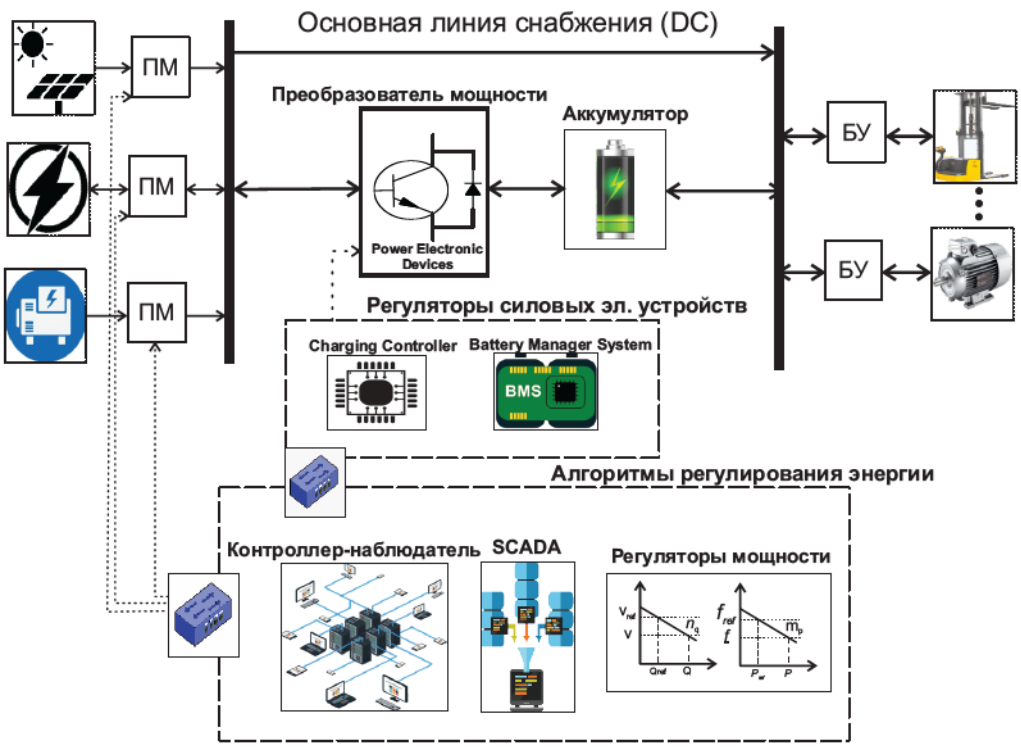

Figure 1.1: Battery-based power supply system operating technical complex.

1.1 Hoist and Transport Mechanisms

Hoist and transportation mechanisms are categorically addressed in this research because of their diverse applications and encouraging properties. Electromechanical systems employed in these mechanisms freely offer regenerated energy to be harvested and utilized [3]. This will significantly increase the efficiency of these applications and reduce operational costs.

1.1.1 Application of Energy Storage in Hoist Mechanisms

Many applications are classified under these mechanisms including overhead cranes, stacker cranes, forklifters, automatic stacking and retrieval devices, gantry cranes, industrial and residential lifts, and ship-to-shore cranes. Decentralized energy storage devices for urban areas based on lift mechanisms regenerated energy was proposed in [4]. The research conducted a full-scale analysis of the available regenerated energy in megacities like Moscow and New York where average buildings are higher than in other cities. The research found that, in developed countries, lift mechanisms alone can supply free energy up to tines of gigawatts. Furthermore, a study established the economic benefits of integrating energy storage devices into various crane configurations in Port Gävle, Sweden [5]. Ship-to-shore cranes among the studied systems showed the highest recoverable energy of (400kWh) during peak hours and with maximum payload and efficiency. These arguments instituted the urgency for extensive study and devel-

opment of battery systems, and their large-scale adoption in hoist-utilizing industries. Flywheel energy storage devices were employed to provide peak power and retrieve the dissipated energy during the braking mode of harbor cranes[6–8]. Their high power density and long life span, allow them to be economically viable for large crane complexes. Ultra-capacitors (UC) and super-capacitors (SC) can provide a rapid burst of power to decrease the demand of the crane complex during acceleration and hoist-up operations. They have been employed to reduce the energy cost or fuel consumption of large cranes and absorb the regenerated energy during hoist-down mode [9–11]. For supporting longer operational periods, battery systems like Li-ion batteries are exploited for RTG and STS crane types[12; 13]. Similar to UCs and SCs, battery systems can provide energy during peak load acceleration. Moreover, they can supply the crane systems for extended periods, especially at peak hours when the price of electricity is soaring.

1.1.2 Automated Stacker Crane

Transportation and material maneuvering operations are considered one of the significant energy consumers in warehouse applications [14]. Renewable energy generator integration into the warehouse complex can reduce the energy consumption and the associated costs by more than 20% when proper utilization and optimal management algorithms are applied [15]. Integration of automated stacker crane systems can enhance the reliability and productivity of the storage facility by minimizing human interactions. Figure 1.2 demonstrates the basic mechanical configuration of the stacker crane system. It is required to synthesize an automated hybrid power supply system for such devices to ensure the sustainability of the stacking and retrieval process, and maintain productivity. Solar energy is the most suitable candidate for warehouse application due to the abundant rooftop space available in these installations [16]. By employing energy storage devices like battery systems, the crane's complex powering process can continue during renewable fluctuation periods. The integrated battery system can also recover the regenerated energy during load-lowering and drive braking modes, which increases power efficiency. As a result, the braking resistors and related converters are eliminated reducing device development costs. A group of stacker cranes operated in a warehouse exchanging power with the grid and energy storage devices is a well-established application of a Microgrid management system where each crane is considered a mini-Microgrid. Unfortunately, the literature is scarce in that regard with little focus on the performance of such an electrotechnical complex. Consequently, in this research, the developed technologies for battery-based power supply systems are implemented in automated stacker cranes as a case study.

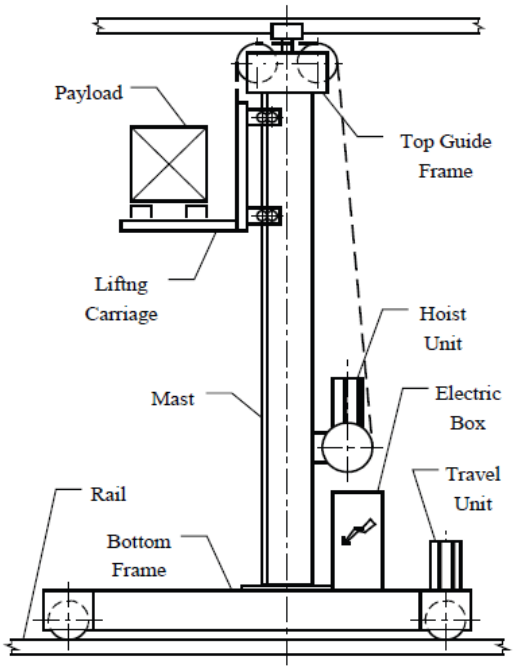

Figure 1.2: Stacker crane configurations[17].

1.2 Prospects of Renewable Distributed Generators

The majority of Russian energy production is from nonrenewable sources. However, since Russia signed the Paris Climate Agreement in 2016, the Russian energy sector has been diversified to presently include (17,8%) of renewable energy sources. The renewable energy market share was increased 10 times over the last 20 years by the Russian government to achieve the (10%) total installation capacity target by 2040 [18]. According to [19], the industrial sector accounted for (67.81%) of greenhouse gas emissions in Russia in 2019, especially in extensively industrialized regions like the Sverdlovsk. Increasing small-scale renewable generator integration to achieve environmental safety is one of the essential targets of the Sverdlovsk regional government. Thus, the incorporation of these generators in the industrial complexes became a necessity. A variety of renewable sources contenders can be integrated into large and medium size power consuming complexes with an expected reduction in peak demand. These sources include hydropower, biomass, solar, and wind. In 2020, 1 GW of solar and wind energy generators were integrated into the Russian energy production sector, which emphasizes the achievable capacity and the subject significance. In the Sverdlovsk region solar energy lack sustainability during autumn and winter periods due to the reduced irradiation hours. Nevertheless, solar panels can still be considered as a viable small-scale generator for industrial applications [19]. Furthermore, by taking the Ural region as a whole into account, the southern cities and provinces appear well within the medium-range annual solar irradiation, which makes them more suitable for wider solar energy adoption [18]. However, wind generators have encouraging prospects for wider integration, considering that the Sverdlovsk region has the capacity to produce around 200

MW of power from wind farms [19]. Therefore, renewable distributed generators incorporation into the power supply of electrical complexes has been well-established and justified. The utilization of these sources and the regenerated energy from hoist mechanisms can increase energy efficiency and reliability.

1.3 Microgrid and Energy Management

A Microgrid is a collection of power generators and loads operated as subsections of the power grid and controlled separately [20]. This unique architecture was proposed to mitigate ecological and economic issues related to power grid operation by facilitating the integration of locally distributed generators [21]. Energy storage devices are essential elements in Microgrids that assist in matching local generation and consumption rates. This offers the opportunity to operate the Microgrid in an islanding mode which seems economically efficient for industrial applications, especially during peak hours. The stored energy becomes the solitary source energizing the loads when renewable generators experience fluctuations. The stored energy could also be injected into the power grid to perform grid services like peak-shaving, frequency, and reactive power regulations [22]. Microgrid installation has also gained importance for remote and military-type applications due to their resilience and offered reliability [23; 24]. The Microgrid represents the energy management layer in the battery system which regulates the absorbed and discharged energy of the battery. Moreover, as seen in Figure 1.1, they are also responsible for controlling the supplied energy by power converters. This indicates that Microgrid controllers have a high-level operation that supervises the energy exchange of the entire electrical complex. The next sections discuss types of Microgrid operations and special controllers used for energy regulation.

1.3.1 Grid-tied Microgrid

This type of Microgrid is more common in residential and large industrial applications. From a utility perspective, Microgrids have the role of stabilizing load profile while minimizing the excessive utilization of massive power turbines in regulating frequency changes occurring over the grid [25]. On the other hand, the demand side can integrate a variety of local generators that reduce energy costs and attract incentives. Grid-tied Microgrids are hybrid in nature since they encapsulate various AC and DC resources. The power-sharing between two sides of the grid is regulated by a bidirectional interlinking converter (BIC). It manages the extraction of energy from distributed generators and its injection into the demand complex [26; 27]. Therefore, the proper regulation of this converter can ensure AC power balance and the prevention of ripple injection into the DC bus [28]. The studied topology and application of the converter largely affect the choice of control mechanism. For instance, an active power damping

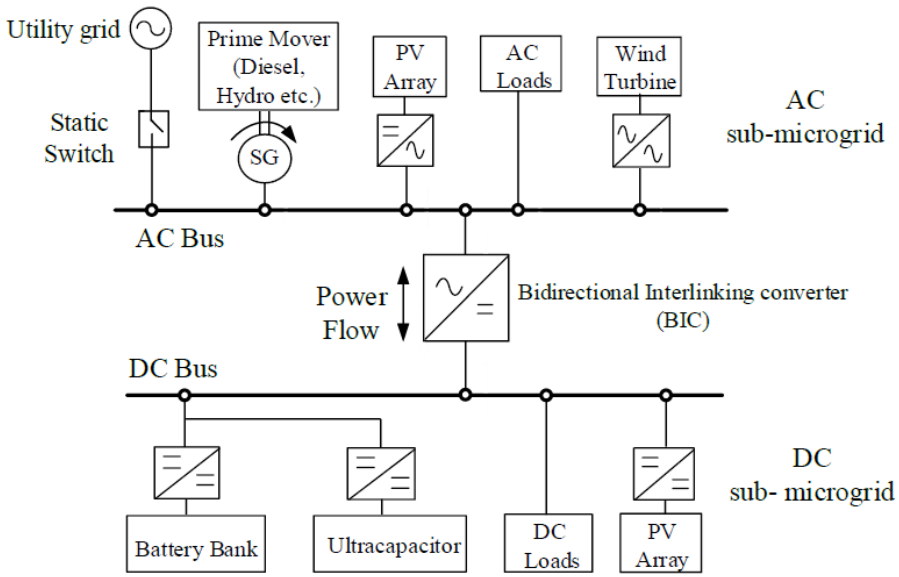

Figure 1.3: Typical grid-tied Microgrid with interlinking converter[30].

controller was employed to control a three-phase SPWM converter to achieve harmonic reduction[28], while a nonlinear model-predictive controller was proposed to ensure power-sharing and frequency regulation between distributed sources with disturbances [29]. Figure1.3 illustrates the concept of a grid-tied Microgrid with distributed generators. Based on the BIC control targets, energy may be extracted from one side and injected into the other side for load regulation.

As previously emphasized, battery systems are an essential part of Microgrid applications. Many research articles addressed the utilization of battery resources for DC sub-grid resource management [31–33]. These research studies were motivated by the ever-growing interest in DC applications like fast electric vehicle chargers and distributed lighting systems. The control targets are shifted from supporting the power grid operation to maintaining functioning DC side resources. In some scenarios, the DC side of the grid is isolated from the AC side when extensive depletion of battery resources to regulate the AC grid jeopardizes the operation of some critical DC loads [25]. Finally, Grid-tied Microgrid application into the hoist and transport mechanisms has been well-established in the literature. The hybridization of Rubber Tyre Gantry (RTG) crane energy supply was proposed to mitigate the rapid and significant increase in the demand profile during hoist-up operations that reduced power quality at industrial sites [10; 13].

1.3.2 Islanded Microgrid

The combination of distributed generators with battery systems allowed the autonomous operation of certain electrical complexes based on the available resources. The centralized power system architecture is replaced by a distributed generator-based

scheme that utilizes renewable generators like solar and wind energy to increase the sustainability and reliability of the power system [34]. This new architecture, which is operated in isolation from the power grid, is called Islanded Microgrid. It has a similar concept to the autonomous power supply (APS) systems that are used for uninterruptible critical and remote applications [35]. The visualization of this Microgrid is quite similar to the grid-tied configuration demonstrated in figure1.3 except for the obscene or disconnection of the main grid. Many articles address different combinations of local generators, but all of them utilize energy storage devices like battery systems and super-capacitors to sustain the load complex during generation degradation periods [30; 36]. Some practical studies of islanded Microgrid implementation to hoist mechanisms, including crane systems, are proposed in the literature. These studies, more precisely, addressed the utilization of fuel cells, battery systems, and local diesel generators to reduce energy consumption and increase the efficiency of large container cranes [37; 38].

1.3.3 Droop Controllers

Regardless of the Microgrid operational mode, there are prerequisites for stable and effective operation of the generator-load complex. These include voltage and frequency regulation, proper power-sharing, synchronization with the main grid, optimizing operational cost, and proper regulation of internal and external events [39]. Thus, it is imperative to use a hierarchical control structure that has the capability of reacting on different levels to regulate voltage and frequency based on active and reactive power control [40; 41]. Droop controllers have an inherent hierarchical structure that requires minimal communication with other regulators in the vicinity. Their reaction is purely based on the local measurements and the provided droop gain parameters. The three levels of such cooperative structure regulating the Microgrid response are shown in the figure. The primary control mechanism regulates voltage (V) and frequency(ω) on the distributed generator level, while the secondary mechanism is tasked with regulating deviations caused by the primary level in a centralized manner. The tertiary controller operates to optimize the overall power interaction of the Microgrid and addresses economic concerns of energy utilization. The equations 1.3.1 and 1.3.2 represent the basic droop relationships that are required to be realized by the droop controller[39]:

$$V = V_{ref} - n_q * Q \tag{1.3.1}$$

$$\omega = \omega_{ref} - m_p * P \tag{1.3.2}$$

P represents the active power while Q is the reactive power. Droop gain parameters n_q and m_p represent the slop of active and reactive power deviations from nominal values. These linear parameters could be extended to sophisticated mechanisms based

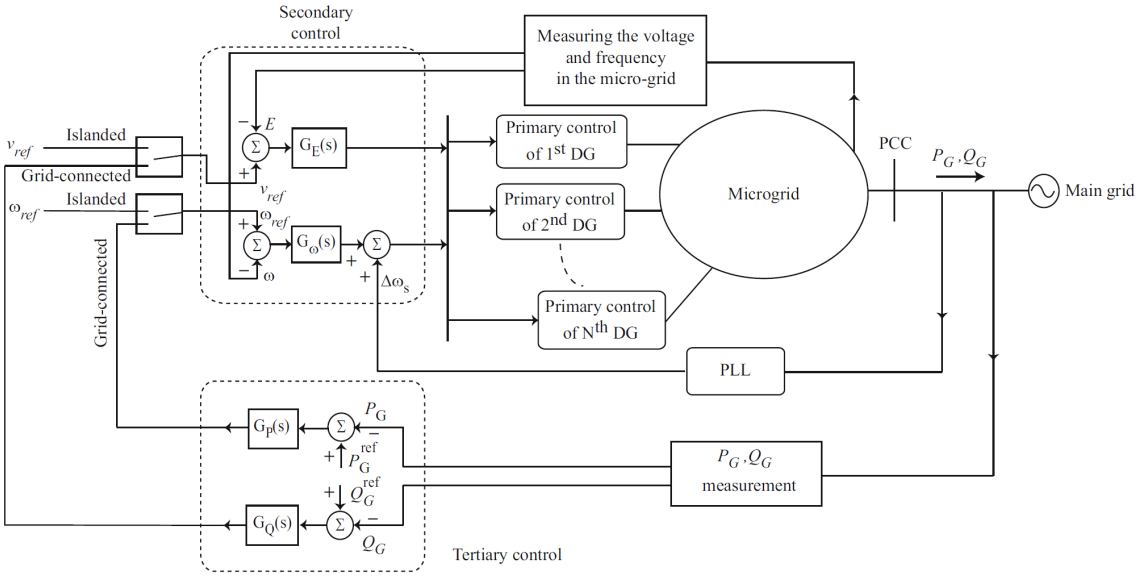

Figure 1.4: The three levels of Microgrid Controllers[42].

on the required performance and available computational capabilities. However, the target of these controllers is to regulate the power converter interlinking the distributed generator to the Microgrid[32; 43; 44].

1.3.4 Intelligent Controllers

Intelligent algorithms have been gaining considerable interest in recent years due to the introduction of more computationally capable microelectronics. Applications of these algorithms extended from enhancing the performance of typical controllers to system-level optimization and organization. In the Microgrid field, significant research is conducted based on intelligent methods to improve efficiency and maximize profits. A certain direction of research considers the Microgrid as an inertial-based transfer function that describes the load frequency interactions [45–47]. The objective of this direction is to mitigate the frequency deviations with the utilization of intelligently modified controllers. However, it is considered an oversimplification of the Microgrid problem that disregards important factors like power interactions and voltage regulations [25]. Another direction is to utilize these methods directly into the control loop of distributed generators connected to droop-operated Microgrid[48]. This may be convenient for known generator dynamics, but less useful in general situations. Some intelligent optimizer methods are employed in off-line management and optimization of Microgrid parameters [49; 50]. While other algorithms like fuzzy logic can deal with physical-current measurements to optimize the decision-making process of energy management systems [51; 52].

1.3.5 Virtual Synchronous Generators VSG

Load-frequency regulation in an islanded Microgrid is a problematic issue due to the lack of inertia, which is normally induced by mechanically rotating power turbines in grid-tied operation. For this reason, an inertial compensation element is required to emulate the functionality of power turbines. This is the basic concept of virtual synchronous generators where a distributed generator-connected power converter is controlled to imitate the behavior of synchronous machine and regain inertial response. The application of this concept is not particular to the islanded Microgrid but also extended to enhance frequency stability and eliminate power oscillations in grid-tied configurations [53]. Energy storage devices like battery systems and super-capacitors are usually employed as the distributed generator for such implementation due to their high dynamic response that assists in minimizing transient energy consumption [54]. Nevertheless, this method is customarily combined with other control strategies like distributed droop controllers to improve dynamic performance and power-sharing [55]. The principle dynamics of the VSG are based on the swing transfer function of the synchronous generator.

$$\omega_{rotor} = \omega_0 + \frac{(P_m - Pe)}{J * \omega_0 * S + D} \tag{1.3.3}$$

where ω_{rotor} is the rotor rotational frequency,W_0 is the nominal-rotational frequency, P_m and P_e are the generator output power and active measured power respectively. The parameters J and D are the mechanical inertia and damping of the emulated generator. Then, by integrating the ω_{rotor} we obtain the machine rotational angle θ. This angle is used in the formation of the three-phase virtual voltages of the generator with an amplitude of E.

$$V_{abc} = E * \sin(\theta * t - \theta_0) \tag{1.3.4}$$

1.4 Battery Charging Stations

These stations are represented by power electronic devices that administrate the charging process of chemical batteries. The topology of the employed charging station depends on the battery capacity and the addressed application. For instance, the electric vehicle charging station of the Tesla Model X has a fast-DC charging capability that can deliver up to (200kW) of charging power [56]. However, battery chargers are usually structured as two consecutive converters: an AC/DC rectifier and a DC/DC converter. The rectifier supplies a stable DC voltage and current, while the DC/DC converter regulates the injected power into the battery depending on the battery manager and charging controller. There is an outstanding number of regulations and standards

for battery charger construction and implementation. They set must-adhered specifications to designers like power factor, systems efficiency, maximum leakage current, total harmonic distortion (THD) on the AC side, and many others [57]. This section addresses the topologies of battery charging stations along with their design challenges. It also addresses new technologies and emerging trends in the charging stations field.

1.4.1 AC/DC Power Converters

This power device is responsible for maintaining stable DC power supplied to the next stage of a charging station. Single and multiple-stage rectifiers can be employed in this stage to achieve the required performance and power [58]. Nevertheless, grid operators typically require the integration of power electronic devices that produce less than (5%) of THD in order not to affect other devices connected in the vicinity [59]. This largely limited the employed topologies to the ones with power factor correction capabilities. Active front end (AFE) and Vienna rectifiers are the most distinguishable selection of manufacturers due to their offered efficiency, high power density, and controllability. Figure 1.5 demonstrates the elementary configuration of these two converters. With proper design of pre- and post-filters, the AFE can function as a buck-boost converter transferring the power bi-directionally. This property is missing in the typical design of Vienna converters that require certain topological modifications to be implemented [60]. The AFE suffers from problems related to high switching stress, which can be alleviated by increasing the number of switches[61]. In general, Vienna rectifiers can achieve an astonishing efficiency of (99.2%) [62] with sophisticated topologies and controllers, while AFE can accomplish low voltage ripple and reduced THD using proper control techniques [63].

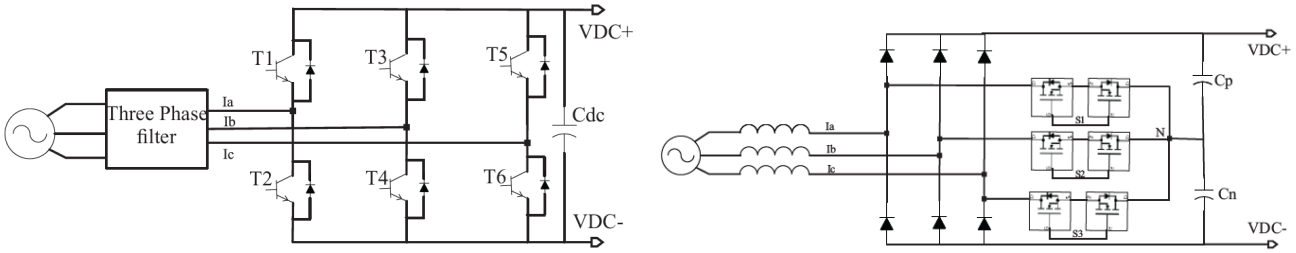

Figure 1.5: Commonly used AC/DC topologies.

1.4.2 DC/DC Power Converters

These converters regulate the delivered voltage and current to battery terminals. They are normally associated with high-precision controllers and high switching-frequency devices. The proper control and implementation of this stage are crucial for a safe and

effective charging process. Design requirements for these converters may include a wide range of voltage regulations, reduced switching losses, high efficiency, and attenuated voltage and current ripples [56]. Unlike the previous stage, numerous DC/DC topologies are available for charging station application each with a unique advantage. The LLC resonant converters are the most widely used topology because of their wide output voltage range, zero voltage switching (ZVS), and relatively high efficiency [64; 65]. The output of the converter is regulated by manipulating the transistor switching frequency near the resonant frequency which is determined by the resonant tank design. Another topology is the phase-shift converter which is associated with features like design simplicity, soft switching capability, reduced current stress, and low electromagnetic interference [66]. The converter is controlled by regulating the phase difference between the two legs of the input bridge while maintaining constant frequency. However, this topology suffers from non-ZVS operation at light loads which limits its efficiency [67]. Figure 1.6 shows the basic configuration of the previously discussed converters. It can be observed that both topologies utilized high-frequency transformers for galvanic isolation which is a design requirement to prevent electrical shocks [56]. Moreover, both converters lack the bidirectional power flow capability. For a bidirectional operation, the output diode bridge of the phase shift converter is replaced with transistors which produces an entirely new type of converter called dual active bridge (DAB) [68; 69].

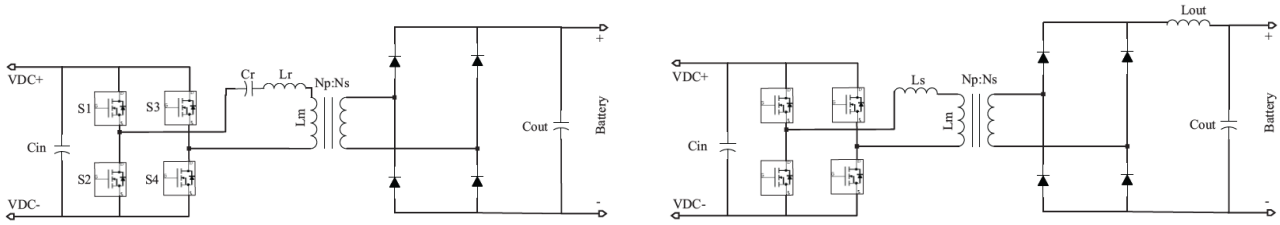

LLC resonant converter

Phase shift converter

Figure 1.6: DC/DC converter topologies.

1.4.3 Battery Charging Methods

The charging process must be carefully conducted to preserve battery cell internal electrochemical reactions and maintain the battery's state of health (SoH) [70]. An optimal method can safely and efficiently charge the battery pack without damaging internal cells. The constant current-constant voltage (CC-CV) method splits the charging profile into two operational regions. A battery current controller is deployed during the first region, while the voltage controller is invoked when a cut-off cell voltage is reached [71]. For faster charging processes, a time-pulsed charging method is utilized by injecting precisely timed voltage pulses into the battery with variable widths. This method guarantees the neutralization of ions during reset periods, which assist in the

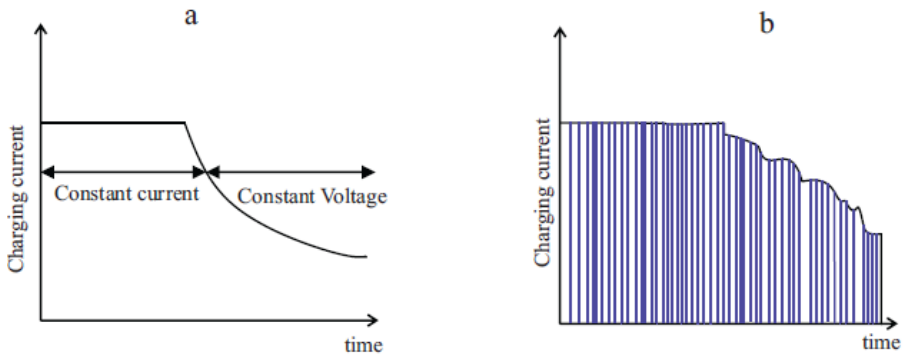

Figure 1.7: Battery charging methods.

deceleration of the polarization process and achieving enhanced battery life cycle [72]. The principles of these charging methods are illustrated in figure 1.7 where pattern (a) represents the (CC-CV) charging profile while pattern (b) represents the pulsed charging profile.

1.4.4 Hard and Soft Switching

Hard switching is one of the most significant issues in battery charger design. During the switch transition, the output current I_L falls with a linear rate instead of immediate change. The output voltage of the power transistor V_{ds} starts to gradually increase at the same time, which means switching losses occur during the transition period. They can be calculated according to the following equation [73]:

$$P_{Losses} = \frac{1}{2} * V_{ds} * I_L * T_{on} * f_{sw} \tag{1.4.1}$$

Several approaches have been proposed to mitigate this serious problem. One approach is to employ an auxiliary circuit causing voltage and current shifts, which reduces the possibility of their intersection [73; 74]. Another solution is to incorporate a snubber circuit around the power switch, which reduces the voltage across its terminals and ultimately minimizes losses[75]. Finally, the previously discussed resonant converters can inherently accomplish soft switching when they operate around the resonant frequency. However, limitations of output voltage regulation range, especially in light-load conditions, are experienced. For enhancing the efficiency of battery chargers, this topic remains an active field of research [76].

1.4.5 V2G and V2V technologies

The random charging of battery farms may result in reducing grid stability, degrading power quality, deteriorating system reliability, frequency and voltage deviations, and increasing load-profile peak demand [77]. Advanced technologies like vehicle-

to-grid (V2G) and vehicle-to-vehicle (V2V) can alleviate these issues by enabling multi-directional power flow [78–80]. Although these technologies address the transfer of power between an electric vehicle's battery system and other entities, they could be generalized for any power-exchanging battery-on-grid complex. The transferred power can be employed to perform grid services or simply reduce the extracted energy from the grid, causing grid-quality improvement. These technologies become more valuable as the size of the energy storage capacity increases or renewable energy sources are integrated [81]. However, power operator regulations and the immaturity of these technologies are still barriers preventing their wide adoption in power systems.

1.5 Battery Managers and Charging Controllers

Cells monitoring and balancing, faults diagnosis and health prediction, thermal management, and state estimation are some of the commercially available battery manager features [82; 83]. These devices operate on a high-level observation and control to administrate the charge and discharge processes of the battery system without damaging battery cells or degrading their SoH. On the other hand, charging controllers are commissioned to control the charging voltage and current. They operate under the administration of battery managers to regulate the supplied voltage level and the injected current. These controllers are divided into AC/DC and DC/DC control algorithms, regulating each power converter. Figure 1.8 demonstrates the configuration of commonly employed AC/DC rectifiers. The AFE uses a control mechanism based on the *dq*-frame to regulate the voltage and current. More advanced structures were proposed in the literature to achieve unity power factor and enhanced dynamic control [84; 85]. The Vienna rectifier controller utilizes the current hysteresis method combined with voltage balancing to boost response time and eliminate steady-state errors [86; 87].

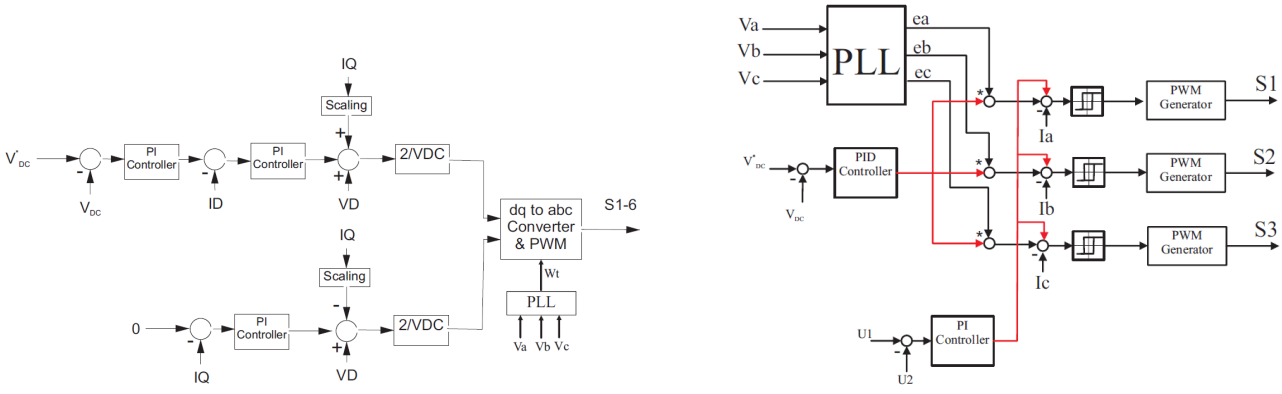

AFE Controller

Vienna rectifier controller

Figure 1.8: Controllers of AC/DC converters.

DC/DC topologies operate on much higher switching frequencies to reduce losses and increase power density. They are regulated either by controlling the phase shift be-

tween input bridge legs or by varying the switching frequency of the converter. Figure 1.9 shows the two elementary structures of these control algorithms. Phase shift algorithm can achieve a wider regulation range by changing the phase difference between (0-180) degrees, while the variable frequency method must maintain the switching frequency of the converter near the resonant to ensure soft-switching. In general, these algorithms are mergeable, and they can have exchangeable usage on the opposing topology to accomplish better performance [88].

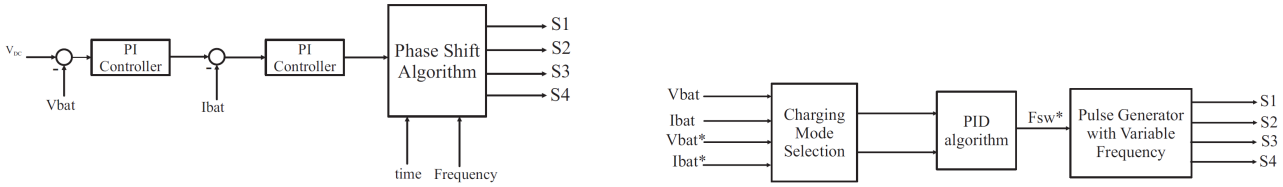

Phase shift Controller

Variable frequency controller

Figure 1.9: Controllers of DC/DC converters.

1.6 Chemical Batteries

Lead-acid batteries represent the majority of worldwide on-grid battery installations [89]. However, due to environmental concerns related to their recycling, these batteries are being phased out and replaced by lithium-ion batteries [90]. Li-ion batteries offer a satisfying energy-to-power density with fast charging capabilities. Recently, their utilization expanded over a wide range of applications including small remotely operated devices, electric vehicles, and on-grid battery farms. Therefore, it is reasonable to focus on their implementation and model development given their anticipated future. Developing accurate battery models is not only significant for test and research purposes but also for runtime parameter estimation and internal state prediction conducted by battery managers. A simplified representation of Li-ion batteries may be useful for online estimation of battery SoC and voltage-current performance [91]. These models depend on equivalent electrical circuit approximation and can produce slight runtime errors. On the other hand, the electrochemical representation of battery cells is developed mainly to address certain aspects like cell balancing, thermal stress, and aging [70; 92]. Nevertheless, these models are quite specific and not addressed in this research. A sufficient representation of the battery model incorporated the Shepherd electrochemical model and the Thevenin approximation was developed for both accuracy and runtime estimation of battery internal states [93–95]. The discharge model of Li-ion batteries is represented by:

$$E = E_0 - K\left(\frac{Q}{Q-\int i}\right) i^* - K\left(\frac{Q}{Q-\int i}\right) \int i + A * \exp\left(-B \int i\right) \tag{1.6.1}$$

while the charge model dynamics are represented by:

$$E = E_0 - K\left(\frac{Q}{\int i + 0.1Q}\right) i^* - K\left(\frac{Q}{Q - \int i}\right) \int i + A * \exp\left(-B \int i\right) \tag{1.6.2}$$

where E_0 is the constant voltage, Q is the battery maximum capacity in Ah, K is the polarization constant in V/Ah, $\int i$ is the extracted capacity in Ah, i^* is the low frequency current dynamics in A, A is the exponential voltage in V, B is the inverse exponential capacity in Ah^{-1}. Finally, the previous nonlinear equations are employed in the following electrical approximation to find the battery voltage V_{batt}:

$$V_{batt} = E - R_{int} I_{batt} \tag{1.6.3}$$

where R_{int} is the battery's internal resistance in ohm, and I_{batt} is the battery current in A. The SoC is calculated as:

$$SoC = 100\left(1 - \frac{Q}{\int i}\right) \tag{1.6.4}$$

1.7 Hardware in Loop Technology

Testing and validation of power system components and proposed controllers are a consequential task addressed by enormous international companies. A safe and realistic testing platform is required to interact with the device or controller under-test and validate its performance. This is a significant improvement from simulation-based studies where real-time properties and physical power signals were not examined. Equipment inadequacy, communication delay in controller cycles, missing modeling functionalities, model-hardware parameters mismatch, interoperability issues between different vendors, and hardware-software compatibility are some of the issues investigated by these technologies before product final deployment [96].

1.7.1 Types of in-Loop Technologies

A number of technologies employed in system validation purposes. The utilized technique depends on the inspected parameter, algorithm, or equipment. They may include:

- **Software-in-loop technique:** the power system, related parameters, and control algorithms are modeled and simulated on specialized software. This test can provide high coverage, but low test fidelity [97].
- **Hardware-in-loop technique:** the power system model is developed in a software environment and compiled on a specialized DSP processor or real-time digital simulator (RTDS). This allows functions like cycle delays, harmonics, and oscillation to be examined [98].

- **Controller-in-loop technique:** both the modeled power system and the associated developed control algorithm are deployed on different processing units. Usually, the controller is complied on an inferior computational device like a microcontroller boards to emulate the actual working environment of industrial controllers. Disturbances and perturbations can be induced and results are evaluated [99].
- **Power hardware-in-loop technique:** this is the ultimate test of a developed system or algorithm where actual physical signals are exchanged and consequences of design parameters are observed. Power converters can be controlled to emulate the behavior of the power system, while the device under test is subjected to various operational scenarios. The fulfillment of design requirements and applicability of selected parameters can be verified [100].

A detailed review of these technologies, related applications, and vendors is provided in [101]. Famous simulator platforms like OPAL-RT, virtual test beds VTB, and SpeedGoat real-time targets are some of the commercially available technologies for hardware-in-loop power system testing. Although these platforms are associated with authenticated results and marvelously perform on a larger scale, they are significantly specialized and inflexible in terms of extended equipment tests. For instance, including an energy storage device in the test cycle requires the purchase of expensive modules, which contain extensive undesired functionalities. Therefore, the customization of laboratory-based test beds is a necessity.

1.7.2 Battery Emulators

Batteries are one of the most essential components of power systems integrated into diverse low and high-power applications. However, due to their thermal and physical characteristics, it is not advised to conduct tests with real battery packs [102]. Lithium metal is a flammable material with exothermic activities that can cause thermal runaways [102; 103]. Li-ion batteries require particular attention during utilization and specialized thermal management to prevent thermal reactions and combustion. Thus, newly designed battery system technologies and algorithms need a safe and adjustable battery emulator test bench for research and design purposes. The structure of such a platform consists of a battery model developed and deployed on a specialized processor, power components for signal conditioning, and communication devices to interface the battery simulator with the test subject[104]. A HiL technology was used to test the cell-to-cell performance of battery managers using a specialized dSPACE GmbH real-time emulator[105]. Other dedicated HiL platforms utilized concepts lit XPC [106] and cell-in-loop with environmental container [107] to test specific thermal and reactive properties without exchanging real power signals. Another direction in the literature is to exploit the PHiL technology principles by employing real power converters for battery emulation. Nevertheless, the reviewed article's objectives were concentrated on

testing discharge characteristics [108], the interactions with the vehicle's drive system [109], and on-grid battery correlations and properties [110]. These research studies are essential for the conceptualization of the proposed test bench in this research but differ in application objectives and implementation.

1.8 Problem Statement and Research Tasks

Based on the previous literature analysis, it is required to develop battery system technologies for reliable power supply applications. These developed technologies need to be studied at the system utilization level and deployed component level. The subsequent reliable power supply is employed in the hoist and transport mechanism applications. The previous discussion demonstrated the significance of integrating energy storage devices in the supply systems of these mechanisms and achieved benefits. Due to the lack of research in this direction, the stacker crane system was chosen as an example of such an application. To achieve the objectives and goals of this research, the following tasks are set and addressed:

1. Development of energy management regulators for power supply systems of electrical complexes. These regulators are developed for grid-tied and isolated operation scenarios.
2. The research and development of battery charger topology and controllers that minimize switching losses and maximize voltage regulation range.
3. Development of a real-time battery emulator based on a lithium-ion battery model for testing and validation purposes of battery system components and related technologies.
4. Development of an efficient, environmentally friendly, and reliable power supply system for hoist and transport application.

Chapter 2

Microgrid Regulators

Modern electrical complexes incorporate various power generators and consumers. The utilization of distributed renewable energy sources in industrial installations is gaining increasing interest, because of the claimed peak demand reduction and electricity cost minimization [111]. However, it is important to regulate the extracted, stored, and consumed energy based on the required demand. Considering electrotechnical complexes as Microgrids allows the employment of energy management algorithms. They are synthesized to regulate active and reactive power while maintaining the voltage and frequency supplied to loads. Different algorithms are used to attain improved performance for grid-tied and islanded modes of operation. In this chapter, energy management Microgrid control methods are developed based on the operation mode. Their objectives are to regulate the power converters of distributed generators and energy storage devices while sustaining load performance. Specific concepts related to each application are also studied and evaluated. During system development, universal reactive loads are considered. The proposed method can generally be applied to diverse industrial applications, including hoist and transportation mechanisms. Recommendations on the specific implementation of these algorithms for various applications is provided.

2.1 Load Frequency Regulation

This Microgrid concept formulation suggests a holistic representation of the technologies employed in the studied electrical complex. Different components are integrated into the design structure that are jointly addressed and controlled. Each unit is expressed in a simplified transfer function that characterizes its energy contribution to the Microgrid. The load complex is depicted as a load-frequency dynamic relation that associates the energy variations in a Microgrid with the frequency deviation of the delivered power. The variable behavior of power components in a Microgrid and the existence of different generation units can lead to frequency deviations exceeding the maximum allowable limits set by the operator [112]. The control system's target is to

rapidly regulate these deviations and maintain stability. There are several problems with this approach restricting its implementation in practice. Over-simplification of system dynamics is the first issue related to its application. Power converters and distributed generators are typically modeled as nonlinear elements, while this method views them in their simplest expression. Another problem related to the separate control design of each technology. Since the power components are fused together in one block diagram as seen in figure 2.1, individual tuning of regulators is impossible. An optimization algorithm is required to locate the gain parameters of each controller that produces the best performance. Finally, load-frequency control provides an important perspective on the accumulated effects of different components on Microgrid performance. Nevertheless, subsequent energy management control algorithms in this research are developed based on more sophisticated and practical models. Thus, no extended discussion is provided on this topic.

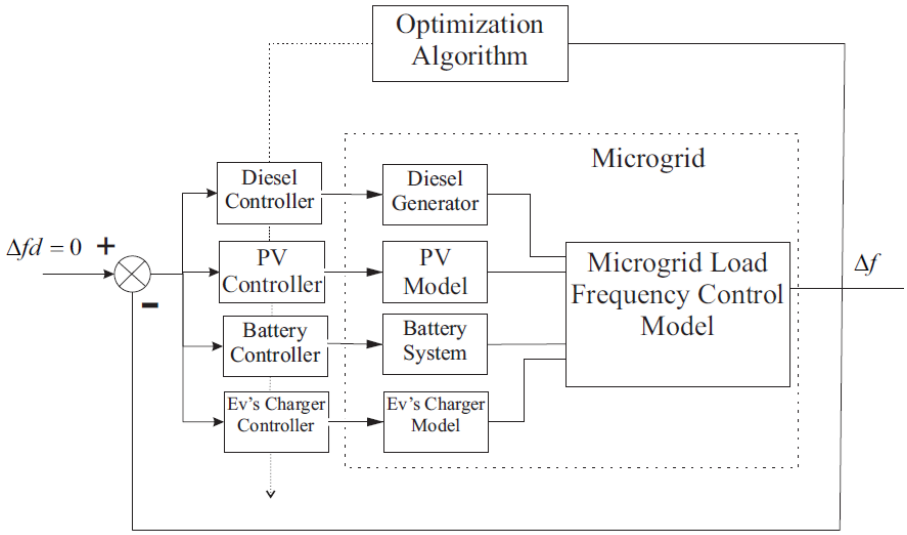

Figure 2.1: Microgrid load-frequency control system

2.2 Distributed Generator - Solar Energy

Distributed generators are increasingly integrated into the distribution network and private applications. The nature of their output power depends on their type and the employed interconnecting power converters. The majority of the integrated distributed generator capacity is photovoltaic (PV) solar panels [113]. Solar energy technology has experienced dramatic development in recent years, which encouraged a market growth of 34% in installed capacity [114]. In this section, the principles of solar energy modules utilized throughout this research are described. The output power rating of solar panels depends on the parallel and serial-connected cells. Although solar energy generation suffers from extreme fluctuation, power electronic devices and special control algorithms are used to ensure the extraction of maximum available power. A DC boost

converter is controlled by a maximum power-point tracking (MPPT) algorithm, which changes the operating point of the converter based on irradiation changes. The configuration of this system is exhibited in figure 2.2. The capacitor C_2 is chosen large enough to filter any output voltage ripple, while the pre-filter parameters C_1 and L_1 are calculated as follows:

$$C_1 = \frac{I_{out}\,(V_{out} - V_{in})}{f_{sw} * \Delta V * V_{out}} \tag{2.2.1}$$

$$L_1 = \frac{V_{in}\,(V_{out} - V_{in})}{f_{sw} * \Delta I * V_{out}} \tag{2.2.2}$$

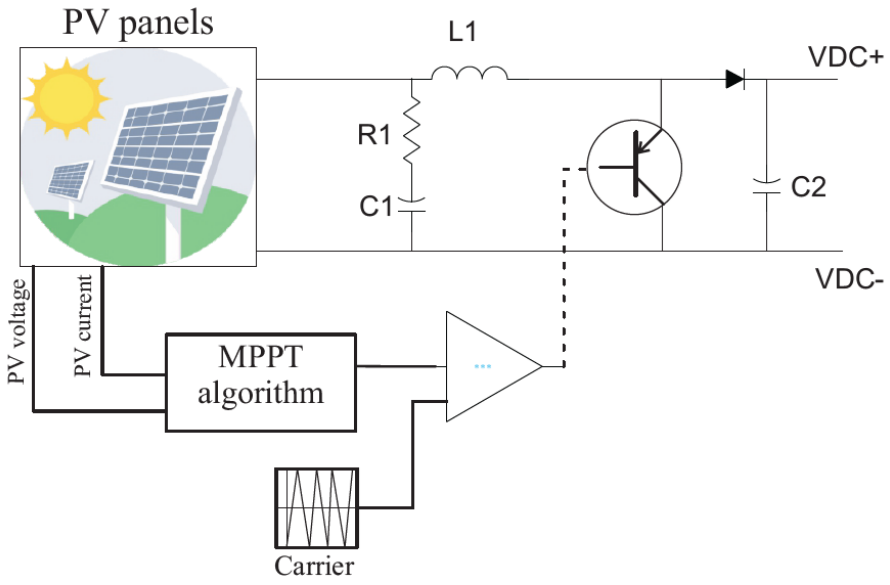

Figure 2.2: PV solar panel with the boost converter.

f_{sw} represents the switching frequency. Based on the voltage and current measurements of the PV solar panels, MPPT algorithm reacts either by slightly increasing or decreasing the reference voltage of the converter to preserve maximum output power. This algorithm is illustrated in figure 2.3, which represents one of the most common possible configuration of this method [115].

2.3 Grid-tied Microgrid

As the name indicates, these Microgrids operate in cooperation with the electricity grid. Usually, grid-tied Microgrids are hybrid in nature, which means they encapsulate AC and DC resources and loads. The energy sharing between different local generators and the grid is managed, while the performance of connected loads is maintained [25]. The energy-sharing process is administrated by regulating the interlinking AC/DC bidirectional converter [26]. The implemented control strategy computes the necessary active and reactive power and performs the required compensations. The

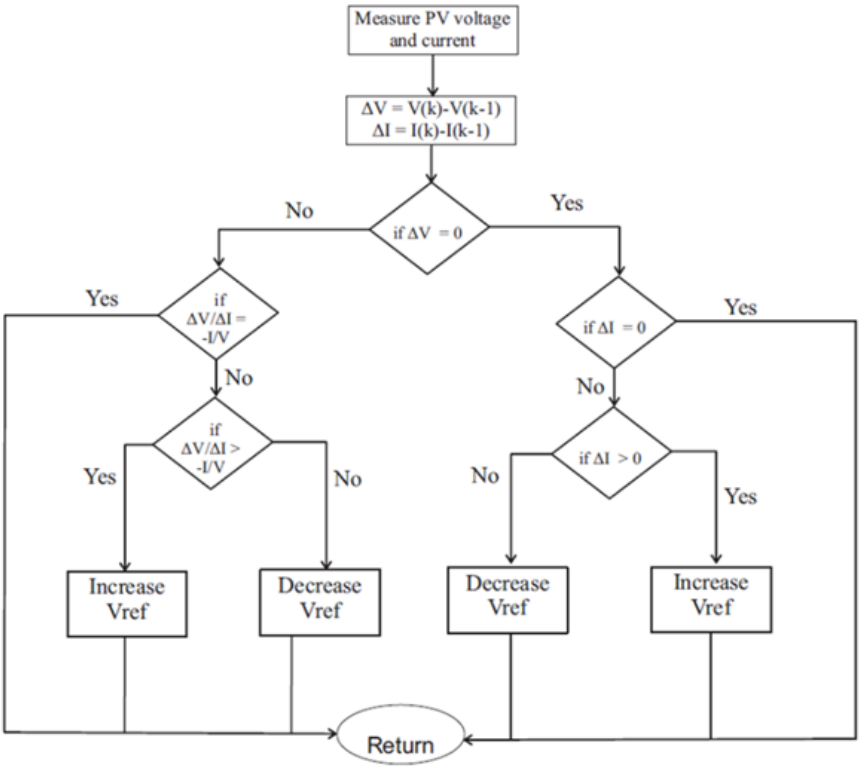

Figure 2.3: MPPT algorithm.

general configuration of a grid-tied hybrid Microgrid is shown in figure 2.4. The three-phase dynamic load represents any industrial or residential load connected to the AC side of the Microgrid. On the other hand, the DC side of the grid can be disconnected at any instant and operated as an islanded sub-grid, when DC resources are depleted or the quality of DC power is in jeopardy.

2.3.1 Grid Supporting Droop Controllers

These controllers regulate the voltage and frequency levels on the AC side by injecting active power from the DC side of the grid. As previously stated, the droop control mechanism is hierarchically structured to allow a multi-level response that attenuates disturbances and load change influences. Figure 2.5 demonstrates the block diagram of a grid-supporting controller with dual droop actions. The E_m and F_m parameters depict the measured voltage and frequency levels on the AC side, which are compared with the required set points to produce a regulation error. The two PID controllers in parallel represent the primary and secondary droop regulators, while P^* and Q^* are the active and reactive power references. The current regulator functions as a low-level control mechanism regulating the interlinking bidirectional converter currents based on the previous droop resolutions. These regulator command signals are calculated according to the following equations (2.3.1-2.3.2):

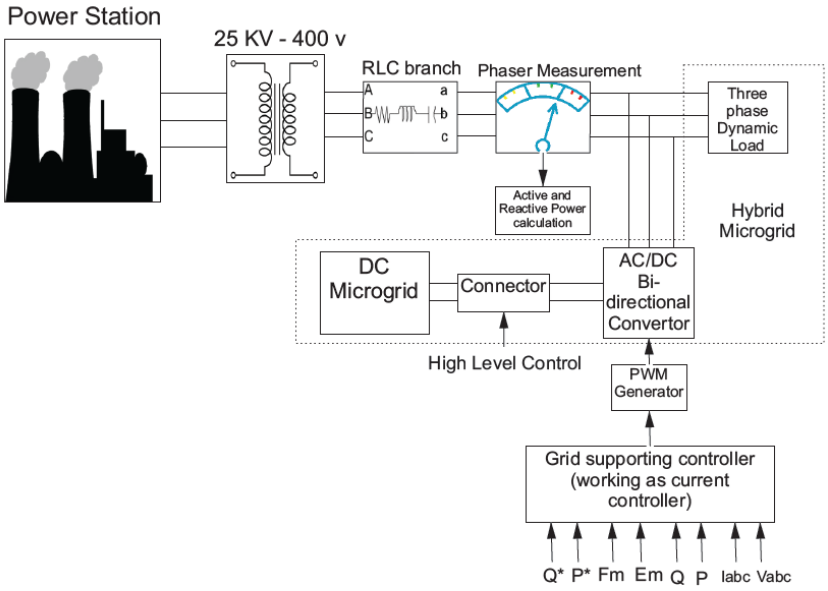

Figure 2.4: Grid-tied hybrid Microgrid.

$$U_d = V_d + \left(I_{dref} - I_d\right) * R - \left(I_{qref} - I_q\right) * L + \left(\dot{I_{dref}} - \dot{I_d}\right) * L \tag{2.3.1}$$

$$U_q = V_q + \left(I_{dref} - I_d\right) * R + \left(I_{qref} - I_q\right) * L + \left(\dot{I_{qref}} - \dot{I_q}\right) * L \tag{2.3.2}$$

where L and R parameters represents the utilized filter of the bidirectional converter.

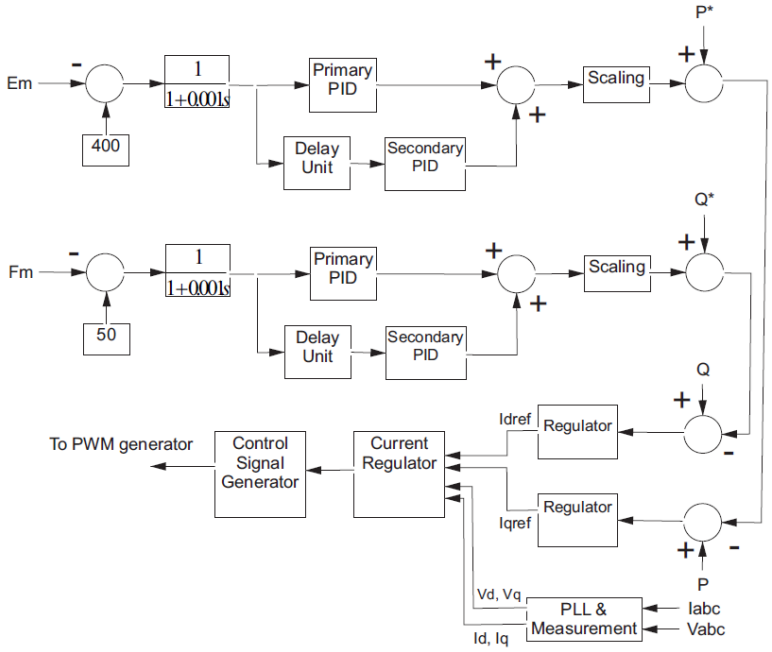

Figure 2.5: Grid supporting droop control scheme.

Although this type of control structure is common and can perfectly regulate the power-sharing process between two sides of the Microgrid, tuning the dual droop controllers for voltage and frequency is quite a challenging assignment. One solution is

to employ an optimization algorithm that iterates and finds the best controller parameters according to the provided performance index. The particle swarm optimizations (PSO) algorithm, which is roughly explained in Appendix A, is utilized in this research to conduct such a task. The performance index is user-formulated, which means different indexes can produce different results. The following index is formulated to penalize the voltage and frequency deviations from reference levels and the over-extraction of energy from the DC side of the grid.

$$Per_{index} = \left(E_{ref} - E\right) + \left(F_{ref} - F\right) + \sum \forall P_{DC} \leq 15kW \tag{2.3.3}$$

Traditionally, the DC sub-grid consists of the battery system, DC generators like PV panels, and Critical Loads. In case of accidents or grid faults, the DC sub-grid is sustained by the local generator and storage devices. Figure 2.6 presents an example of such a composition. The power converter of the solar energy system is controlled by the MPPT algorithm, accomplishing maximum performance. For evaluating the designed control scheme quality, the power system parameters in table 2.1 are simulated in MATLAB/Simulink environment.

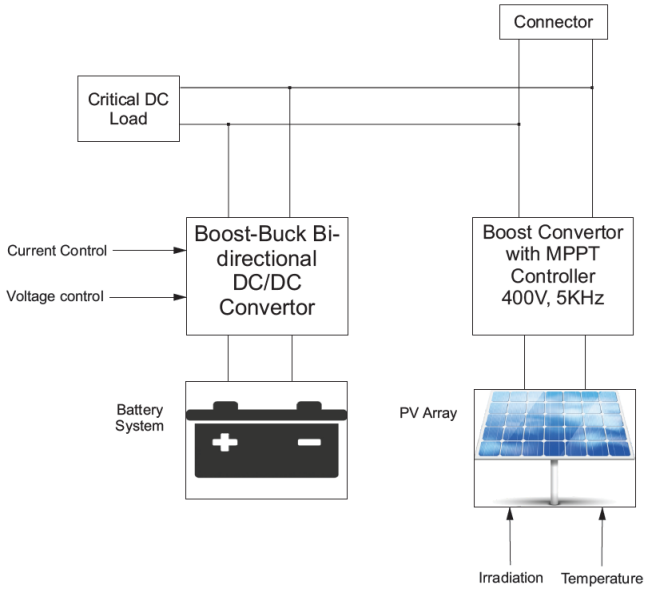

Figure 2.6: The DC sub-grid.

Table 2.1 — Droop control based System parameters

Parameter name	Value	Units
3-ph load active and reactive power	$10^3, 10^3$	W, Var
PV solar panels	10^3	Kw
E_{ref}	400	V
F_{ref}	50	Hz
Battery Capacity	200	Ah
Battery SoC	60	%
DC load	15	Kw

Figure 2.7 exhibited the AC side response of the grid. Regardless of variations in the active and reactive power caused by the dynamic load, voltage, and frequency were regulated and maintained at desired levels. This is due to the extracted power by the droop action from the DC side resources. The effect of increased power extraction can be observed in figure 2.8. The PV solar panels and the battery system injected more power than required to operate the DC critical load. This power is transferred to the AC side for regulation using the interlinking converter.

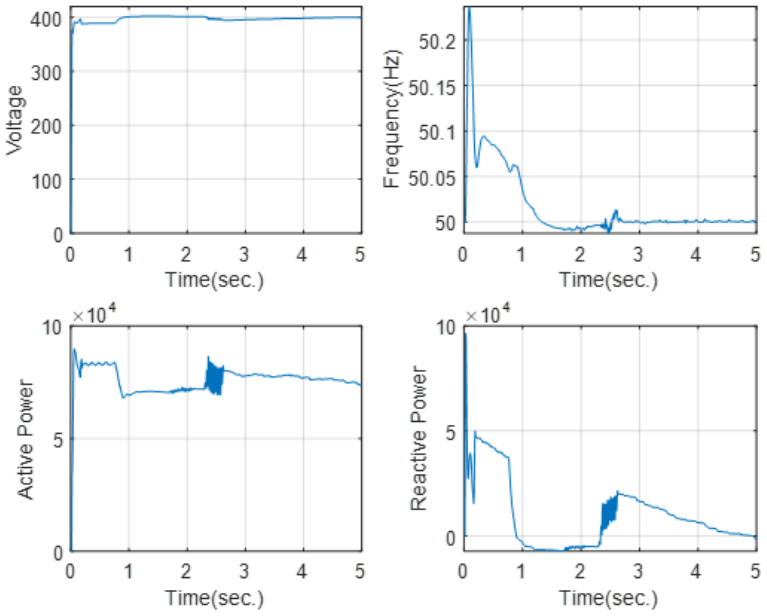

Figure 2.7: The Microgrid AC side response.

In some scenarios, the grid-supporting controller exhausts more power from the DC resources than is demanded for normal operation. In this case, the DC side must be detached and managed as an islanded sub-grid. This is to conserve the critical load functionality and to prevent the deterioration of battery systems SoC and SoH. The optimization algorithm performance is illustrated in figure 2.9. As seen in the figure, the index declined by (5.2%) in just under 20 iterations. This index reduction corresponds to performance enhancement.

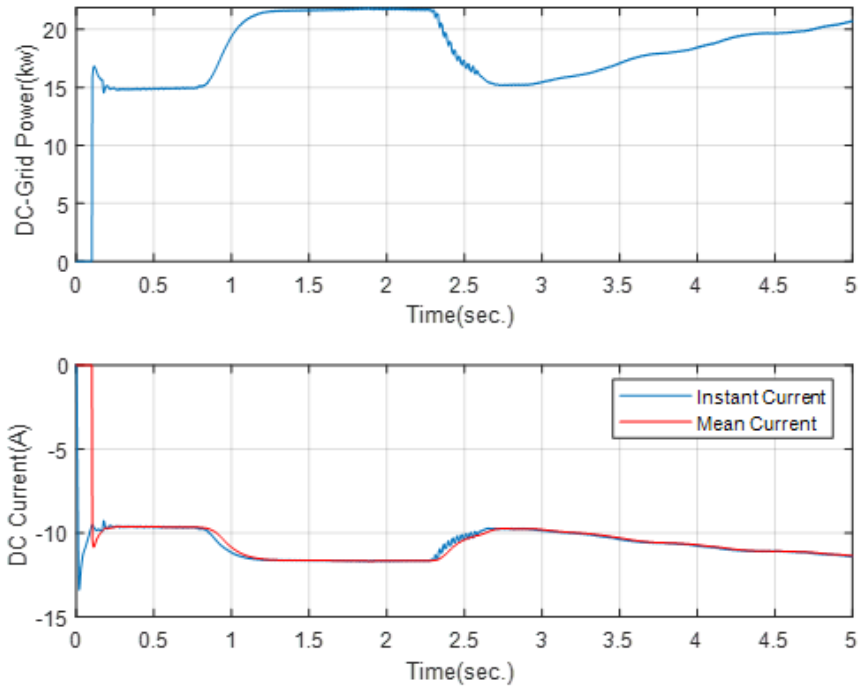

Figure 2.8: The Microgrid DC side response.

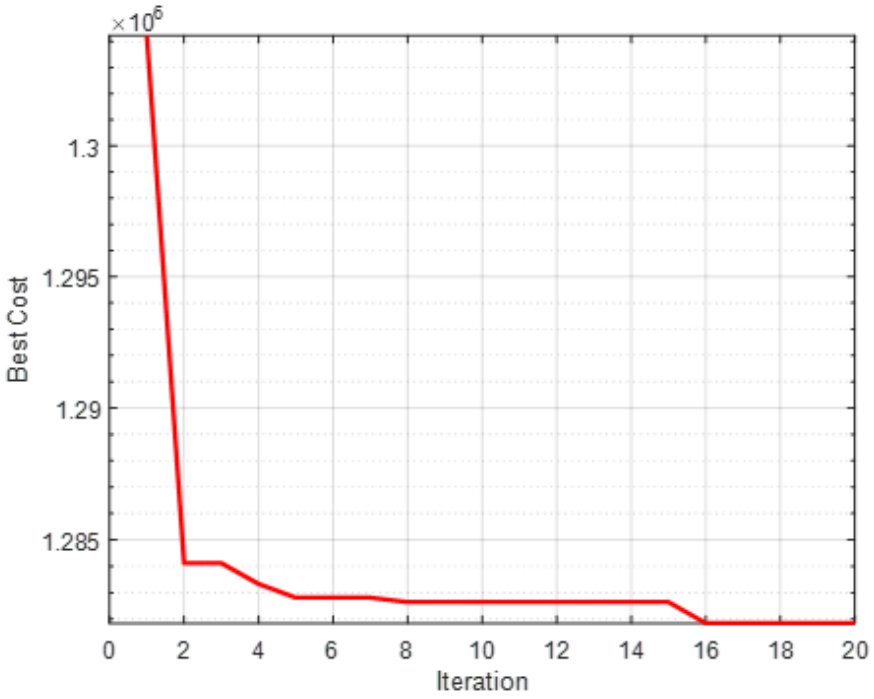

Figure 2.9: PSO optimization performance.

2.3.2 Sliding Mode Current Controller

The previously presented current regulation method in equations (2.3.1-2.3.2) has acceptable performance and simple implementation. However, no methodical verification for stability is provided. The sliding mode control strategy is developed based

on the converter dynamic equations. It is a well-established method in the literature that ensures the stability of the synthesized system using the Lyapunov principles. The three-phase inverter converter is modeled in the (abc) frame as [116]:

$$L\frac{dI_{abc}}{dt} = -RI_{abc} + V_{abc} - Vg_{abc} \tag{2.3.4}$$

where V_{abc} and I_{abc} are the three-phase voltages and currents respectively, while Vg_{abc} represent three-phase voltages of the grid. Then by Denoting that:

$$V_{abc} = \frac{V_{DC}}{2}\begin{bmatrix} 2 & -1 & -1 \\ -1 & 2 & -1 \\ -1 & -1 & -1 \end{bmatrix} U_{abc} \tag{2.3.5}$$

and using the following transition matrix to transfer the system from the (abc) coordinates to the (dq) frame:

$$T = \frac{\sqrt{3}}{2}\begin{bmatrix} \cos\theta & \cos\theta - \frac{2\pi}{3} & \cos\theta + \frac{2\pi}{3} \\ -\sin\theta & \sin\theta - \frac{2\pi}{3} & \sin\theta + \frac{2\pi}{3} \end{bmatrix} \tag{2.3.6}$$

we get,

$$L\frac{dI_{dq}}{dt} = -AI_{dq} + V_{DC}U_{dq} - Vg_{dq} \tag{2.3.7}$$

where

$$A = \begin{bmatrix} R & -LW \\ LW & R \end{bmatrix} \tag{2.3.8}$$

The W parameter refers to the angular frequency, which is calculated by the phase-locked-loop (PLL) method to synchronize the operation of the inverter/converter with the power grid.

The sliding mode procedure starts by defining the sliding surfaces as the difference between reference and actual current of the converter:

$$S_d = I_d - I_d^{ref} \tag{2.3.9}$$

$$S_q = I_q - I_q^{ref} \tag{2.3.10}$$

A sliding vector is formed by combining the two sliding surfaces:

$$\rho = \begin{bmatrix} S_d \\ S_q \end{bmatrix} \tag{2.3.11}$$

The derivative of this vector is minimized to zero which indicate the elimination of current error.

$$\dot{\rho} = \begin{bmatrix} \dot{S_d} \\ \dot{S_q} \end{bmatrix} = 0 \tag{2.3.12}$$

For constructing the variable structure sliding mode controller, the sliding vector derivative is assumed as:

$$\dot{\rho} = \begin{bmatrix} -\delta_d Sgn(S_d) - K_d S_d \\ -\delta_q Sgn(S_q) - K_q S_q \end{bmatrix} \tag{2.3.13}$$

where δ_d and δ_q represents the magnitude of the switching functions, while the K_d and K_q are the sliding surface gain parameters. By substituting these expressions in the converter system dynamics in equations 2.3.7 and 2.3.8, the following equations are obtained:

$$V_{DC}U_d - Vg_d = -\delta_d Sgn(S_d) - K_d S_d - LWI_q \tag{2.3.14}$$

$$V_{DC}U_q - Vg_q = -\delta_q Sgn(S_q) - K_q S_q + LWI_d \tag{2.3.15}$$

The control signals U_d and U_q are developed as:

$$U_d = \frac{1}{V_{DC}}\left(-\delta_d Sgn(S_d) - K_d S_d - LWI_q + Vg_d\right) \tag{2.3.16}$$

$$U_q = \frac{1}{V_{DC}}\left(-\delta_q Sgn(S_q) - K_q S_q + LWI_d + Vg_q\right) \tag{2.3.17}$$

Substituting equations 2.3.16 and 2.3.17 in the sliding vector derivative equation, detailed descriptions of the sliding surfaces are obtained.

$$\dot{S_d} = \frac{-1}{L}\left(RS_d + \delta_d Sgn(S_d) + K_d S_d + RI_d^{ref} + L\dot{I}_d^{ref}\right) \tag{2.3.18}$$

$$\dot{S_q} = \frac{-1}{L}\left(RS_q + \delta_q Sgn(S_q) + K_q S_q + RI_q^{ref} + L\dot{I}_q^{ref}\right) \tag{2.3.19}$$

the necessary conditions for stability take the multiplication of sliding surfaces and their derivatives and ensures that they are negative in value. These conditions are expressed as:

$$S_d\dot{S_d} < 0 \tag{2.3.20}$$

$$S_q\dot{S_q} < 0 \tag{2.3.21}$$

The stability conditions for δ_d and δ_q magnitudes that ensures error minimization are:

$$\delta_d > |RI_d^{ref} + L\dot{I}_d^{ref}| \tag{2.3.22}$$

$$\delta_q > |RI_q^{ref} + L\dot{I}_q^{ref}| \tag{2.3.23}$$

Whereas for the K_d and K_q gain parameters, it is enough to choose any positive value to guarantee the stability of the overall dynamics.

2.3.3 Grid Current Injection

Another method of managing injected power from a distributed generator into the Microgrid complex is the Fryze current minimization technique. This method computes the required current to be injected or absorbed by the converter depending on load demand and grid contribution. This method establishes a simple power-sharing process based on local measurements to regulate the energy exchange. In general, this method is deployed with any type of distributed generator. However, due to the enabled

bidirectional power exchange capability, it is mostly applied on energy storage devices operating with power inverters in a Microgrid. The minimization function is calculated as:

$$G = \frac{P_g}{V_a^2 + V_b^2 + V_c^2} \tag{2.3.24}$$

where P_g is the power contribution of the grid, having a positive value in grid-supporting mode and a negative value in grid-supplying mode. Then, a butter filter is implemented on the G function output with a cut-off frequency of (60 Hz).

$$\bar{G} = Butter_{filter}(G) \tag{2.3.25}$$

The reference currents in the (abc) frame are determined as follows:

$$I_{abc}^{ref} = V_{abc}\bar{G} - IL_{abc} \tag{2.3.26}$$

Equation 2.3.26 generates the three-phase currents, but these signals are usually transferred to the (dq) frame to be utilizable in later controller development stages.

$$I_{dq}^{ref} = dq(I_{abc}^{ref}) \tag{2.3.27}$$

To investigate the performance of the Fryze current minimization technique in energy extraction of a distributed generator unit, the power system in figure 2.10 was studied and simulated. A three-level four-leg inverter was utilized to deliver the energy from the distributed generator, expressed as a DC source, to the load-grid complex. The configuration and operational advantages of this converter are exhibited in Appendix (B). A neutral point compensation is assumed and the sliding mode technique is exploited for current control. The Fryze method provides the reference currents to the sliding mode controller where current regulation is performed. Since the sliding mode method was developed based on a three-leg power converter, it is required to generate the fourth control channel, which controls the extra converter's leg. The following equations are employed for determining the control signal of the neutral point leg:

$$U_n = -0.5 \min U_{abc} - 0.5 \max U_{abc} \tag{2.3.28}$$

Next, the control vector containing the four control signals is re-calculated as:

$$U_{abcn} = [U_{abc} - U_n, U_n] \tag{2.3.29}$$

It should also be mentioned that the employed three-level topology requires a capacitor balancing regulator, which is combined with the control action on the d-channel of the current controller.

The tested power system parameters are shown in table 2.2. The values of the switching magnitudes $delta_d$ and $delta_q$ in equations 2.3.22 and 2.3.23 are calculated as infinite norms, cautiously considering the maximum possible value. The grid contribution factor P_g is initially assumed as (-5kW), which indicates that the inverter is supplying a grid-load combination. After two seconds, the P_g factor is changed to (2kW),

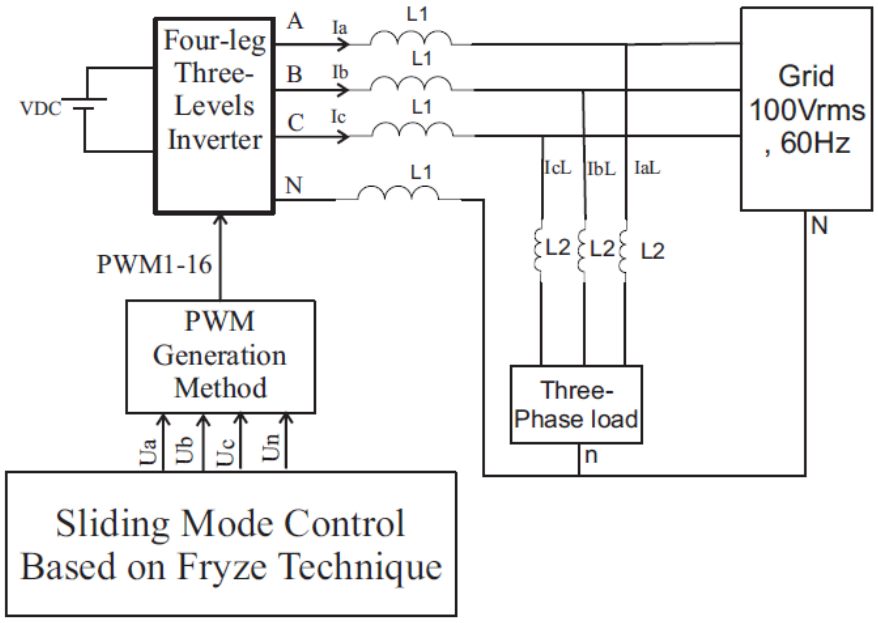

Figure 2.10: Distributed generator energy management based on Fryze technique.

which means that the grid is to contribute that power to supply the load. Finally, one second after the change, the factor value was dropped to (-3kW), enabling the injection of energy into the grid again.

Table 2.2 — Fryze technique based system parameters

Parameter name	**Value**	**Units**
L_1r	7	mH
L_2	1	mH
V_{DC}	300	V
C_1 and C_2	650	μF
R_1 and R_2	0.001	ohm
$\|\|\delta_d\|\|$ and $\|\|\delta_q\|\|$	250	–
K_d and K_q	100	–

Figure 2.11 exhibits the active and reactive power responses of the inverter and load complex. The sub-figures (a&b) represent the extracted power from the distributed generator, while sub-figures (c&d) show the delivered power to the load demand.

The sliding mode controller performance is demonstrated in figure 2.12. As seen in the figure, the actual and reference currents are identical, which indicates an extraordinary tracking performance of the employed method. The inverter phase-to-phase three-level voltage is shown in figure 2.13. These levels imply better dynamic performance of the system and smoother supplied voltage. The figure also illustrates the

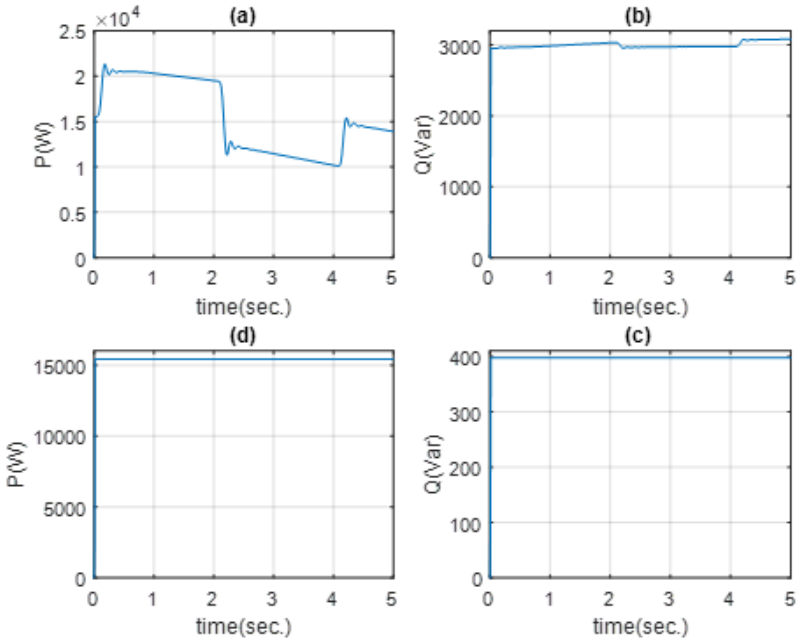

Figure 2.11: Active and reactive power simulation of the inverter and load.

neutral line current used to compensate for imperfectness and fluctuations in the grid-load demand side.

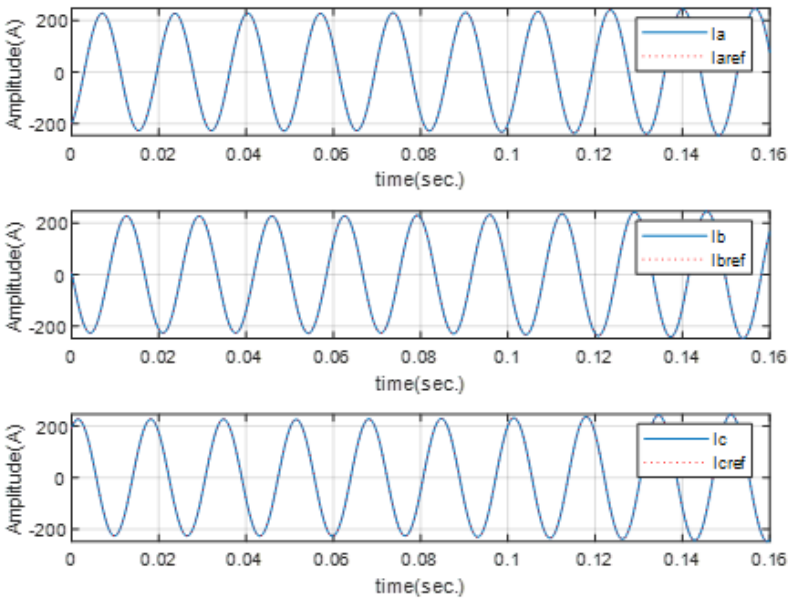

Figure 2.12: Performance of the sliding mode current controller.

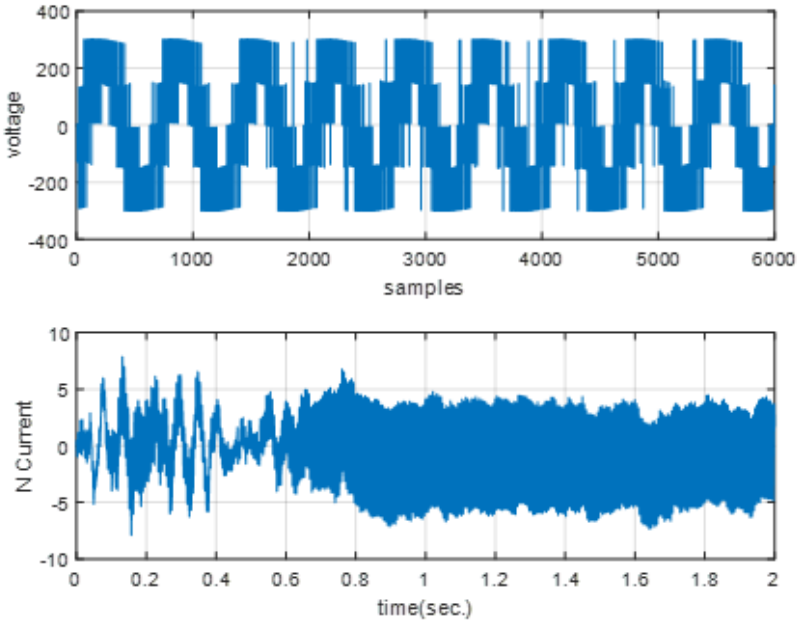

Figure 2.13: Unique response of the three-level four-legs inverter.

2.4 Islanded Microgrid

The integration of locally distributed generators, especially renewable-type generators, has unwrapped the possibility of autonomously operating certain parts of the electricity grid as islanded Microgrids. The local standalone power supply system can incorporate different generator units and storage devices to satisfy local demand. These Microgrid configurations are usually employed in critical infrastructure and commercial sectors, where the supplied energy quality depends on the utilized control scheme [117]. Although integrating adequate local generator capacity ensures the fulfillment of load demand, these generators suffer from low controllability and the islanded Microgrid usually experiences inertial response deprivation [118]. To rectify these issues, a proper control mechanism must be utilized to regulate the generator converter, battery storage devices, and load complex. In this section, the synthesis of energy management mechanisms is addressed and evaluated based on several examples inspired by practice.

2.4.1 Proportional Resonant (PR) controller

Instead of using the traditional PI controller, a new control tool was adopted to enhance tracking performance, reduce steady-state error, and eliminate harmonics [119]. Although this type of controller can be applied to various power systems, it is more preferably implemented in the inverter of a standalone power supply system. This is due to the controller's offered advantages which enable fast reaction and compensation of the regulated converter during inertial response situations. The PR controller is de-

veloped based on the dynamic equations of the three-phase inverter in the (abc) frame [120]:

$$\begin{bmatrix} V_a \\ V_b \\ V_c \end{bmatrix} = \begin{bmatrix} C_{an} \\ C_{bn} \\ C_{cn} \end{bmatrix} - L\frac{d}{dt}\begin{bmatrix} I_a \\ I_b \\ I_c \end{bmatrix} \tag{2.4.1}$$

$$\begin{bmatrix} I_a \\ I_b \\ I_c \end{bmatrix} = \begin{bmatrix} I_{aL} \\ I_{bL} \\ I_{cL} \end{bmatrix} - C\frac{d}{dt}\begin{bmatrix} V_a \\ V_b \\ V_c \end{bmatrix} \tag{2.4.2}$$

where C and L are the filter parameters, the C_{an} represent the control signal on phase (a), I_L is the load current on each phase. The PR controller is assigned to regulate the voltages and generate the reference current as follows:

$$\begin{bmatrix} I_a^* \\ I_b^* \\ I_c^* \end{bmatrix} = G_{PR}\begin{bmatrix} V_a^* - V_a \\ V_b^* - V_b \\ V_c^* - V_c \end{bmatrix} \tag{2.4.3}$$

the G_{PR} symbolizes the transfer function of the resonant converter which has the following form:

$$G_{PR} = K_P + \frac{K_i s}{s^2 + K_i K_f} \tag{2.4.4}$$

Considering that the controller has embedded filter capability characterized by the extra zero-pole in the second term, and the controller adjustable parameters are K_P, K_i, and K_f. Then, the control vector can be expressed as:

$$\begin{bmatrix} C_{an} \\ C_{bn} \\ C_{cn} \end{bmatrix} = \begin{bmatrix} I_a^* - I_a + I_{aL} \\ I_b^* - I_b + I_{bL} \\ I_c^* - I_c + I_{cL} \end{bmatrix} K(s) + \begin{bmatrix} V_a \\ V_b \\ V_c \end{bmatrix} \tag{2.4.5}$$

$K(s)$ is a vector transfer function with each element is the PR transfer function exhibited in 2.4.4.

2.4.2 Fuzzy Logic Energy Management

Fuzzy logic is a type of intelligent decision-making algorithm based on system-user experience. It can handle noise-polluted and rapidly varying signals to produce decisions formerly built within its internal inference mechanism. The algorithm consists of a fuzzification process involving projecting measured signals on nonlinear membership functions to obtain transformed values. Based on the acquired results, the inference mechanism fires a proper rule, which is then re-projected into the real world by the de-fuzzification process. This research uses the Sugeno-type fuzzy logic, which means that the inference mechanism produces crisp output values that do not require a de-fuzzifier like in Mamdani-type [121].

This management algorithm is more particularly utilized in generating reference current signals for battery systems operating in an islanded Microgrid situation. Since the design of such an algorithm completely relies on the configuration of the addressed power system, a study-case-based design is introduced. The studied islanded Microgrid structure is demonstrated in figure 2.14. Once again, the three-level four-leg topology is considered for connecting the DC side resources to the AC side nonlinear demand. A PR controller was utilized to regulate the converter operation, while an MPPT algorithm was employed to control the solar panels-connected boost converter. The fuzzy logic energy management system is used as a reference current generator for the buck-boost converter integrated into the battery system. It receives the power demand predictions and the solar power generation signals that are usually vague and fluctuating values.

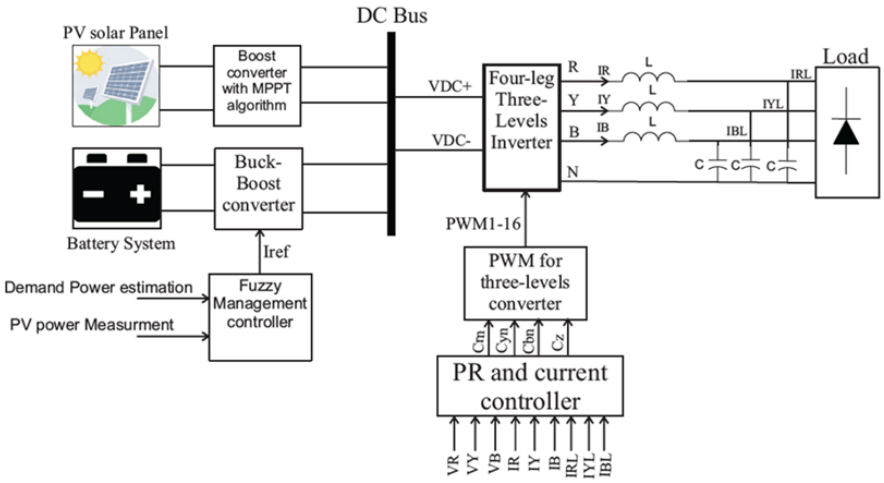

Figure 2.14: Islanded Microgrid with an automated power supply.

The load configuration considered in this particular example was inspired by [122], where an asymmetrical nonlinear load structure was utilized. This configuration imposes a challenge for the developed control algorithm, which is required to maintain balanced operation regardless of the difficult operational conditions. The load configuration is shown in figure 2.15, where the the inverter is connected to various load arrangements through diode rectifiers. This load does not necessarily reflect a realistic operational electrical complex, but rather used in literature as test subject for newly synthesized energy management algorithms. The hoist and transport mechanism addressed in the fifth chapter of this dissertation is well-balanced and does not include nonlinear diode rectifier effects. Thus, the controller is expected to behave much better in terms of response quality. Further information about the load rating can be found in [35].

The fuzzy system membership functions and the obtained fuzzy surface are exhibited in figure 2.16. The output reference current spans from (-30A) to(30A), and the system parameters have been designed accordingly. During the solar energy decline period, the fuzzy manager ensures a power discharge proportional to the required current demand. The management system administrates the proper charging power when

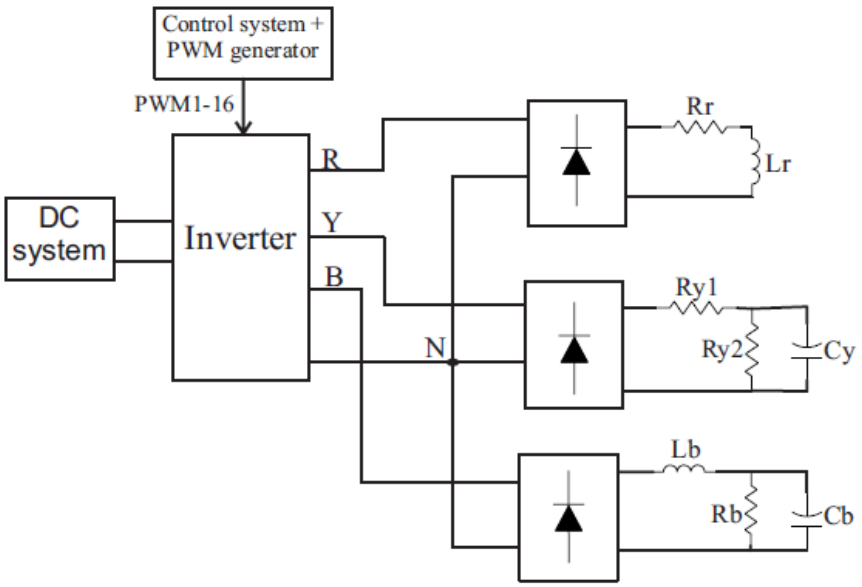

Figure 2.15: Topology of the asymmetrical nonlinear load.

demand is low or solar generation is high. The fuzzy rules are listed in table 2.3.

Table 2.3 — Fuzzy rules for energy management

Inputs		*Generation*			
Demand	**Levels**	**Zero**	**Low**	**Medium**	**High**
	Zero	Z	LC	MC	HC
	Low	LD	Z	LC	MC
	Medium	MD	LD	Z	LC
	High	HD	MD	LD5	Z

The demand and solar generation are demonstrated in figure 2.17. The fuzzy-generated battery reference current corresponded to the solar energy drop and gradually changed the battery system from charge to discharge mode. The load demand is an asymmetrical nonlinear load, which is attained by the three-phase four-leg converter. The full power rating and system parameters design with load configuration are provided in [35]. The battery current fluctuations are considered significant for practical realization. These fluctuations correspond to the utilized load nature. They are also correlated to the demand variations represented in the figure. This effect was not observed in later application of this controller configuration in Chapter(5).
The response later demonstrated in figure 5.27 represents the implementation of the fuzzy management algorithm with actual industrial load with normal operation.

The battery system response is exhibited in figure 2.18 with the SoC of the battery changing gradually to accommodate power system changes. The actual battery current tracked the nominal value of the fuzzy generated reference current shown in figure 2.17.

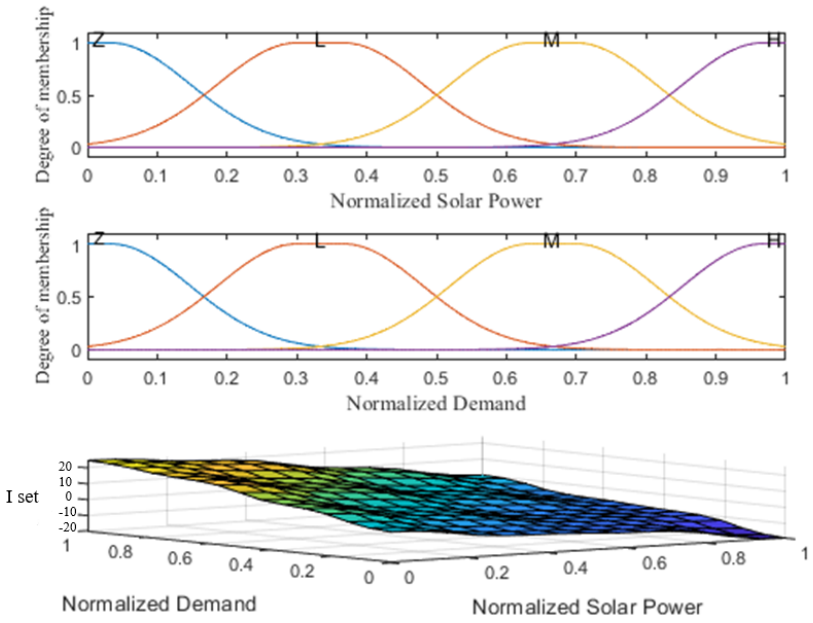

Figure 2.16: Fuzzy logic energy management system.

The responses exhibited in the two figures can be improved by introducing capacities power filters into the individual power lines. Serially adding these filters into each phase acts as current sources, which assist in minimizing line fluctuation. Furthermore, strict filtering and averaging of the fuzzy system input signals reduced variations in the fuzzy controller output. Figure 2.19 demonstrates the Microgrid and fuzzy system responses after the previously mentioned changes. The filtering effect is quite clear on the input PV and demand signals of the fuzzy management systems which induced a smooth output reference current. The battery system response corresponded to these improvements with much smoother and more realistic current response.

Finally, figure 2.20 displays the unique behavior of the employed converter with three-level phase-to-phase output and neutral line compensations. By comparison, it can be observed that the neutral current in this example is higher in magnitude than the one seen in figure 2.13. This corresponds to the regulated load nature, which requires more neutral line compensation.

The fuzzy management system was successfully designed and applied to the islanded Microgrid example for battery system regulation. It proved effective in managing distributed resources in such a standalone power supply system.

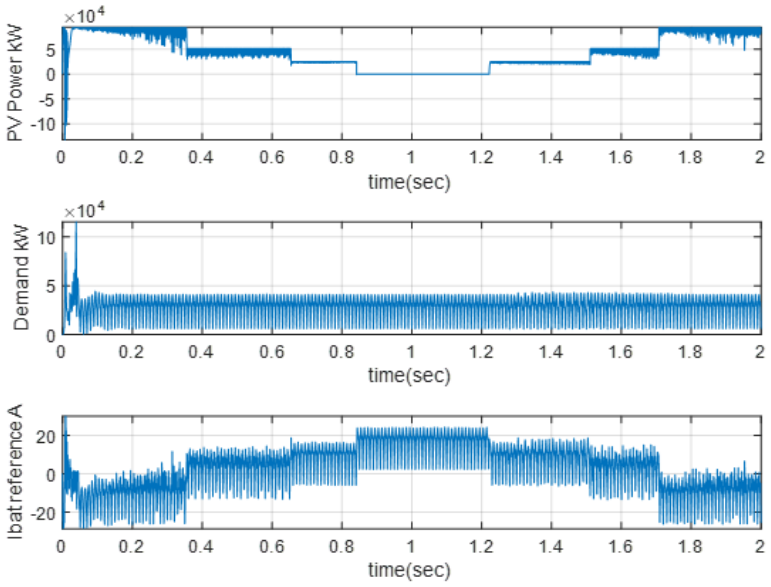

Figure 2.17: Islanded Microgrid response.

2.4.3 Power-Sharing of Scattered Inverters

Industrial applications comprise several electrical complexes performing different duties. Power-sharing of multiple parallel-connected inverters is an important aspect of the complex performance [123]. In an islanded operation, the energy management system is required to synchronize the operation of connected inverters to maintain voltage and frequency while sharing the demand. In such applications, distances and line parameters play an important role in the quality of the power-sharing process by restricting the instantaneous response of distant inverters. A large warehouse with various hoist applications like crane systems is a perfect example of this issue.

A supervisory energy management system is required to regulate the quality of the delivered demand power. The previously explained droop control principles are employed to regulate the inverter dynamics. Figure 2.21 demonstrates the configuration of parallel inverters operating in an islanded Microgrid situation. Droop controllers react locally based on the line measurements, while the supervisory controller oversees the delivered power quality over the entire complex.

The supervisory controller structure is quite simple, composed of two PID controllers for voltage and frequency regulation. It supplies the distributed droop controllers with voltage and frequency deviations substituted in the general droop characteristic equations presented in (1.3.1-1.3.2). The inner voltage and current control loops architecture is shown in figure 2.22 where the outputs are the modulation signals of the inverter switches.

Figure 2.23 exhibits the distributed source of each inverter, which is represented as a battery system with (350V, 200Ah) rating. These systems supply the entire op-

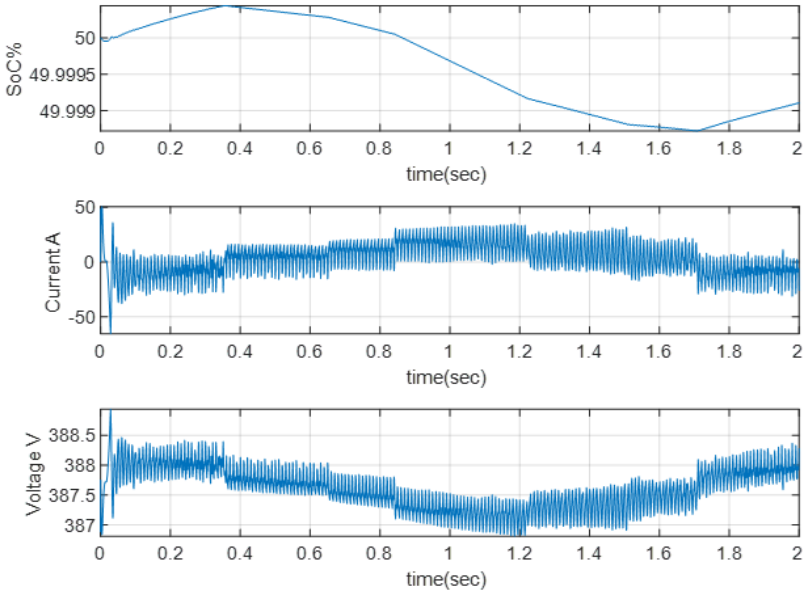

Figure 2.18: Battery system response with fuzzy management system.

eration of the load complex in figure 2.21, each having a (5.3kW, 200Var) of active and reactive power. Power-line parameters were modeled as RL branches with a resistance of (0.15mω) and inductance of (0.35mH). These branches are placed between each load, which makes the first inverter reaction to changes in the last load very slow.

The voltage and frequency response of the studied system is shown in figure 2.24. The disturbance load seen in figure 2.21 activates at (5 sec.) and disconnects after one second. Miner deviations are observed in the voltage and frequency responses of the three inverters, which implies that the local droop controllers sustained their regulation accurately. The active and reactive power responses are demonstrated in figure 2.25.

A faster reaction of the third inverter can be witnessed, with more active power being injected for compensation. However, when other inverters picked up their contribution, the steady-state active power injection of the first inverter dropped accordingly. Although some expected delays are encountered, the active power-sharing process is maintained. Nevertheless, the reactive power responses of the three inverters are different. This suggests that the reactive power depends not only on the demanded load but also on the strategic location of each inverter in the electrical complex.

2.4.4 Virtual Synchronous Generator

As previously explained in Chapter One, the lack of inertial response in islanded Microgrids can limit the frequency regulation capability of local controllers. This is due to the absence of mechanical turbines responsible for maintaining grid stability during disturbances and variations. Therefore, a virtual synchronous generator concept is in-

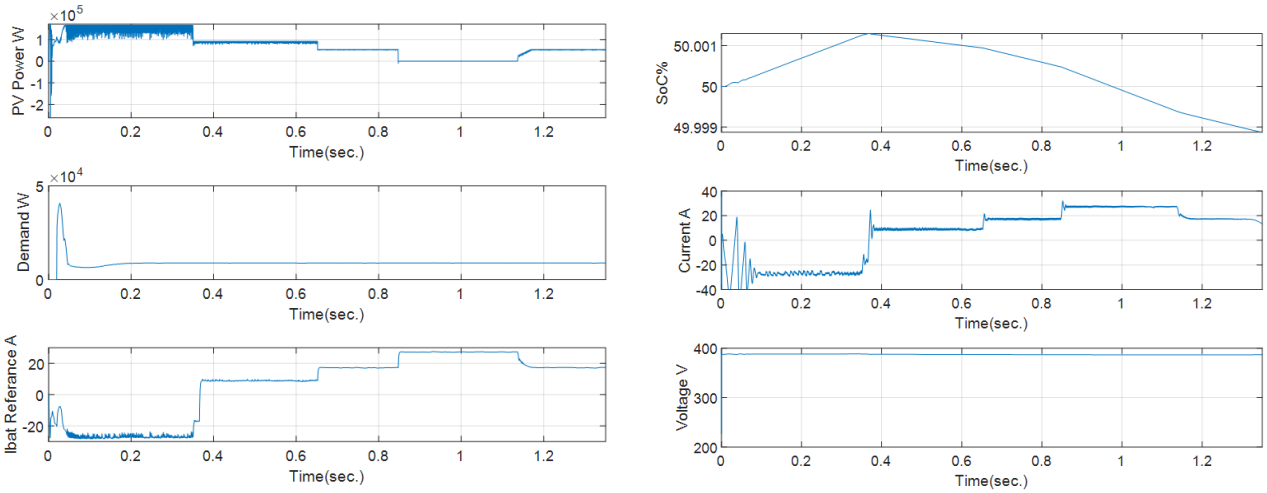

Fuzzy system response

Battery system response

Figure 2.19: Islanded Microgrid response after improvements.

troduced in equations (1.3.3-1.3.4) to induce inertia. The virtual machine emulates the behavior of mechanical machines by manipulating the power converters. This subsection investigates the configuration and effectiveness of this method on the quality of the delivered power and the energy-sharing process.

The same previous configuration in figure 2.21 was modified to include the VSG model. However, for simplicity, only two inverters are considered. Figure 2.26 demonstrates the modified structure with the added control blocks. The supervisory and local droop controllers maintained the same design, while additional P/f, Q/V controllers, and VSG models were inserted between the droop and the double loop control blocks. The P/w, Q/V characteristics accept the reference active power P_*, reactive power Q_*, voltage V^*, and frequency W^* to develop the synchronous generator modeled voltage and mechanical power. They are formulated as follows:

$$P_m = K_{p-f}\,(W^* - W_{measured}) + P^* \tag{2.4.6}$$

$$E = K_{q-v}\,(Q^* - Q_{measured}) + V^* \tag{2.4.7}$$

where K_{p-f} and K_{q-v} are gain parameters of the two characteristic equations. The calculated emulated mechanical power and voltage are then supplied to the VSG model, and the virtual voltages and currents are produced. They are supplied to the inner voltage and current control loops illustrated in figure 2.22, which regulates the power converter. Using the same design parameters of the previous subsection, active and reactive power-sharing performance is obtained as in figure 2.27. The two inverters' responses are identical, even when a disturbance load was introduced between (0.5 sec.) and (1.5 sec.), which indicates successful power-sharing.

However, when line parameters were doubled, which implies increased distance between the power converters, differences began to appear between the inverter's re-

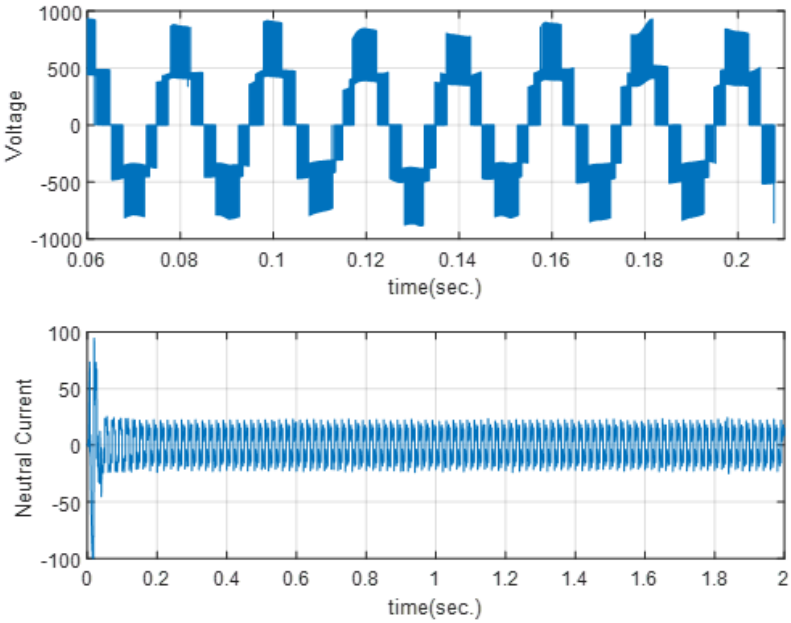

Figure 2.20: Response of the inverter.

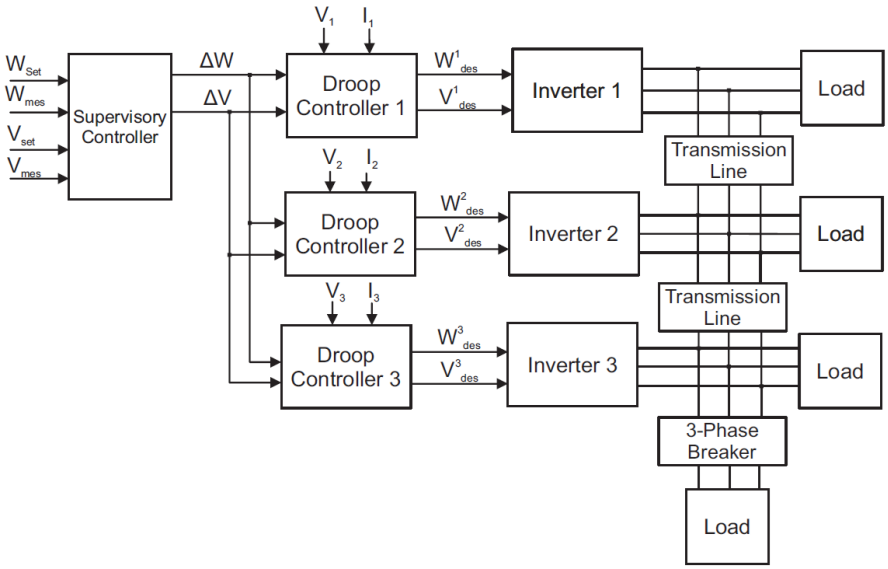

Figure 2.21: Configuration of parallel inverters system with supervisory controller.

sponses as seen in figure 2.28. Active and reactive power responses of the first inverter lag behind the second one. This appeared due to the added distance, which increased response delay time. Nevertheless, the power-sharing process is well-maintained.

The voltage and frequency responses of the two inverters are exhibited in figure 2.29. Once again, the lagging behavior can be observed in the frequency responses. Voltage and frequency changes correspond to the VSG model function, which regulates disturbances by changing operating conditions. These variations and fluctuations are within the range of allowable operating standards IEEE std 1547-2018.

The angular velocities of the two virtual machines responsible for these regula-

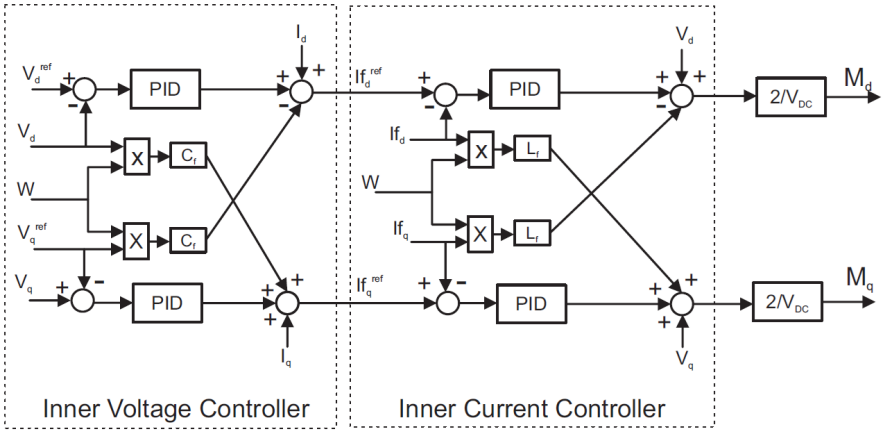

Figure 2.22: Inverter inner voltage and current controllers.

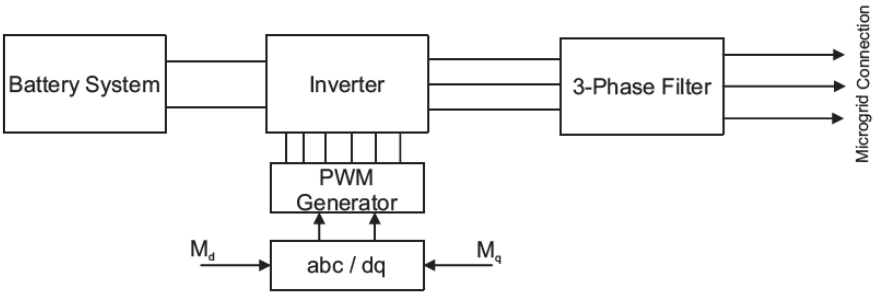

Figure 2.23: Integration of battery system to the islanded Microgrid.

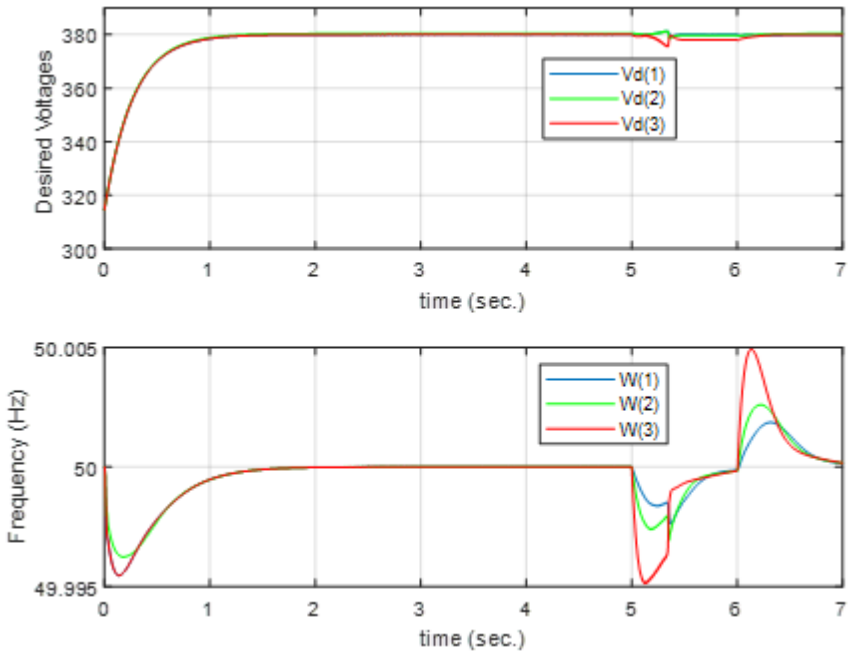

Figure 2.24: Voltage and frequency responses of parallel inverters.

tions and compensations are shown in figure 2.30.

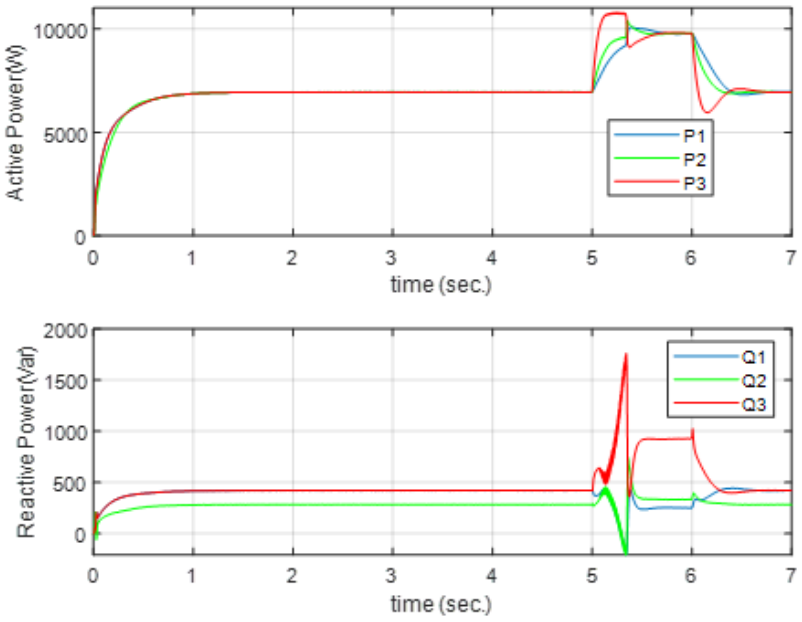

Figure 2.25: Power-sharing response of parallel inverters.

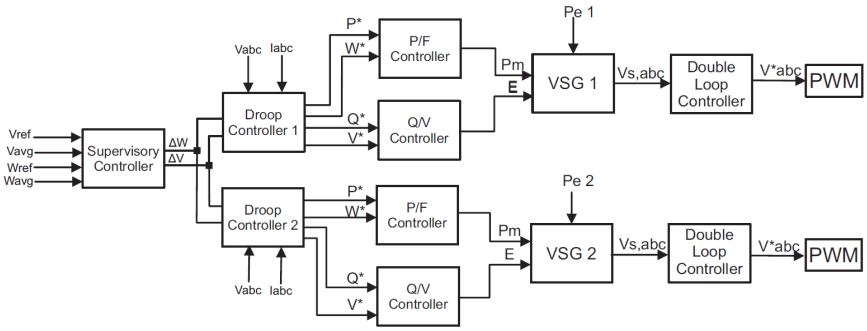

Figure 2.26: Configuration of modified parallel inverters for VSG.

2.5 Implementation Recommendation

Based on the nature of the regulated electrical complex and the capacity of local resources, the choice of the employed energy management algorithm might change. As previously demonstrated in this chapter, each method has its merits and limitations in dealing with specific operational scenario. Therefore, this section attempts to formulate recommendations about the implementation of each method in the addressed warehouse operation. The recommendations are as follows:

1. For grid-tied electrical complexes, grid-supporting droop controller or the current injection based on sliding mode control methods are utilized. While islanded warehouses employ fuzzy energy management or the droop controller based on VSG.
2. The grid-supporting droop control method regulates the operation of a bidirectional AC/DC converter. This indicates that it can simultaneously extract the energy from multiple local sources and inject it into the AC side of the grid. Changing the active

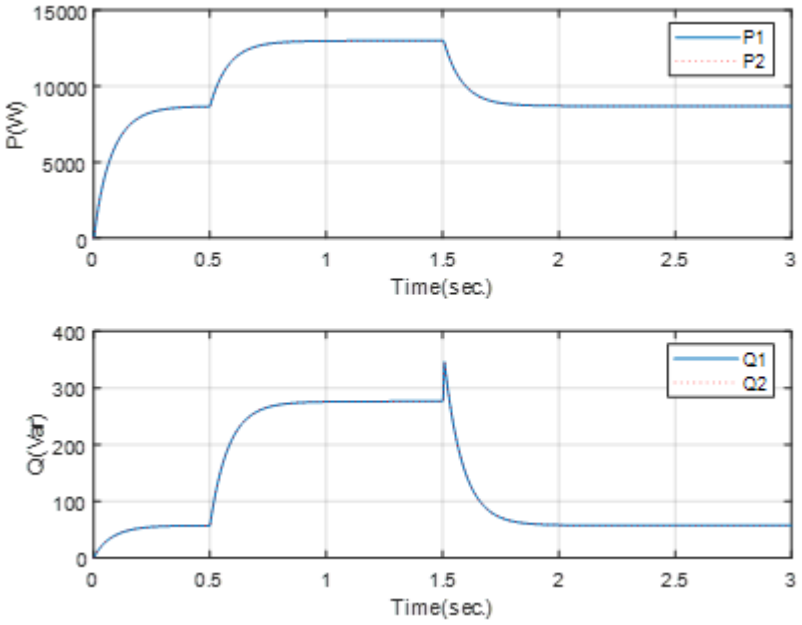

Figure 2.27: VSG active and reactive power responses.

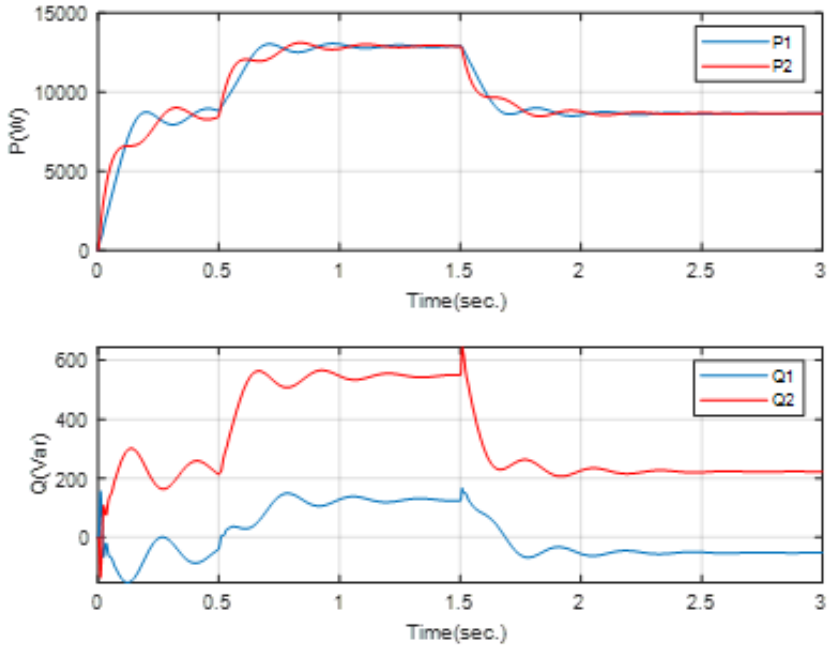

Figure 2.28: VSG active and reactive power responses, double line parameters.

and reactive power set points of the algorithm can draw the energy from the AC to the DC side of the complex. Therefore, this method provides more flexibility when number of local resources are connected to the same DC bus in a warehouse operational scenario.

3. The current injection method based on sliding mode control is mainly used with one specific energy sources like battery system. Unlike the grid-supporting droop controller it does require a well-established mathematical model of the regulated

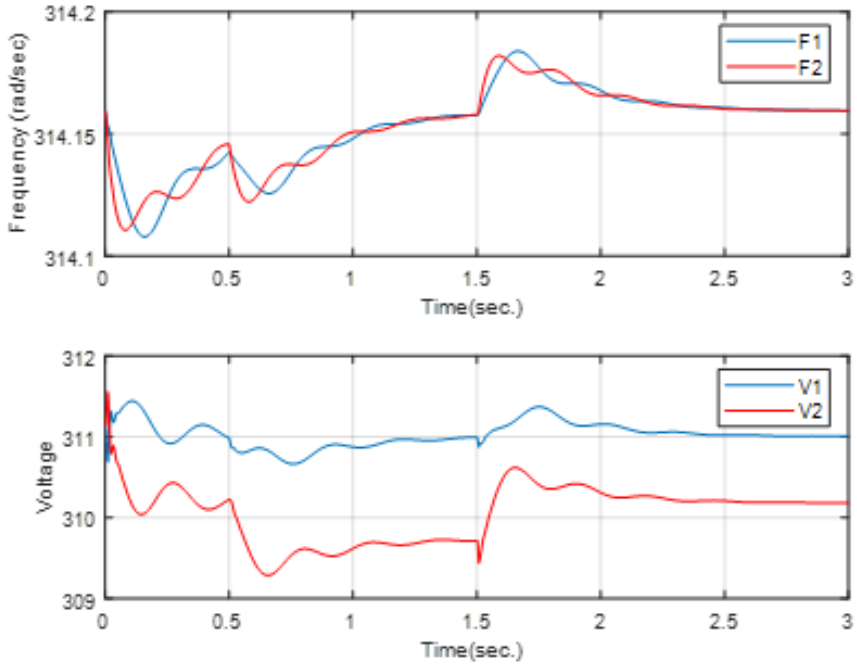

Figure 2.29: VSG voltage and frequency responses.

power converter. However, the extracted energy level regulation is slightly easier than the previous method due to the utilized the grid contribution parameter which has full control over the reference currents.

4. For medium-sized warehouses where only limited power lines are considered, fuzzy management regulator can be used to transfer the energy between different electrical complexes at the DC level. This method is associated with its simplicity and the ability to deal with uncertain measurements and complicated loads. It is designed to efficiently inject only the required energy into the load complex without a previous knowledge about the load nature or model.
5. Islanded electrical complexes with distributed components and pulsating loads suffer from inertial response deterioration. Droop control method with VSG integration can be used in this case to alleviate this problem and achieve power-sharing between different generators and loads separated by long distances. Large-sized warehouses with significant number of stacker crane complexes can utilize this method to ensure successful power distribution and faster disturbances regulation.

2.6 Conclusion of chapter two

In electrical complexes, energy management controllers are developed to regulate extracted, stored, and consumed energy. These control and management algorithms are deployed on power converters connecting different system components to retain the delivered power quality and accomplish power-sharing targets. Grid-tied and islanded

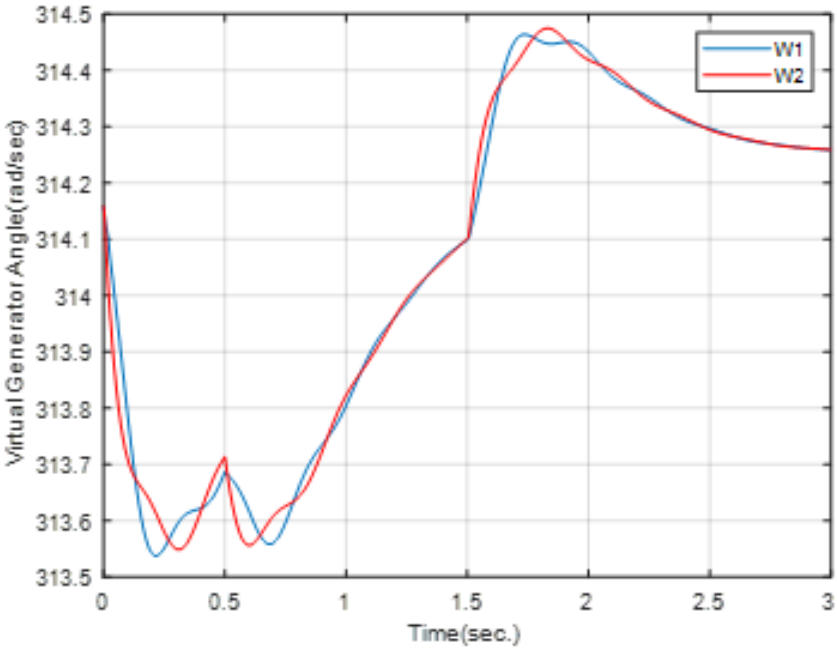

Figure 2.30: Virtual generator angular velocities.

Microgrid configurations were considered and studied. Different algorithms were proposed for these two modes of operation to ensure performance. Based on the application, Grid-supporting droop control and current injection algorithms were proposed for grid-tied Microgrid system architecture. Whereas, the fuzzy energy management system was developed for battery resources regulation in an islanded Microgrid scenario. The implementation of droop control algorithms in islanded Microgrids is also possible but with certain modifications including the integration of a supervisory controller and VSG model blocks. Developed controllers proved their effectiveness and can be utilized in hoist and transport applications addressed in this dissertation as part of the battery-based power supply system.

Chapter 3

Battery Chargers and Controllers

Battery systems are essential components in the proposed reliable power supply system. The topology of their charging station and the employed controllers are largely influenced by the addressed application. Understanding the architecture of each utilized converter, its characteristics, and the particularity of each design is an important aspect of the development of battery-integrated applications [76]. This chapter is devoted to the study and evaluation of different battery charging stations and their affiliated technologies. As previously stated, battery chargers consist of an AC/DC rectifier stage and a DC/DC converter stage. Different combinations of power converters on both stages can produce distinctive results, which assist in evaluating the design applicability. The stability of the DC bus, the achievable output voltage range, power rating, and switching losses magnitude are some of the important factors considered while nominating a possible charging topology. A comparative study of different charging architectures commonly used in the industry is provided to establish baseline performance. A wide output range LLC resonant converter controlled by a phase-shift algorithm was proposed to implement the DC/DC charging stage of the battery system. A simulation and practical study are conducted to assess the computer model's accuracy. Different energy-exchanging technologies used in larger electrical complexes are also addressed and evaluated.

3.1 Comparative Study of Standard Chargers

The DC/DC converter is regarded as the technological challenge in battery charger development. A high-accuracy controller is required to operate the converter's switching devices to regulate the voltage and current on the battery terminals. This converter is also associated with elevated switching losses due to the high switching frequency of operation. The transistor switching frequency in this stage is higher than the AC/DC stage because of the utilized high-frequency transformer required for galvanic isolation. Nevertheless, the AC/DC converter selection is also an important element in the overall performance of the charging station. This converter regulates the DC-bus voltage and

compensates for deviations caused by the load variations. Therefore, different converter combinations on the two stages can lead to entirely different results and performance.

The four converters illustrated in figures (1.5 and 1.6) are considered in this section. The first examined combination is between the Vienna rectifier and the LLC resonant converter. The resonant frequency was specifically designed based on the C_r and L_r elements of the resonant tank circuit. A detailed design procedure for these parameters will be provided in the next section. The rectifier regulates the DC line voltage around (900 V) utilizing the control structure exhibited in figure 1.8, while the LLC converter used the variable frequency controller shown in figure 1.9. The pulse generator function utilized in this design is demonstrated in Appendix C. Figure 3.1 shows the battery response to the examined charger topology.

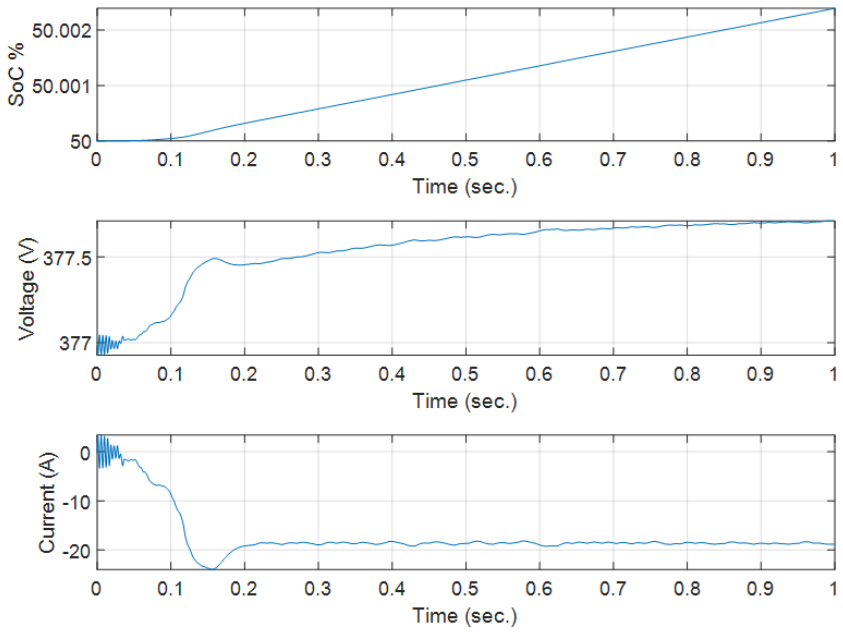

Figure 3.1: Vienna rectifier & the LLC converter battery response.

The battery's SoC is increasing which indicates commence of the charging process. Moreover, the battery voltage encountered some insignificant dynamics in reaction to the supplied power, while the battery current holds a negative value fluctuating around the (-19 A). It is important to point out that, the LLC converter could not accomplish a higher charging current regardless of the adaptation in the PID controller parameters. The control scheme itself restricts current and voltage range regulation, which limits its usability. On the other hand, figure 3.2 reveals the average switching losses of the DC converter that appear to have a very reasonable level, while the DC voltage could not achieve the (900 V) level which explains the power density reduction experienced by the output.

The second charger complex incorporates the Vienna rectifier with the phase-shift converter topologies. The phase-shift function used by the control structure in figure 1.9 is demonstrated in Appendix C. An increased battery current injection can be

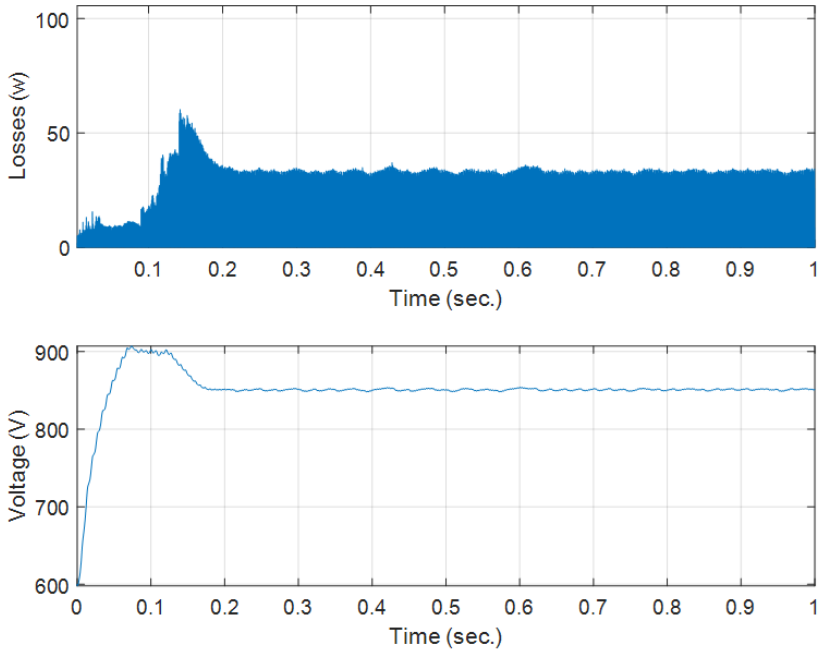

Figure 3.2: Vienna rectifier & the LLC converter losses and DC voltage.

instantly noticed in figure 3.3. The phase-shift control algorithm has a wider achievable voltage and current regulation range. In practice, the controller can attain any required current value within the converter design limitation. However, the switching losses of the input transistor bridge were higher than in the previous case.

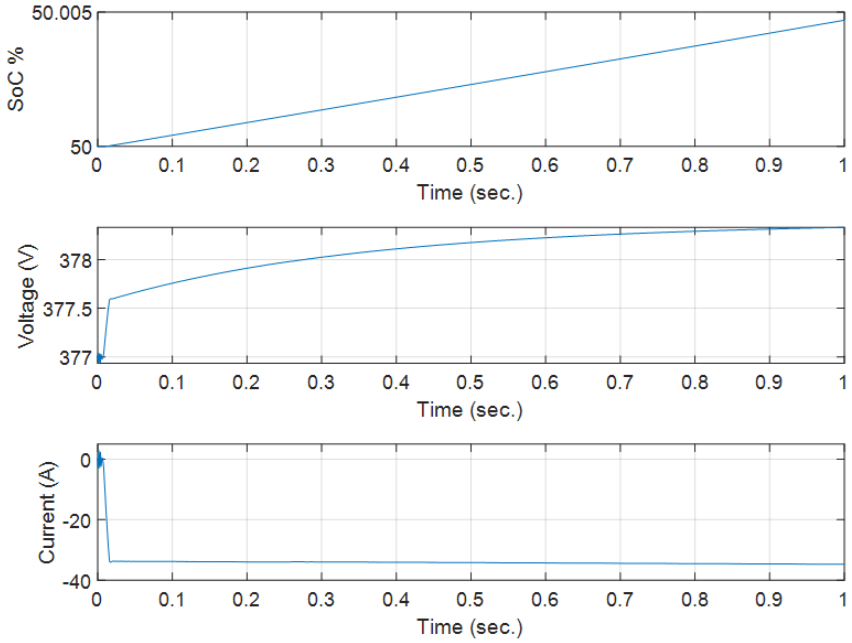

Figure 3.3: Vienna rectifier & the phase-shift converter battery response.

Although the same AC/DC rectifier was used in the simulation, a robust and rapid DC voltage regulation was observed in figure 3.4. This undoubtedly shows that the obtained performance depends on the combination of these topologies rather than their

separate characteristics.

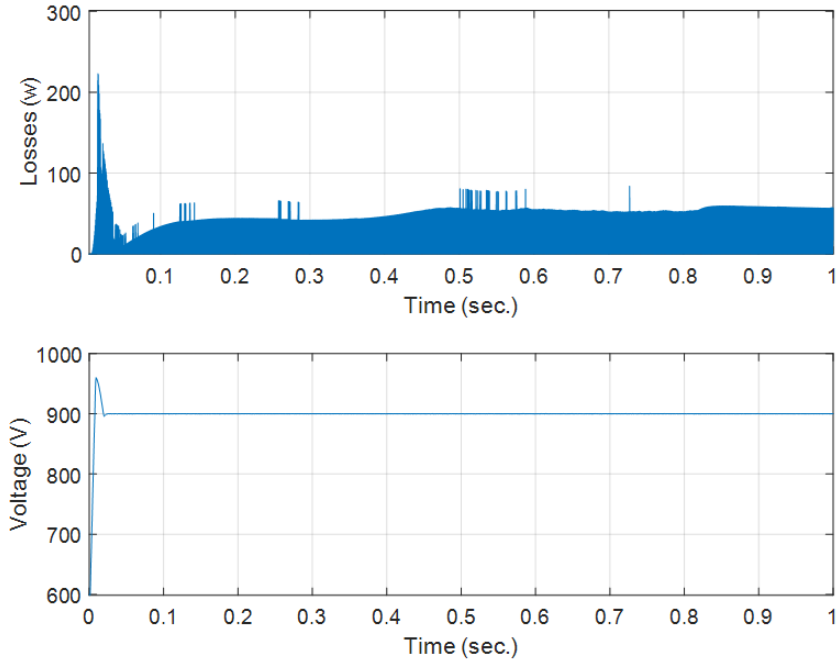

Figure 3.4: Vienna rectifier & the phase-shift converter losses and DC voltage.

The active front-end AFE power rectifier is combined with the LLC resonant converter and the battery response is presented in figure 3.5. Similar to the previous case, the current is not precisely regulated by the LLC control mechanism, although it achieved higher charging current injection.

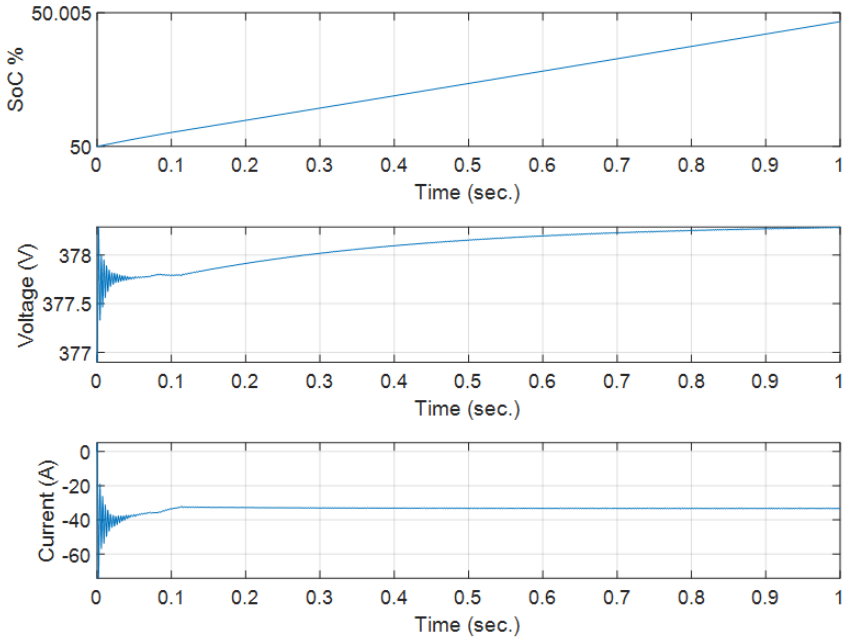

Figure 3.5: AFE & the LLC converter battery response.

The switching losses of the LLC converter are demonstrated in figure 3.6. As seen in the figure, the level of losses is unreasonably high, with expected operational

problems in practice. The converter efficiency is quite low due to the dissipated power, which indicates a re-design procedure must be executed. The resonant tank was remodeled around a lower resonant frequency of (60 kHz) which significantly improved the efficiency as shown in figure 3.7.

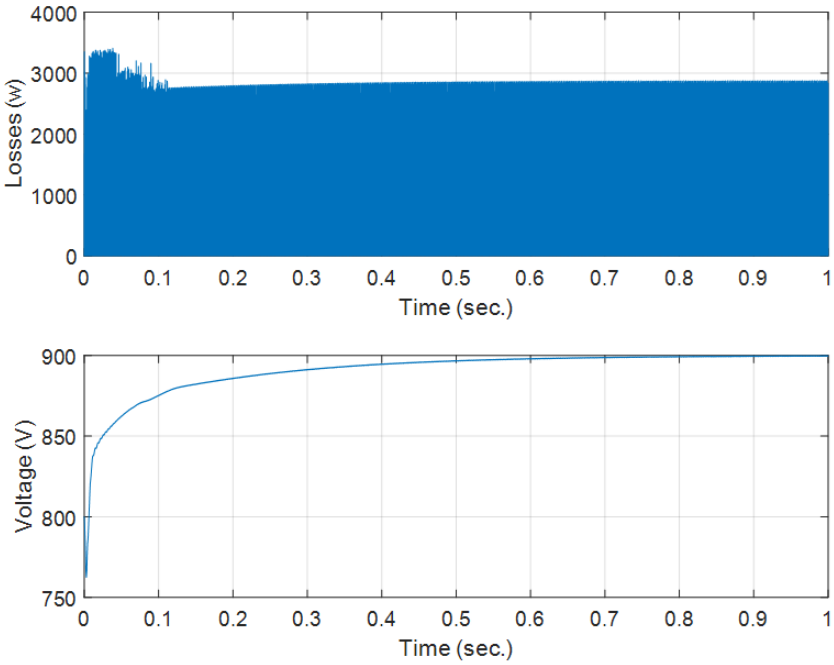

Figure 3.6: AFE & the LLC converter losses and DC voltage.

However, the battery current regulation performance deteriorated with the control system failing to achieve any required set-point. On the other hand, the DC-bus voltage response of the AFE converter was demonstrated in both cases starting from (800 V). This is due to the per-charging process of the DC-bus capacitor, which is necessary for stable charging station operation. This is considered a limitation to the AFE applicability to charging applications.

The final combination examined in this section is between the AFE and the phase-shift converter. Figure 3.8 exhibits the battery response of the tested charger with perfect regulation performance. Nevertheless, the results of the switching losses in figure 3.9 reveal that the efficiency of such topology is approximately less than (70%). The power losses can be attenuated by decreasing the switching frequency. However, an increased transformer size is implicated by such a solution.

Finally, it should be mentioned that the total harmonic distortion tests showed a (5.7%) distortion rate in chargers implementing Vienna rectifier topology, while AFE achieved less than (2.7%). The previous comparative study establishes the need for a modified topology, that incorporates the merits of both LLC and phase-shift converters.

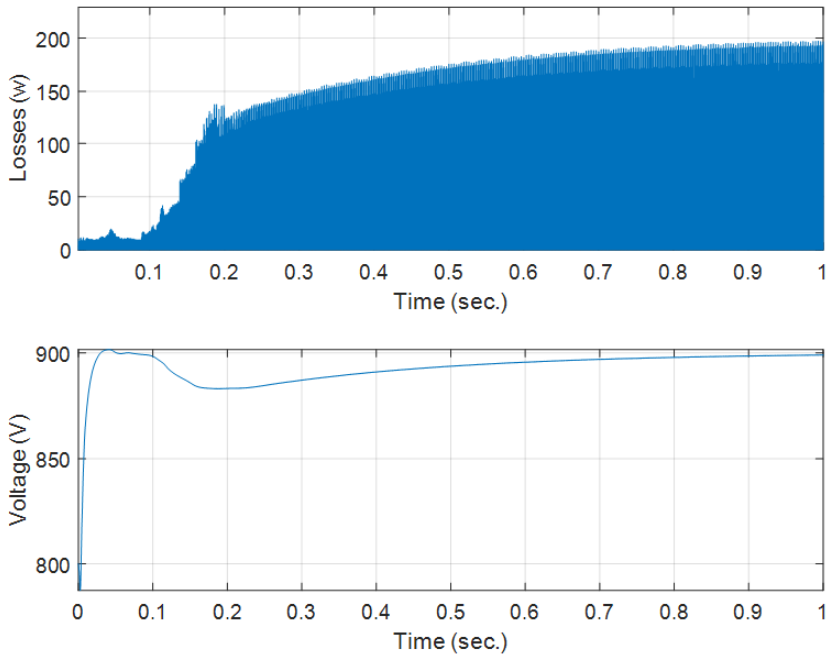

Figure 3.7: AFE & the LLC converter improved efficiency.

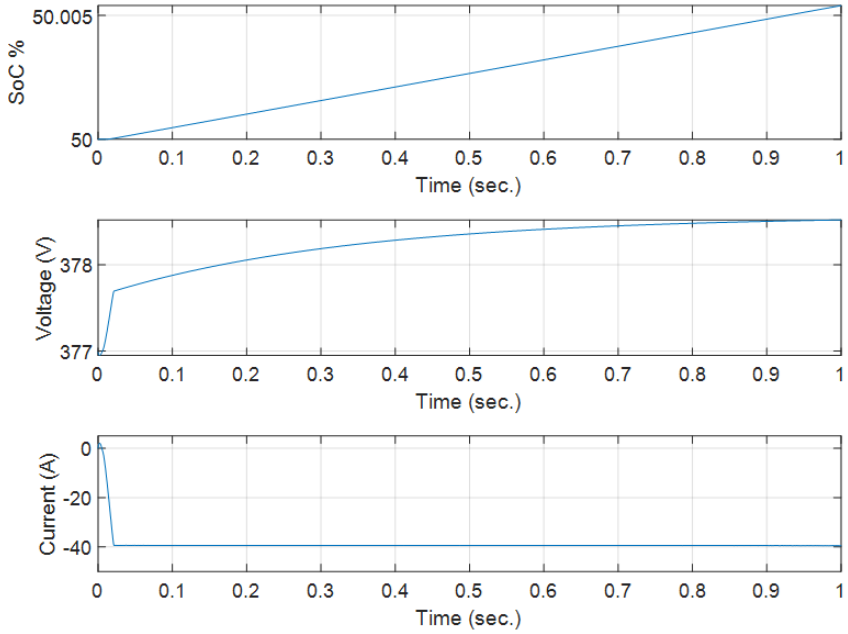

Figure 3.8: AFE & the phase-shift converter battery response.

3.2 Wide Voltage Range LLC Resonant Converter

The previous discussion implicated the necessity of developing an enhanced charging technology with a wider output-voltage range and acceptable loss level. The LLC resonant converters generally performed better than the phase-shift variant in terms of switching losses, which is due to its unique architecture allowing soft-switching near the resonant frequency. On the other hand, the phase-shift algorithm delivered satisfactory regulation capabilities allowing a wider operational range. The combination of

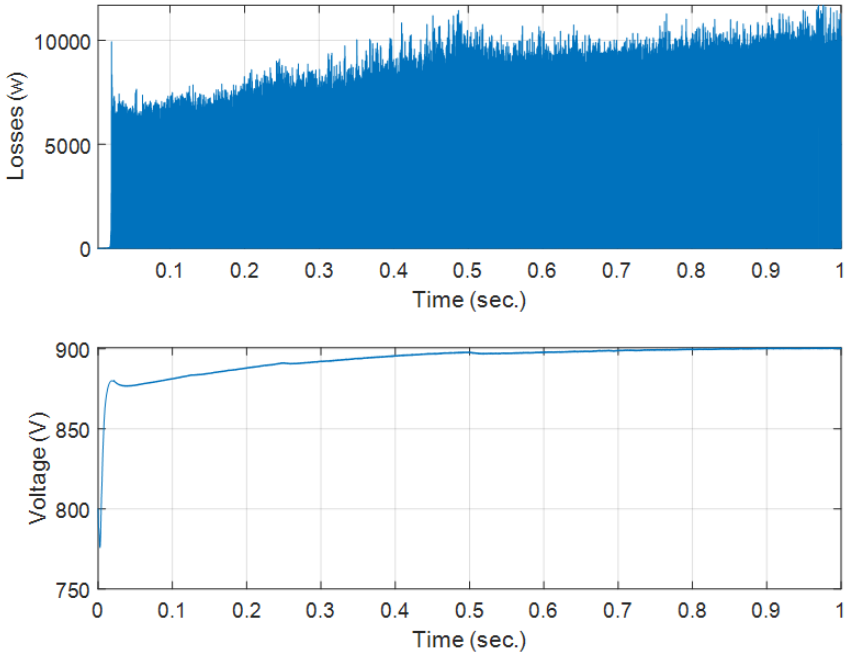

Figure 3.9: AFE & the phase-shift converter losses and DC voltage.

these two technologies has already been established in the literature, but with diverse bridge and transformer configurations [124; 125] or with a more complicated control mechanism [126]. The proposed wide voltage range converter is composed of an LLC resonant topology controlled by a phase-shift algorithm. The LLC converter functions at a specific constant switching frequency near the resonant achieving reduced losses, while the phase difference between the input bridge legs is formulated by the voltage and current control loops. The converter structure simulated in MATLAB/Simulink environment is demonstrated in figure 3.10.

3.2.1 Simulation Based Study

The first harmonic approximation (FHA) method was utilized to design the resonant tank parameters by compromising the converter gain with operating frequency. The objective is to investigate the gain-frequency characteristic to identify operating points for various operational requirements. Although the resonant frequency F_{res} is assumed constant, changing the switching frequency value around it can offer more voltage gain or reduced switching losses. The designed converter power rating was set to (7.5 kW) based on practical constraints and requirements. Multiple modules could be integrated in parallel to obtain a higher power rating. Ideally, the converter is designed to regulate the voltage at the range of (0-350 V) with passive loads. Initially, IGBT transistors were selected for the converter construction with a maximum frequency limited by 100-120 kHz. However, during the prototyping process, significant switching losses were experienced, which did not allow the use of typical radiator size. Therefore, MOSFET technology was used, which significantly reduced losses and made it possible to

employ a compact active cooling system.

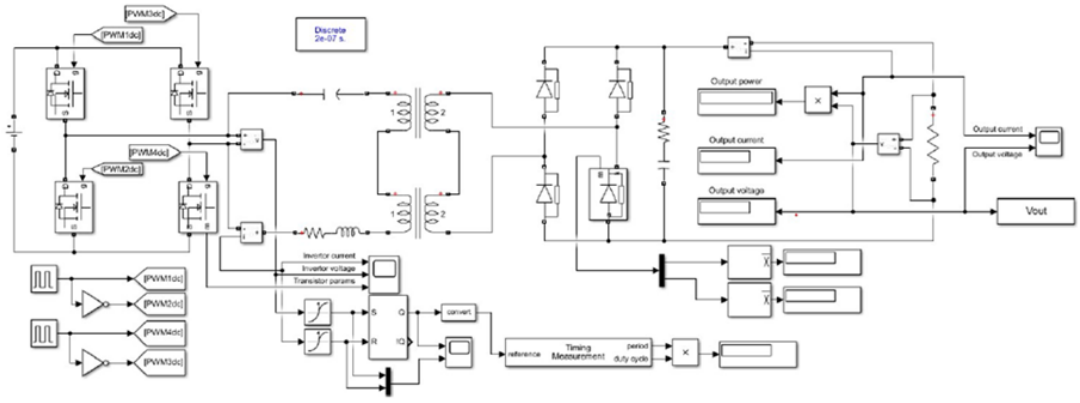

Figure 3.10: LLC resonant converter Simulink model.

The resonant frequency F_{res} was set to (60 kHz), while the maximum frequency F_{max} was bounded at (100 kHz). The transformation ratio of the high-frequency transformer is calculated as:

$$n = \frac{V_{out}}{V_{in}} \tag{3.2.1}$$

The quality factor of the resonant circuit Q_e and the transformer magnetization inductor to the resonant tank inductor ratio L_e were determined using an iterative manner. Initially, arbitrary values were selected before conducting the optimization procedure, based on certain specifications. The optimization criteria were to achieve a (1.3) voltage gain that ensures the required output voltage is reached, even when a supply voltage drop is experienced. The selected parameters influence the choice of maximum gain at the rated load which affects the converter losses. Then, the Q_e and the L_e parameters were set to (0.5) and (4.5) respectively. Then the equivalent nominal resistance at nominal parameters is calculated according to:

$$R_e = \left(\frac{8n^2}{\pi^2}\right) * \left(\frac{V_{out}}{V_{in}}\right) \tag{3.2.2}$$

The values of the resonant tank elements are determined by:

$$C_r = \frac{1}{2\pi Q_e F_{res} R_e} \tag{3.2.3}$$

$$L_r = \frac{1}{(2\pi F_{res})^2 C_r} \tag{3.2.4}$$

$$L_m = L_n L_r \tag{3.2.5}$$

Now, the transfer characteristic of the LLC converter is constructed by, first, checking the alignment of the designed parameters with the converter requirements. The fundamental resonant frequency of the circuit is calculated as:

$$F_0 = \frac{1}{2\pi\sqrt{(C_r L_r)}} \tag{3.2.6}$$

While the quality factor of the load circuit at nominal operation is:

$$Q_e = \frac{\sqrt{(C_r/L_r)}}{R_e} \tag{3.2.7}$$

The transfer function of the LLC converter, based on variable frequency and the design parameters, is then given by [127]:

$$M_g\left(Q_e L_n F_n\right) = \frac{L_n F_n^2}{\sqrt{\left[\left(L_n+1\right)F_n^2-1\right]+\left[\left(F_n^2-1\right)F_n Q_e L_n\right]}} \tag{3.2.8}$$

The above voltage gain equation is a function of the normalized frequency F_n, which reaches unity at resonant frequency F_{res}. The gain was also normalized to achieve the required (500 V) output at unity gain. The acquired parameters were implemented on the design in figure 3.10, and the simulation results are presented in figure 3.11. Several load ratings were tested to exhibit their influence.

Comparing the analytical results with the simulated ones requires incorporating load change effects into the design equations. The equivalent resistance represented in equation 3.2.2 is modified as:

$$R_e(R_{load}) = \left(\frac{8n^2}{\pi^2}\right) * R_{load} \tag{3.2.9}$$

While the quality factor of the resonant circuit Q_e becomes:

$$Q_e(R_{load}) = \frac{\sqrt{(C_r/L_r)}}{R_e(R_{load})} \tag{3.2.10}$$

The gain magnitude function is also modified to be:

$$M_g\left(Q_e L_n F_n\right) = \frac{L_n F_n^2}{\sqrt{\left[\left(L_n+1\right)F_n^2-1\right]+\left[\left(F_n^2-1\right)F_n Q_e(R_{load}) L_n\right]}} \tag{3.2.11}$$

During simulation and calculations, the R_{load} is assumed as percentage of the total load resistance for convenience. The load rate is determined by:

$$Load\% = \frac{U_{in} * 100\%}{R_{load} I_{out}^{nom}} \tag{3.2.12}$$

where U_{in} is the experimental input voltage and I_{out}^{nom} is the normalized output current. The analytical and simulated results converge around the resonant frequency value and diverge elsewhere, as seen in figure 3.15. This implies the MATLAB model accuracy compared to the design equations. It is also worth mentioning that the simulated converter achieved sufficient voltage regulation performance between (0-350 V) with complete transistors turn-off at zero volts. Table 3.1 illustrates the design parameters utilized in the simulation.

Table 3.1 — LLC converter design parameters

Parameter name	Value	Units
U_{in}	200	V
I_{out}^{nom}	15	V
R_{load}	$129.85, 26.68, 17.06$	ω
C_r	204.1	nF
L_r	38.9	μH
L_n	4.138	μH
L_m	160.98	μH
F_{res}	56.48	kHz

Figure 3.11 shows the simulated battery response of the proposed wide-range resonant converter. For this specific test, a Vienna rectifier was employed to supply a constant DC voltage. However, substituting it with an AFE rectifier had minimal effect on the obtained results. This resulted from the increased controllability of the DC/DC stage by employing the phase-shift algorithm while varying the switching frequency around the resonant. The converter current experienced fast dynamics with increased range.

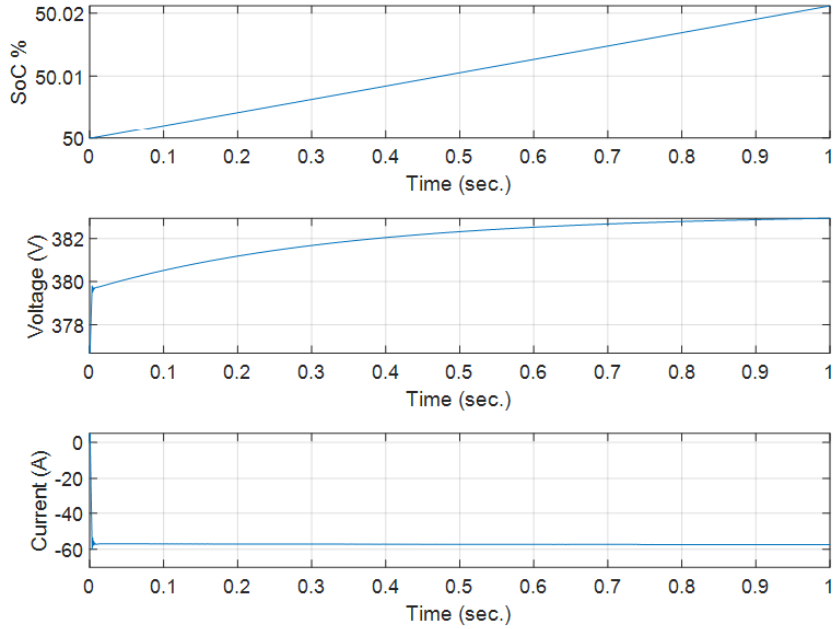

Figure 3.11: Wide range LLC converter battery response.

The switching losses of the converter are demonstrated in 3.12 with an average level of less than (700 w). The converter can work with a typical active cooling system. It must be pointed out that the switching frequency was set to (52 kHz) during the simulated test. Normally, such converters are operated with a frequency lower than the resonant to guarantee high power density. Nevertheless, the losses can be reduced

further by slightly moving the frequency operating point around the resonant. This compromises the current regulation range but is beneficial with less demanding loads. Appendix (D) exhibits the results of changing the switching frequency of the proposed converter while maintaining other parameters.

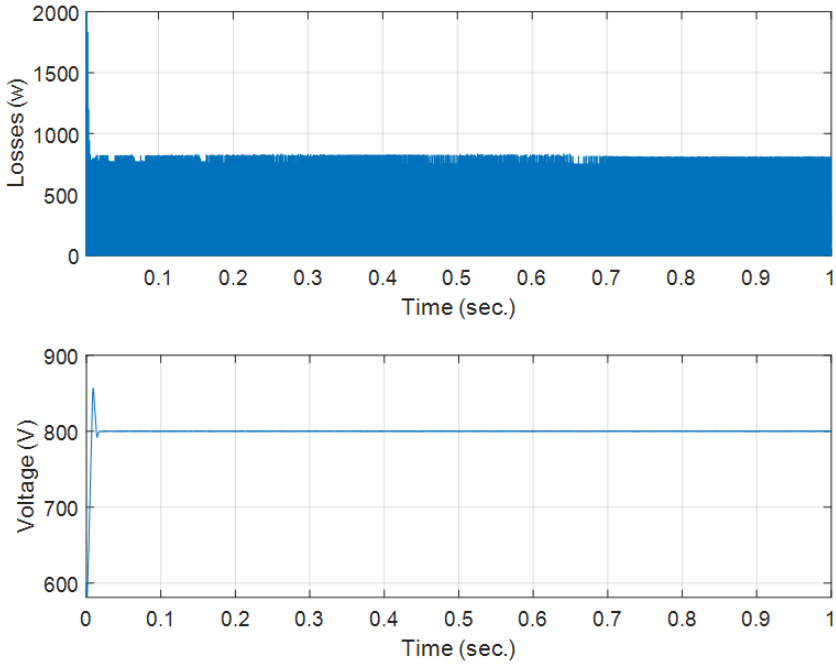

Figure 3.12: Losses and DC voltage response of the proposed charger setup.

3.2.2 Practical Implementation and Evaluation

The objective of this experimental study is to confirm the findings of the simulation and analytical results. The experimental setup is shown in figure 3.13. The input of the converter consists of a bulky capacitor bank to stabilize the input DC voltage of the full-bridge inverter. Silicon carbide MOSFETs were used to implement the bridge circuit since they can withstand higher switching frequencies while maintaining relatively low losses. Nevertheless, an active cooling system was utilized for each leg of the inverter and the output diode bridge. Output capacitor banks were used to stabilize the voltage of the inverter.

The implemented converter is demonstrated in figure 3.14, where transformers and inductors were specially designed for better isolation and minimum losses. The two transformers were carefully constructed to be identical. However, some differences were practically expected. Designed system parameters are slightly different from the simulated ones due to hardware availability restrictions. During the operation, the input inverter bridge of the LLC converter recorded a temperature of 52 degrees, which is manageable by employing proper cooling systems.

Figure 3.15 compares the simulated and analytical result's accuracy with the prac-

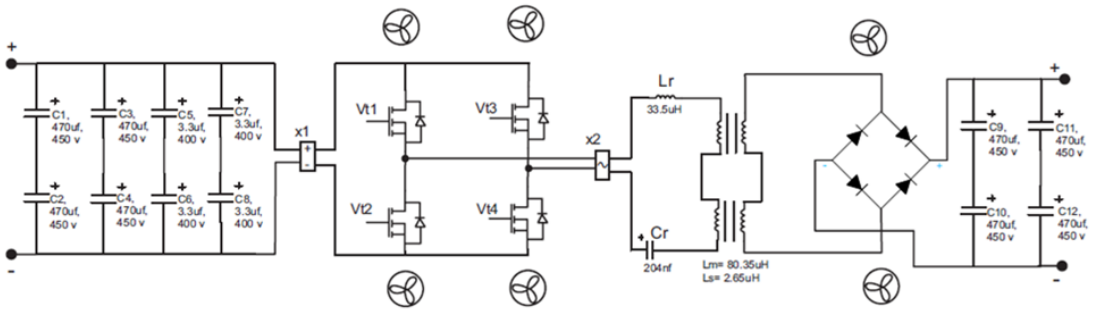

Figure 3.13: LLC resonant converter hardware implementation.

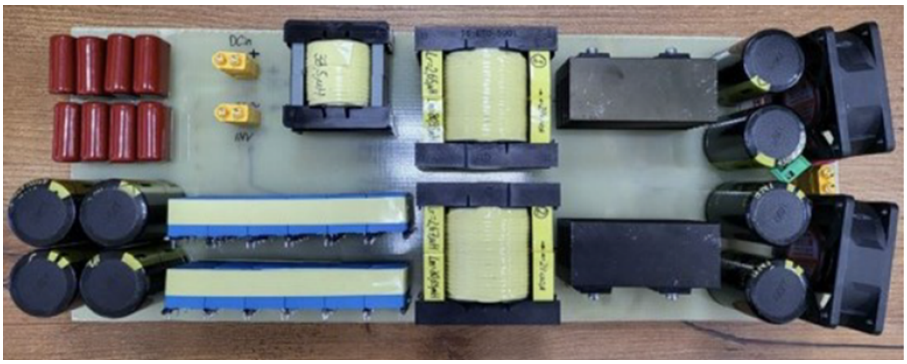

Figure 3.14: Circuit layout of the experimental setup.

tically acquired ones. In sub-resonant frequencies, the simulated and practical converter characteristics were almost identical, with insignificant error margins. However, the two curves diverge from each other at higher frequencies, indicating inaccuracies. The analytical results demonstrated poor performance in predicting converter gain, especially at higher than resonant frequencies. Nevertheless, all characteristic curves converge at the operational region around the resonant frequency. This indicates the successful implementation of the FHA method and the adequacy of simulated MATLAB models for testing and validation of this converter.

3.3 Exploring the V2G Technology

The vehicle-to-grid V2G terminology represents the transfer of an electric vehicle's stored energy to the power grid during bottleneck conditions to perform services like peak shaving and reactive power compensation. Although the concept was developed based on battery systems of electric vehicles, it can be generalized to include various battery-supported applications. For instance, an industrial electrical complex integrated with a battery system can exploit this technology when excess energy is stored or generated locally. In the hoist and transport sector, this condition is frequently encountered during regenerative operation modes and extensive power production of any locally integrated renewable energy generators. The critical services offered by the V2G

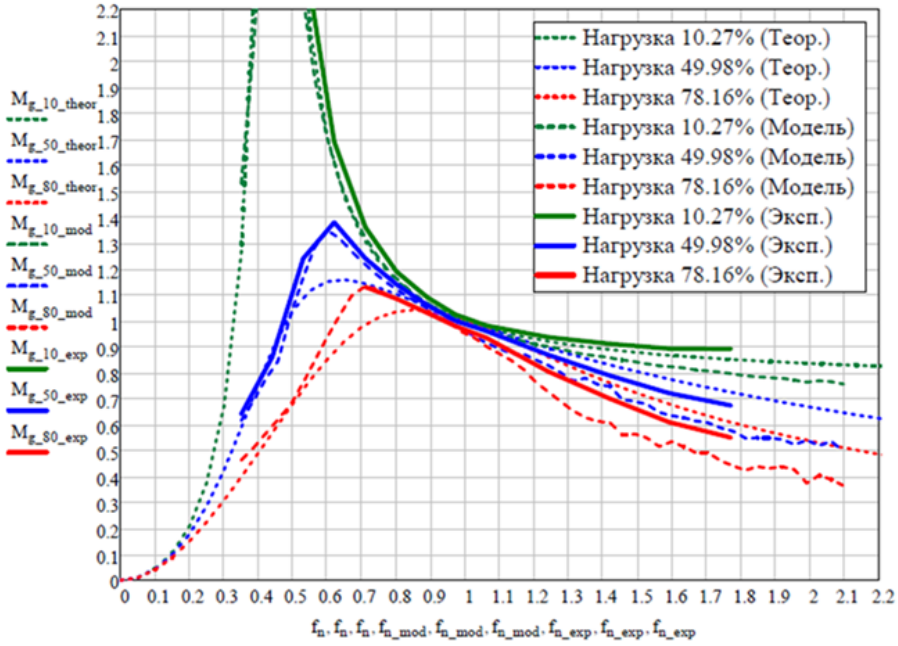

Figure 3.15: Theoretical, Simulation, and Experimental results of the resonant converter.

technology could be compensated by the grid operator using intensives in exchange for granting access to the complex power supply system. On the other hand, uncontrolled bidirectional power exchange between battery systems and the grid can cause serious problems including voltage sag, swells, shorter time of system's power components, and degradation of battery's life cycle [128]. The purpose of this section is to introduce this technology and highlight its operation in the electrical complex. Theoretically, this technology is quite similar to the grid-supporting controllers in grid-tied Microgrids explored in the second chapter. However, here it addresses battery-centered applications. An electric vehicle charging station integrated into a solar energy generator is demonstrated in figure 3.16 as an example of this technology. The utilized power converters and their control systems were previously explained and discussed. The charging station employs a solar generator unit to supply the battery demand. When the solar generation level is low and the V2G technology is not invoked, the grid transfers energy to the battery system and charges the electric vehicle. Once the V2G energy transfer is enabled, the bidirectional AC/DC converter starts injecting power into the grid. Depending on the solar generation level, the battery system and solar panels cooperate to supply the required injected power.

Figure 3.17 exhibits the three-phase voltages and currents of the grid during G2V operation. A phase difference of 180 degrees was observed between the voltages and current responses. This implies that the power was extracted from the grid and supplied to the charger complex.

On the other hand, when the direction of power is reversed in V2G technology, the three-phase voltages and current become mutually in-phase with each other, as seen in figure 3.18. This indicates the power flow from the battery complex to the unity

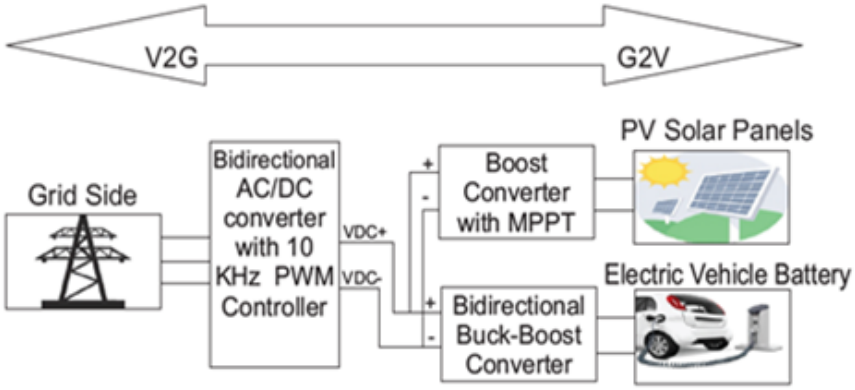

Figure 3.16: EV charging station with G2V and V2G power flow.

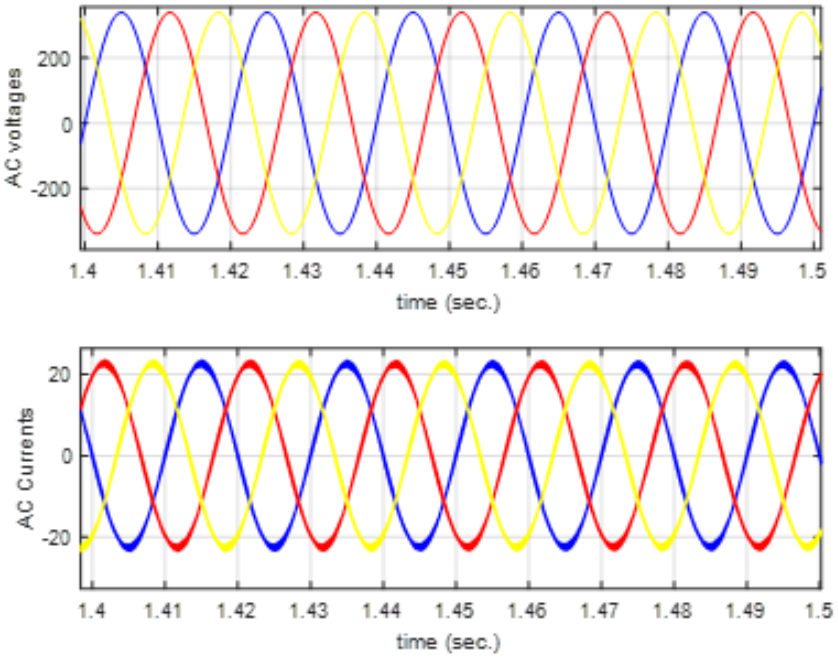

Figure 3.17: Grid side voltages and currents in G2V mode.

grid. Hence, the bidirectional energy transfer between the battery-supported electrical complex and the grid has been established.

3.4 Exploring the V2V Technology

Another concept that addresses the energy exchange of battery systems in technical complexes is the vehicle-to-vehicle V2V technology. It describes the power exchange process between two electric vehicles attached to a charging station. However, similar to the previous principle, the terminology is extended to covert power-exchanging electrical systems in multiple battery complexes. An example of this appli-

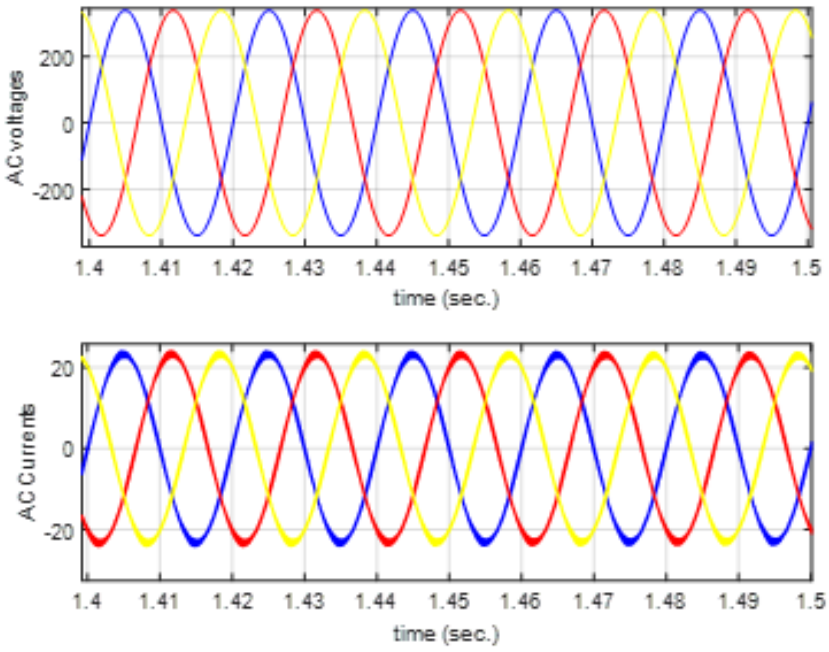

Figure 3.18: Grid side voltages and currents in V2G mode.

cation is the exchanged power between different battery-operated stacker cranes in an automated warehouse. From a utility perspective, this technology can alleviate some issues related to the high energy consumption of certain industrial complexes on low and medium-level distribution networks. These issues may include power quality degradation and the aging-decay acceleration of power system components [129]. This technology utilizes the stored power in posed complexes and injects it into an active complex with soaring demand. When the original objective of this technology is considered, the power system can be configured as a common-AC or common-DC architecture.

Figure 3.19 demonstrates the common AC line configuration with two electric vehicles connected to two different charging stations. The problem with this system architecture is the increased power losses with multiple energy transformations and the harmonic injection of the donor vehicle inverter. This significantly impacted the power quality on the AC side and produced impractical operation.

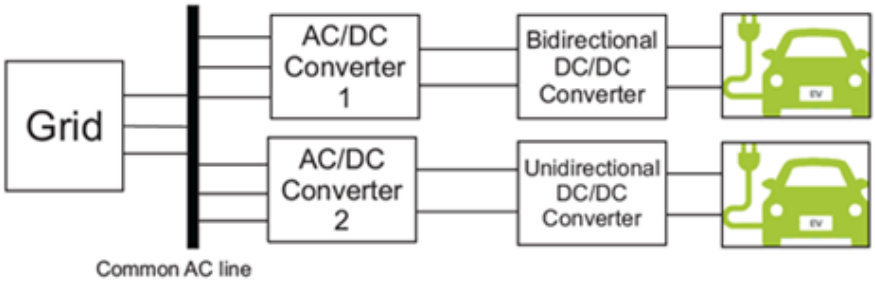

Figure 3.19: V2V common AC line architecture.

On the other hand, the common DC line configuration eliminated the AC transfer stage of the donor vehicle power and directly utilized the DC converters for the energy exchange process. This reduced losses and protected the main grid from harmonic injections. The architecture of this technology is exhibited in figure 3.20.

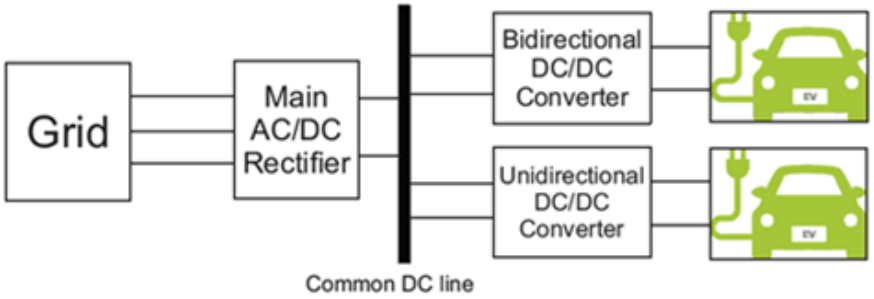

Figure 3.20: V2V common DC line architecture.

Finally, the two battery responses are shown in figure 3.21 where the donor battery is represented by the left side figures while the receiver battery is on the right side. The donor SoC is decreasing at the same rate as receiver SoC increment. Battery current fluctuations on both responses are affected by the parameter selection of the two converter topologies. They can be improved by proper enhancement and optimization. However, the dual active bridge performance dominates the overall quality of the transferred power. Most importantly, the battery voltages demonstrated in the figure have different levels on both sides. This indicates that different devices integrated into one electrical complex can exchange power even with different power and voltage ratings.

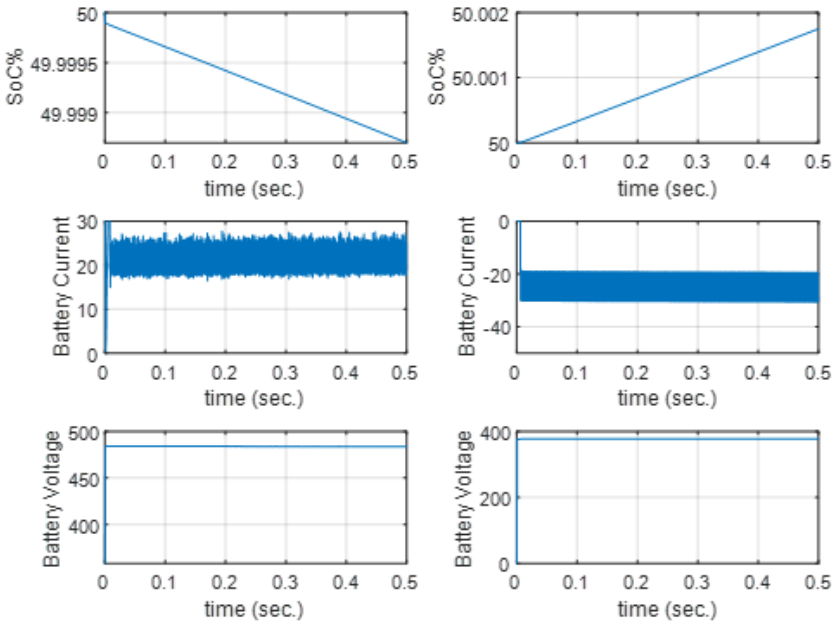

Figure 3.21: V2V batteries responses.

3.5 Conclusion of chapter three

Battery chargers are an essential component of a battery-operated power supply system. The charging station performance significantly impacts the overall efficiency of the electrical complex. In this chapter, various converters commonly utilized in charging station configuration were combined, and their performance was evaluated. The comparative study highlighted the typical issues associated with these topologies and motivated the development of better charging stations incorporating the available topologies and controllers. A wide voltage range DC/DC converter was proposed by integrating the LLC resonant converter topology with the phase-shift regulation algorithm. The developed DC converter tackled the high losses issue of the phase-shift configuration and the weak controllability of the frequency-controlled LLC converter. The converter was developed in simulation and practice to validate its performance and assess the accuracy of MATLAB/Simulink models. The results confirmed the achievement of the design requirement, and the simulation models accurately predicted the frequency-gain characteristic in the region around the resonant frequency. Finally, energy-exchanging technologies like V2G and V2V were investigated to establish their applicability in industrial electro-technical complexes. The results obtained will be used later in application-based system development.

Chapter 4

Battery Emulator

The previously developed battery system components, like energy management algorithms in Chapter (2) and the battery charging stations in Chapter (3), require a safe and versatile testing environment to validate their design. Based on the arguments presented in Chapter (1), experimenting with chemical batteries is a risky operation, especially for newly designed technologies that need final tweaking before practical deployment. Therefore, a battery system test-bed was proposed to overcome these challenges and provide the necessary system validation. It employed the same PHiL principles illustrated in section (1.7), where actual power signals are exchanged to perform the ultimate test before device commercialization. Li-ion batteries are particularly addressed in this research because of their wide range of modern applications and power-to-energy density ratio, allowing them to be incorporated into high-demand complexes. The test bench utilizes the Li-ion battery model expressed in equations 1.6.1-1.6.4 to emulate the actual behavior of electrochemical batteries in response to current changes. The nonlinear model accepts the battery current as an input and produces the voltage and SoC as an output. This chapter aims to develop a power converter-based battery emulator for testing and validating charging technologies. The emulator's test bench performance is verified both in simulation and practice.

4.1 Test-bench Configuration

Instead of utilizing complicated converters and energy management algorithms to implement the test bench, a simplified half-bridge converter layout was exploited to obtain principle results. Nevertheless, the proposed concepts can be generalized to include any controllable converter topology expecting the same results. Although the developed PHiL-based test bench concurs with the previously analyzed battery emulators in section (1.7), building blocks and equipment deployment are different in the proposed structure to ensure flexibility, efficiency, and reduced power consumption. The proposed test bench structure is presented in figure 4.1, where the objective is to test battery charger apparatuses. The test bench consists of an AC/DC rectifier and DC/DC

converter, jointly representing the charging station. Any charger topology could be connected instead of the employed one with proper modification. This part and associated controllers represent the device-under-test DUT unit.

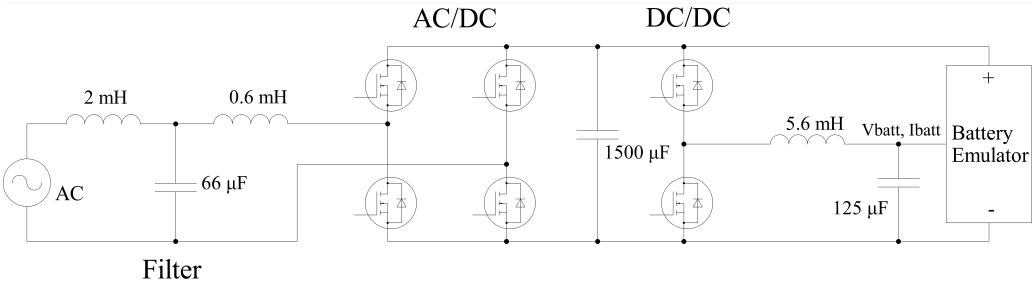

Figure 4.1: Charging station connected to battery emulator terminals.

On the other hand, the emulator block incorporates a buck-boost converter imitating battery voltage characteristics in response to input current variations. The emulator dynamics are governed by the Li-ion battery model executed on a specific processor. Emulator voltage and current regulators are employed to compensate for divergences of converter output from the modeled signals. Figure 4.2 exhibits the battery emulator circuit connected to the charging station block. Voltage and current sensors were employed to measure the induced voltage and the passed current between the two devices.

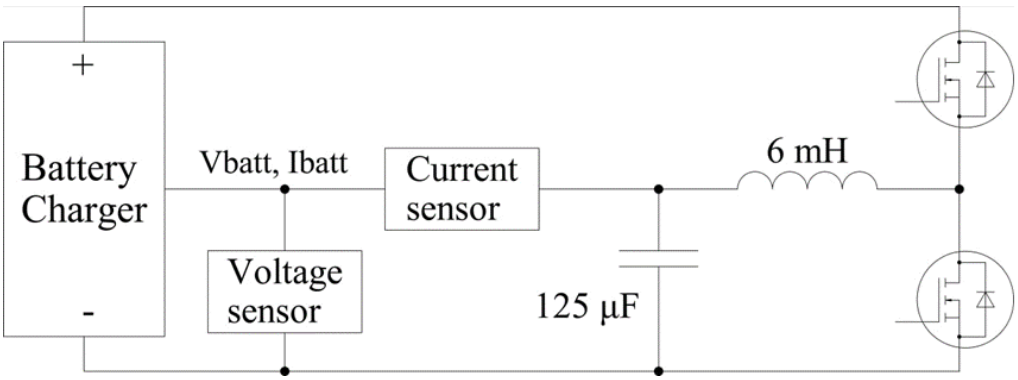

Figure 4.2: Battery emulator circuit connected to charging station terminals.

It is important to notice that the DC/DC charging converter and the emulator circuit share the same supply terminals, which implies that the absorbed energy by the emulator is returned to the common DC line. This significantly reduces the energy consumption of the test bench and assists in stabilizing the experiment. Moreover, it eliminated the need for power inverters utilized to dispose of the extracted energy, like the ones used by other converter-based battery emulators. The interaction between the DUT and the emulator circuits is represented in the following equations:

$$V_{battery} = V_{charger} - V_{emulator} \tag{4.1.1}$$

$$I_{battery} = -I_{charger} \tag{4.1.2}$$

By regulating the emulator voltage $V_{emulator}$, the imitated battery voltage is developed accordingly. The previous equations also indicated that the battery and charger currents are identical but with different signs. It is crucial to maintain energy balance by operating both circuits close to each other. This prevents the accumulation of energy inside the inductors, which can cause burnout.
Filter parameters of both circuits were designed based on the following equations:

$$L = \frac{V_{out}\left(V_{in} - V_{out}\right)}{I_{ripple} f_{sw} V_{in}} \tag{4.1.3}$$

$$C = \frac{I_{ripple}}{8 f_{sw} V_{ripple}} \tag{4.1.4}$$

where f_{sw} is the transistor switching frequency, I_{ripple} and V_{ripple} are the allowable output voltage and current ripples, respectively.

4.2 Simulation Based Test-bench

The proposed test bench was simulated in MATLAB/Simulink environment using the power system library. The DC/DC part of the charging station is controlled by dual loop regulators. Figure 4.3 exhibits the DC charger control system, where the outer loop regulator receives voltage sensor measurement and compares it to the desired value provided by the battery manager. Then, a PI controller was used to regulate the produced error. The reference signal of the inner current regulator is formulated by the previous voltage control stage and compared to the actual current obtained from sensor measurements. Another PI controller was employed to regulate the current error signal and generate the charger control action. Saturation functions limiting regulator responses are represented in the figure. The current limitations I_{max} and I_{min} are set according to the actual physical limitation of the modeled converter. The $controller_{max}$ and $controller_{min}$ saturation is set between (0-0.95), which symbolizes the duty cycle ratio with 0 being a fully closed transistor.

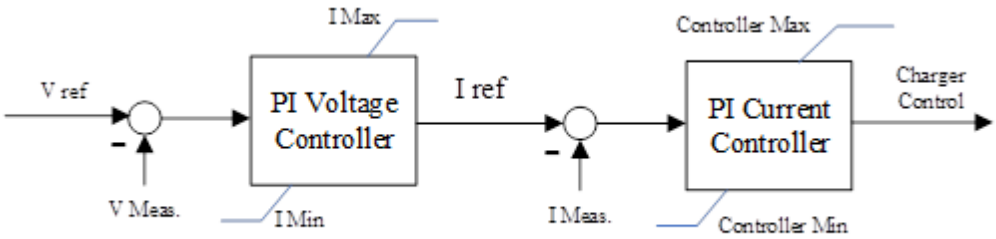

Figure 4.3: DC charger regulators.

Similarly, the emulator voltage and current are regulated using a specialized control structure. In figure 4.4, the battery model receives the current measurement and

generates the emulated voltage, which is considered the voltage reference signal. A PI controller was deployed to ensure that the battery emulator followed the reference battery voltage, while a proportional P current controller was used to generate the final control action of the emulator. The saturation functions of the utilized regulators are correlated with the previous charging controller to achieve mutual correspondence. In this case, the current saturation plays an important role in restricting the exchanged current between the common DC line and the emulator converter, which protects the DUT from high circulating currents. The emulator response is calibrated by tuning the dual-loop regulator parameters.

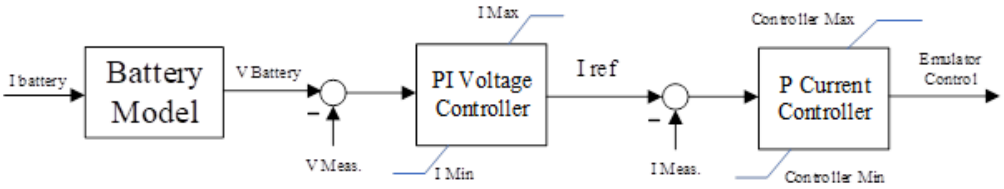

Figure 4.4: Battery emulator control loops.

The battery model parameters are exhibited in table 4.1, along with the charging station power rating. Model parameters were extracted from the generic battery model block in MATLAB by setting the nominal voltage and capacity. The discharge curve simulation revealed the corresponding parameters that significantly change when varying battery ratings due to high nonlinearity. Low power configuration was selected as a benchmark test to facilitate the comparison with practical results. Nevertheless, higher power rating results will be provided later in the experimental part of this chapter.

Table 4.1 — Emulator system parameters

Module	**Parameter**	**Value**	**Units**
Charger	Total Power	15.375	*W*
	Output current	3.75	*A*
	Nominal voltage	4	V
Battery Model	E_0	4.1748	V
	K	0.0057	V/Ah
	Q	5.06	Ah
	A	0.32331	V
	B	12.067	Ah^{-1}
	time constant	1	*sec.*
	Initial SoC	60	%
	R_{int}	0.007608	Ω

Figure 4.5 shows the emulated battery's SoC growing at a constant rate, which

indicates normal charging operation. The battery emulated and modeled voltages are corresponding to each other, especially at steady-state. This implies the successful operation of emulator control loops. The fast dynamics experienced by the battery emulator voltage response represent the utilized converter transient stage. This is a conventional behavior in emulator devices caused by electronic components attempting to imitate the required dynamics. Battery current was maintained at (3.75 A), while the negative sign represents the current direction from charger to battery emulator. As previously illustrated, the control signals of both converters were kept as close as possible to induce energy balance and prevent inductor burnouts.

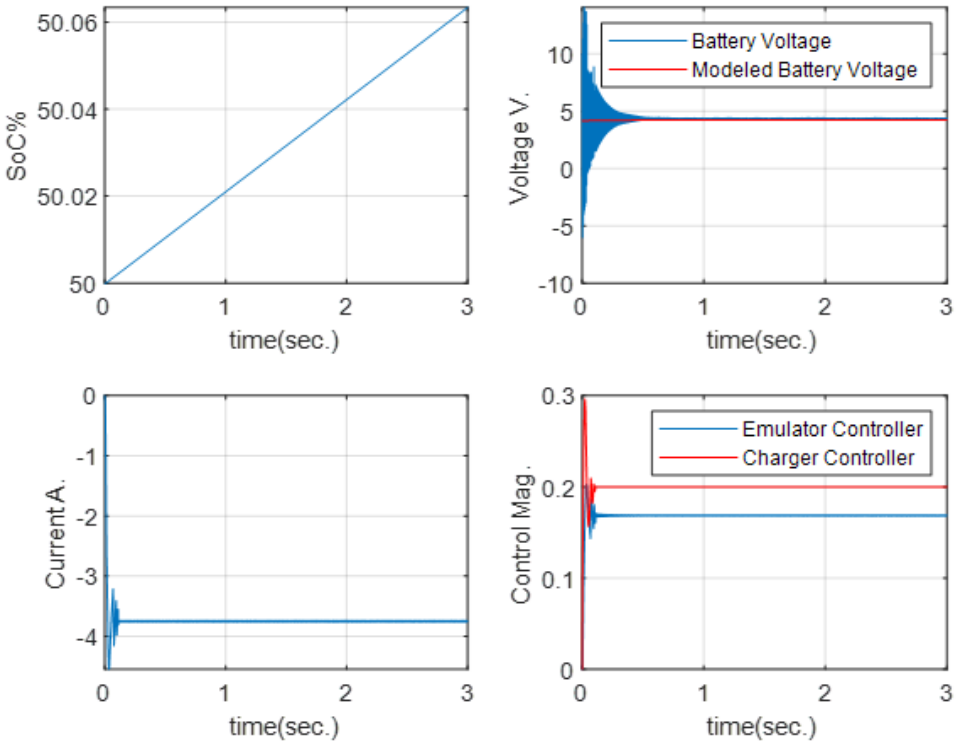

Figure 4.5: Simulation of battery emulator.

4.3 Experimental Study

For validation purposes, the proposed test bench was implemented practically. The simulated design in the previous section was replicated using power electronic devices and microcontroller boards. The battery model was developed in the LABVIEW environment using G-language, allowing real-time-based implementation. The model was discretized, and local functions were incorporated to resemble their MATLAB-based counterparts. It should be mentioned that the developed model includes functions that have not been expressed in Li-ion battery dynamic equations (1.6.1-1.6.4). These functions are related to parameter initialization, value limitation, and operational requirements. They were deduced by performing an inspection and decomposition of

MATLAB's generic battery block. The real-time LABVIEW-based model, illustrated in Appendix E, acquired a program registration status as an original implantation of such models in the G-language environment.

4.3.1 Experimental Setup and Utilized Devices

Figure 4.6 displays the proposed test bench construction with labels indicating different components. The DC charging regulators and the battery emulator control loops were also transferred into the LABVIEW real-time environment. The communication between software and hardware modules was established using a dedicated data acquisition NI-DAQ PXI-6025e card. This interface device has an impressive 200 kS/s analog input interpretation rate, which enables the real-time program to process multiple channels simultaneously. It provides discrete values of the current and voltage measurements obtained from sensory units. These measured values are scaled and handed to the emulator and charger controllers along with the battery model. After control action calculations are performed, the control signals are transmitted back through the DAQ device to the microcontroller units. These signals are scaled down to the range of (0-3.3V), which accommodates the Amigo Heart controller analogy input capabilities. This controller board was locally designed based on the STM-microcontroller technology, and it is utilized for PWM signal generation. Each microcontroller generated two identical PWM signals with opposing polarities to operate the power converter transistors. The output of each converter contributes to the voltage drop and current flow in the filter circuits separating the DUT unit and the battery emulator. These filters and converters operate contrary to each other, achieving the required V-I characteristic, which emulates battery system behavior.

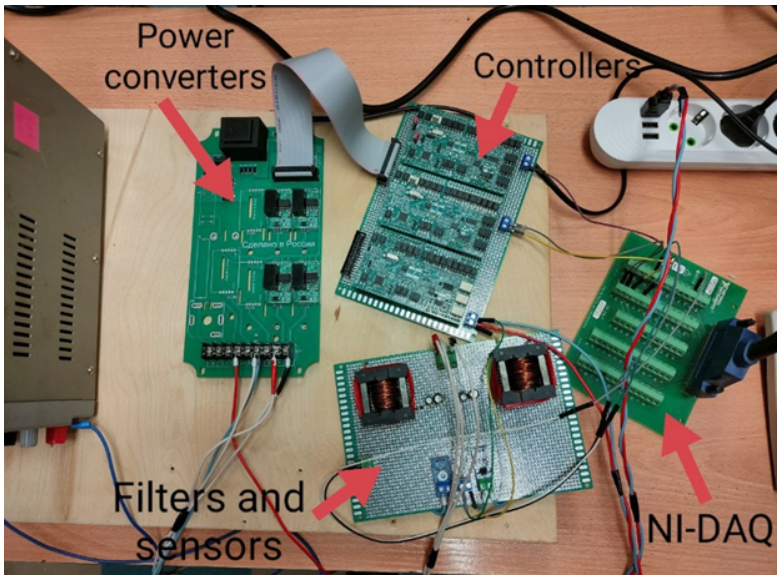

Figure 4.6: Experimental setup of the proposed test-bench.

Sensors scaling and calibration were executed on the computer for convenience

using the LABVIEW program front panel, exhibited in figure 4.7. Furthermore, the designed panel offered a flexible and quick approach for model re-characterization by online variation of battery parameters. This is extremely useful during the charger validation process to examine interaction with various battery ratings. Therefore, it is more suitable for experimentation than other commercially available battery emulators.

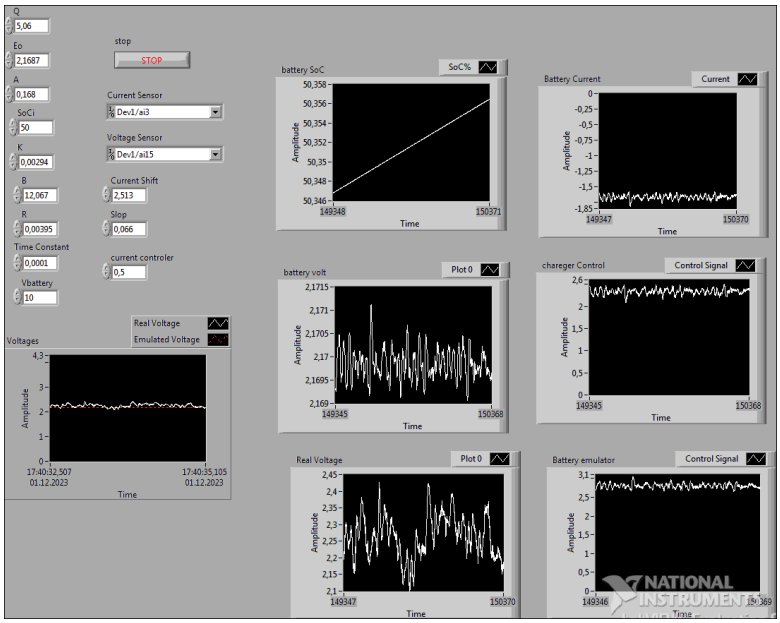

Figure 4.7: Front panel of the LABVIEW control and monitoring center.

Finally, the designed experimental setup adhered to international standards for energy storage systems with electrical installation parameters and test methods IEC 62933-2-1:2017 and IEC 62933-1:2018. Under nominal voltage and current, the tested system capacity obeyed the systematic performance testing procedures described in the standards. Nevertheless, the round-trip and charge-discharge effectiveness were not carried out, since they lay outside the addressed scope of this research.

4.3.2 Experimental Results and Discussion

Battery parameters demonstrated in table 4.1 were deployed using the front panel to emulate the addressed battery behavior. For safety reasons, a specific operational sequence was followed:

1. The rectifier supply is tuned on the DC voltage is stabilized before operation.
2. The power supply of microcontroller units and sensors is turned on.
3. The computer-based model and controllers are executed, making sure sensor's calibration is correct.
4. The DC charger and the battery emulator are switched on, and battery emulation processes begins.

Figure 4.8 shows the current and voltage responses of the test bench obtained di-

rectly from the real-time system operation. The emulated battery voltage was generated by the real-time model, while the real voltage was acquired by the voltage sensor representing the battery emulation process. The small fluctuations in the real signal around the modeled one are related to the accuracy of the utilized sensor and unshielded wiring noise. It is also influenced by the microcontroller precision, which is correlated with the (10kHz) switching frequency. Nonetheless, the emulator successfully achieved the required characteristic with sufficient accuracy. The battery current is around (3.5 A), which is slightly less than the maximum permissible charging current in table 4.1.

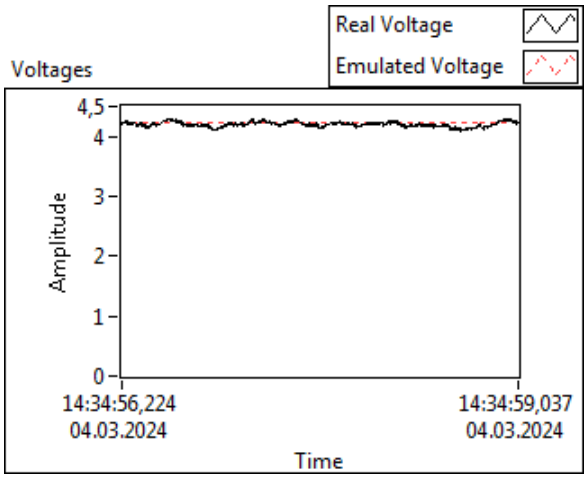

Emulated and real battery voltage

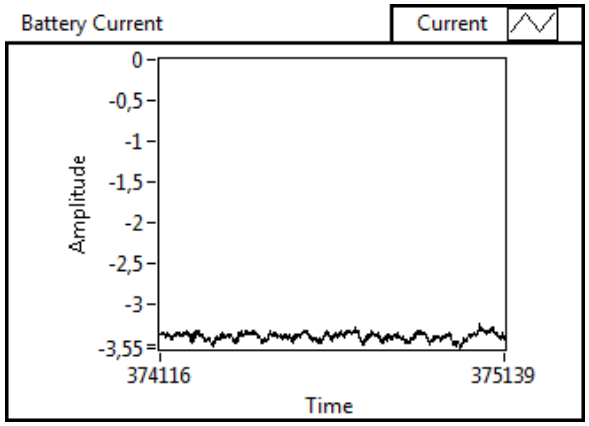

Battery current

Figure 4.8: Test bench voltage and current responses.

The control signals generated by the battery emulator control loops in figure 4.4 and the charger regulator in figure 4.3 are exhibited in figure 4.9. Both signals were observed close to each other, which indicates the previously stated energy accumulation prevention condition was accomplished.

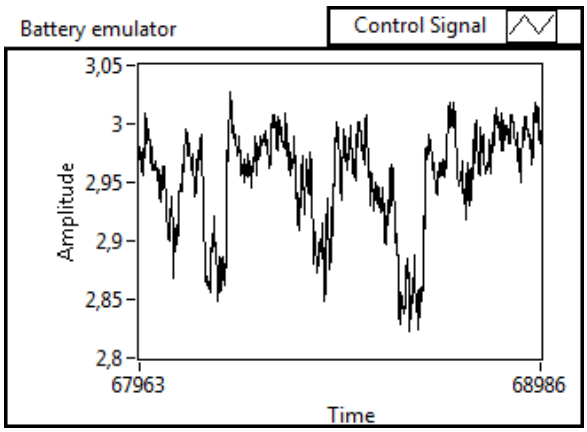

Battery emulator

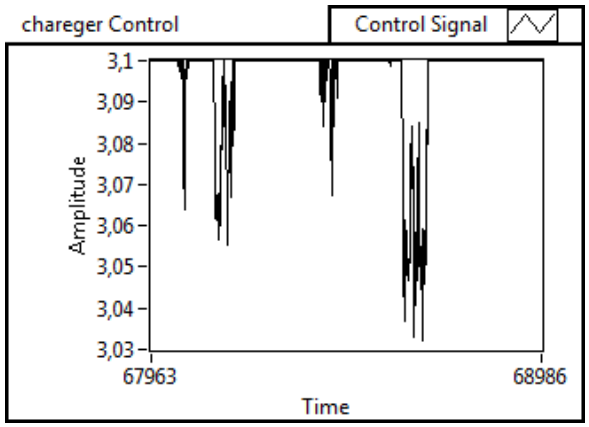

Battery charger

Figure 4.9: Emulator and charger control signals.

Figure 4.10 shows the battery's SoC emulation. This signal is purely emulated for virtualization purposes, as there is no actual battery being charged. The increased

charging rate implies the normal commencement of the charging procedure.

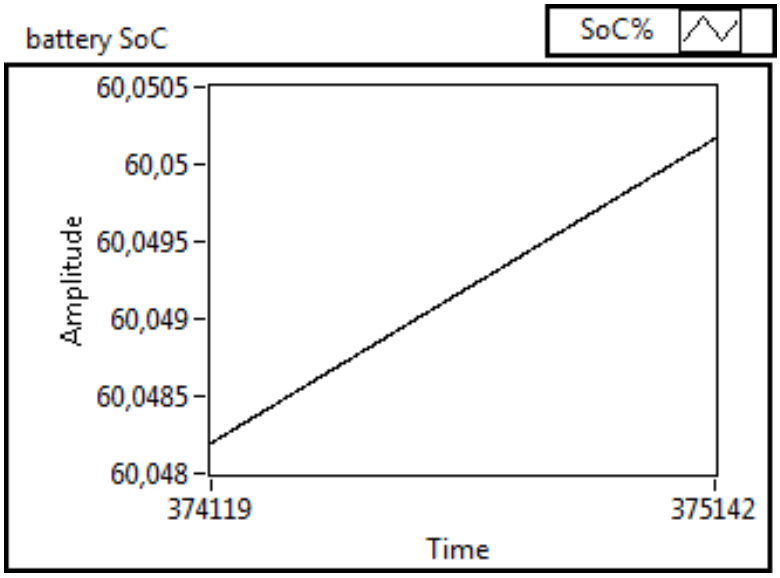

Figure 4.10: Emulated battery's state of charge.

For demonstrating the proposed test-bench full capability, the battery parameters were re-modeled to operate on a much higher power rating. The new parameters of battery emulator and charger systems are illustrated in table 4.2. Although the current was significantly increased, the new rated current is still well within the operational range of the (IRF1018E) MOSFET transistor which requires no heat sink for short periods of operation.

Table 4.2 — Emulator system parameters - High power

Module	Parameter	Value	Units
Charger	Total Power	> 216	W
	Output current	18	A
	Nominal voltage	12.8	V
Battery Model	E_0	11.9279	V
	K	0.00824	V/Ah
	Q	10	Ah
	A	0.92374	V
	B	6.1062	Ah^{-1}
	time constant	1	$sec.$
	Initial SoC	60	%
	R_{int}	0.011	Ω

The responses of the high-power test bench are shown in figure 4.11. It can be noticed that the current and voltage responses became less noisy than the previously

obtained results. This is mostly due to the better performance experienced by voltage and current sensors with higher sensing range. The high-value signals also played an attenuating factor in induced wiring noises. The figure illustrates the success of the emulation process.

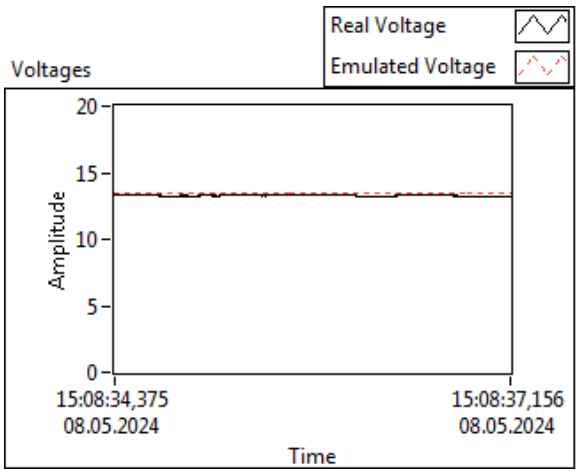

Emulated and real battery voltage

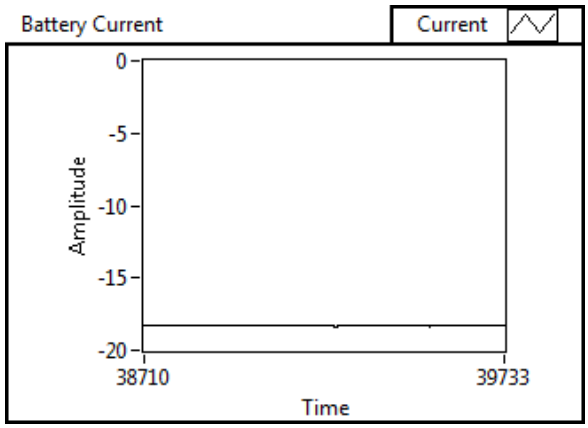

Battery current

Figure 4.11: Higher power test bench responses.

4.3.3 Validation of Results

Substantiating the proposed test-bench fidelity requires comparing the attained emulated battery characteristic against the real one. For this reason, a KEDANONE (NCR-18650) Li-ion battery was exploited to obtain the charging curve characteristic. The battery parameters that need to be re-calculated according to the new physical requirements are illustrated in table 4.3. It must be pointed out that MATLAB implements a unique method to predict these parameters. This method is inspired by [93; 94], but it might lack accuracy with real batteries depending on the internal organization of battery cells and manufacturing materials. However, the accuracy of these methods is not addressed in this research. A multi-chemistry Baiway battery capacity indicator was used to acquire the SoC measurements at specific instances while charging the real battery module. This indicator also has limited accuracy depending on internal interpretations of voltage-capacity relations. The experiment was repeated with the same parameters on the proposed test bench, and the two discharge curves were compared. Figure 4.12 demonstrates the real and emulated battery data. Both curves have the typical zones of battery discharge characteristics, including exponential, nominal, and voltage collapse regions. This indicates that the obtained results concur with the expected standard behavior. Furthermore, the results verify the proposed test-bench accuracy in imitating the characteristics of the battery system. The two curves are clearly correlated with fluctuating errors between them related to the previously mentioned practical limitations.

Table 4.3 — Real battery parameters

Module	Parameter	Value	Units
Charger	Total Power	> 36	W
	Output current	3	A
	Nominal voltage	12.8	V
Battery Model	E_0	12.272	V
	K	0.0039194	V/Ah
	Q	100	Ah
	A	0.70299	V
	B	0.1363	Ah^{-1}
	time constant	1	$sec.$
	R_{int}	0.035	Ω

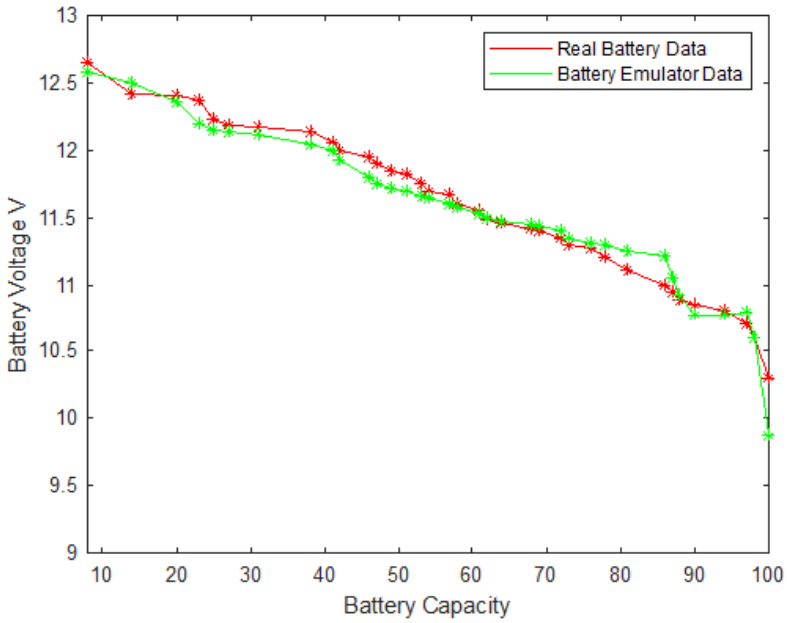

Figure 4.12: Real and emulated battery discharge characteristics.

4.3.4 Test-bench Limitations

The rising question of test bench feasibility in commercial applications prompted modifications to the original system design. For the test bench to be commercially deployable, the computer unit and related specialized interface card are required to be substituted by a compact device, which requires less energy and space. Owing to the relatively slow battery dynamics, the STM microcontroller became a valuable candidate for such replacement. The battery model was translated into C-code with proper adjustment related to specialized functions substitution. Due to the code originality and asso-

ciated advantages, this code received a program registration status and is exhibited in Appendix F. Again, the Amigo Heart controller was utilized by deploying the developed battery model code on its microcontroller. Initially, a HiL test was conducted to evaluate the microcontroller-based model's effectiveness. The UART technology was used to establish communication between the microcontroller board and the LABVIEW-based interactive test program. The real-time program tested the transmitted data package's accuracy and speed, while the model validity was examined using current-SoC analysis. The front panel of the test LABVIEW program is demonstrated in figure 4.13, where adjustable battery current values were set and transferred to the microcontroller unit. The developed model receives these values periodically and determines the Soc and battery voltage according to the provided dynamics. Then, it sends these values back to the LABVIEW program for displaying them.

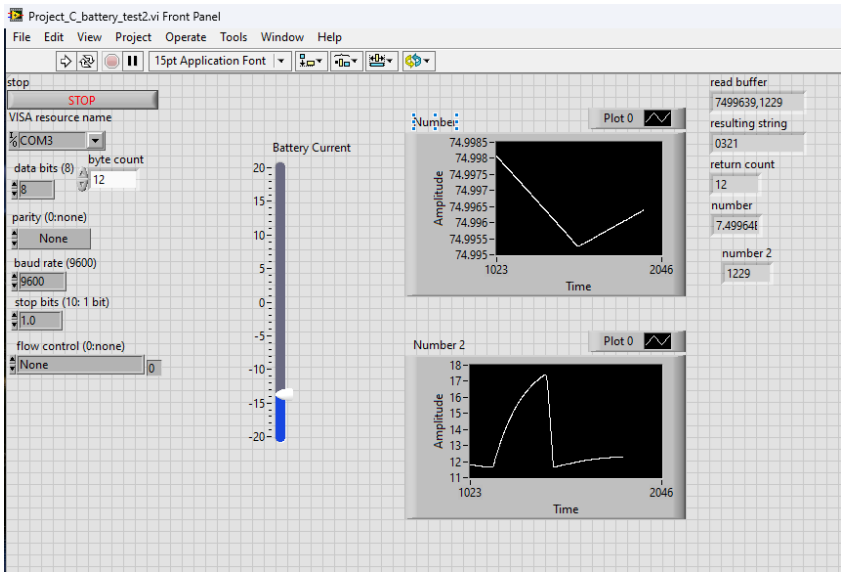

Figure 4.13: Front panel of HiL based Test.

The utilization of the Amigo Heart controller enabled more flexibility and efficiency by eliminating the need for expensive system components and software. This solution also overcomes limitations related to the license of these programs allowing open source development of such test-bench.

4.4 Conclusion of chapter four

Validating the newly designed battery technologies requires a safe and modifiable test bench. A real-time battery emulator was developed based on the Li-ion battery's electrochemical model. It utilized the PHiL technology principles, where actual power signals were exchanged and tested. The emulator imitated the V-I characteristic of the battery system when integrated into a charging device. Simulation and practical studies were conducted to assess the proposed design performance. Two versions of

the test bench were presented based on the employed technology for model deployment. The LABVIEW version utilized specialized interface cards and G-language-based battery models and controllers to achieve the required results. Whereas, the STM-microcontroller version was considered more compact and eliminated the need for specialized hardware and software. Both versions received program registration statutes for their originality. The obtained test-bench characteristic was compared to an actual battery discharge curve, and the results validated the battery emulation performance.

Chapter 5

Power Supply System of Automated Stacker Crane

Battery-supported power supply systems can integrate various locally distributed generators, including renewable energy sources. It can reliably sustain the operation of industrial applications during peak demand hours and malfunction periods. When implemented to hoist and transport mechanisms, it can recover the regenerated energy during reverse drive modes, which is usually dissipated using dump loads. Automated stacker crane ASC system has been studied as an example of these mechanisms, because of the prominent advantages and the lack of research for this application. Increasing the sustainability of warehouses can introduce economic, environmental, and social benefits to the logistics sector [130]. The simultaneousness of material maneuvering operations in a warehouse can lead to demand spikes, which prompts an increased electricity price and large installations of power components. The battery-operated power supply can mitigate this issue by enabling the power autonomy of electrical complexes. The battery system functions as an energy buffer between generators and loads, charging during excess generation periods and discharging when the complex is disconnected from the grid. These operations are affiliated with the Microgrid energy management principles established in Chapter (2). The developed algorithms are incorporated into the ASC system design, especially when considered as an active load connected within a power complex. The utilized battery is charged using the developed wide-range resonant charger topology in Chapter (3). This chapter aims to establish an application-based study of the proposed battery-integrated power supply. The previously designed technological collection is employed to achieve reliability and efficiency. Different operational scenarios are investigated, including renewable power utilization and Microgrid interactions. Regardless of power supply modifications, the crane complex must maintain operational performance without reconfiguration or parameter manipulation.

5.1 Crane System Configuration

The addressed stacker crane system configuration is roughly similar to the one presented in figure 1.2. The application is inspired by an actual ASC presently being

developed by the (РУХЛІО) company for warehouse material handling. The crane structure, demonstrated in figure 5.1, consists of three maneuvering mechanisms operated by single or multiple electrical drives. The horizontal movement is executed using a guided shuttle traveling on ground rails along the warehouse aisles. The lifting mechanism is accomplished by the two hoist columns, while forks are used for cargo delivery. In this research, the designed crane mechanism was adopted without changes, since the research targets the modification of the crane's power supply system rather than the mechanism itself.

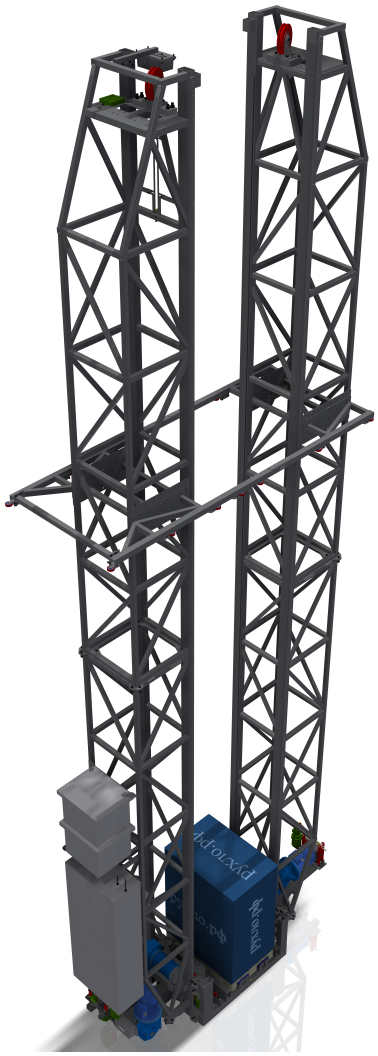

Figure 5.1: Structure of ASC developed by (РУХЛІО) company.

The classical electrical complex architecture was induced by the actual implementation of the ASC system demonstrated in figure 5.2. Four back-to-back converters, comprising uncontrolled rectifiers and regulated inverters, are connected to the main electricity grid. These converters operate four induction motors moving the mechanical parts of the crane. Horizontal and fork mechanisms employ a single-drive system, while the hoist mechanism is operated by a double-drive system. Braking resistors and associated control systems are installed on each drive to dissipate the regenerated energy, significantly reducing the efficiency.

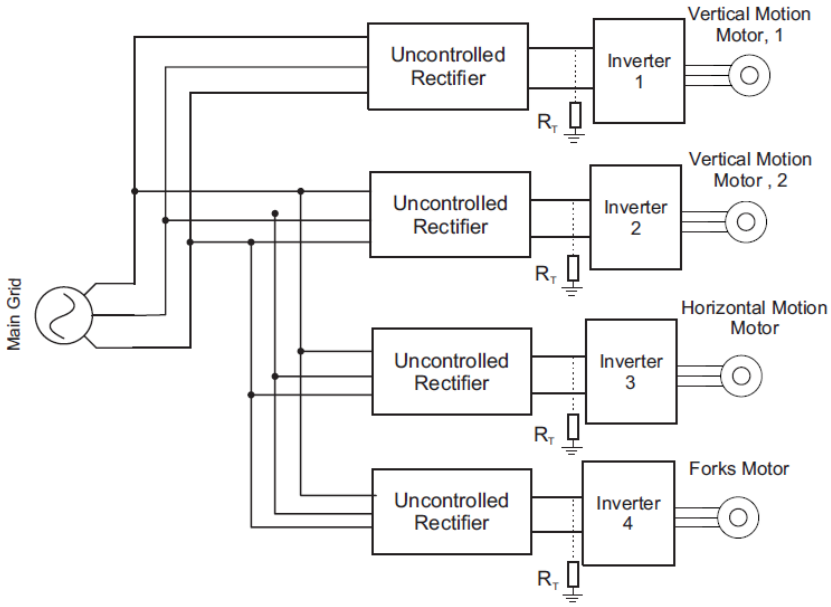

Figure 5.2: Classical ASC drive systems.

5.1.1 Drive System Model

Generally, four squirrel-cage asynchronous motors were used to perform the displacement maneuvers of the crane system. These motors have the same dynamic model but differ in their parameters and power rating. For control purposes, a model of the asynchronous machine has to be developed based on the rotor flux frame, where the reference axis is assumed to be rotating at the synchronous speed[131]. Then, the representation of stator and rotor voltages with constant flux in the xy-frame can be written as [131; 132]:

$$V_{xs} = R_s i_{xs} + \rho \Psi_{xs} - \omega_e \Psi_{ys} \tag{5.1.1}$$

$$V_{ys} = R_s i_{ys} + \rho \Psi_{ys} + \omega_e \Psi_{xs} \tag{5.1.2}$$

$$R_r i_{xr} + \rho \Psi_{xr} - (\omega_e - \omega_r) \Psi_{yr} = 0 \tag{5.1.3}$$

$$R_r i_{yr} + \rho \Psi_{yr} + (\omega_e - \omega_r) \Psi_{xr} = 0 \tag{5.1.4}$$

where R_s and R_r are the stator and rotor phase wounding resistors, Ψ_{xs} and Ψ_{ys} are the stator flux in the xy-frame, while Ψ_{xr} and Ψ_{yr} are the rotor flux in the same working frame. ω_e and ω_r represent the electrical and rotor speed respectively, while ρ symbolizes the number of poles. Now, take into consideration that the machine inductance can be formulated as:

$$L_s = L_{sl} + L_m \tag{5.1.5}$$

$$L_r = L_{rl} + L_m \tag{5.1.6}$$

where L_s, L_r, and L_m are the stator, rotor, and magnetization inductance respectively. The stator and rotor fluxes in the xy-frame can be written as:

$$\Psi_{xs} = L_s i_{xs} + L_m i_{xr} \tag{5.1.7}$$

$$\Psi_{ys} = L_s i_{ys} + L_m i_{yr} \tag{5.1.8}$$

$$\Psi_{xr} = L_r i_{xr} + L_m i_{xs} \tag{5.1.9}$$

$$\Psi_{yr} = L_r i_{yr} + L_m i_{ys} \tag{5.1.10}$$

Then by substituting $i_{xr} = 0$ and $\Psi_{yr} = 0$ we get:

$$i_{yr} = \frac{-i_{xs} L_m}{L_r} \tag{5.1.11}$$

$$\Psi_{xr} = L_m i_{xs} \tag{5.1.12}$$

$$\Psi_{xs} = L_s i_{xs} \tag{5.1.13}$$

$$\Psi_{ys} = L_s \left(1 - \frac{L_m^2}{L_s L_r}\right) i_{ys} = \sigma L_s i_{ys} \tag{5.1.14}$$

where $\sigma = \left(1 - \frac{L_m^2}{L_s L_r}\right)$. Finally, the complete representation of the asynchronous machine in the xy-frame is reduced into the two following equations:

$$V_{xs} = R_s i_{xs} + \rho L_s i_{xs} - \sigma \omega_e L_s i_{ys} = R_s i_{xs} + \rho L_s i_{xs} + e_{xs} \tag{5.1.15}$$

$$V_{ys} = R_s i_{ys} + \rho \sigma L_s i_{ys} + \omega_e L_s i_{xs} = R_s i_{ys} + \rho \sigma L_s i_{ys} + e_{ys} \tag{5.1.16}$$

The stator voltages can also be reformulated to include the dynamics changes in flux and current [133]:

$$V_{xs} = R_s i_{xs} + \rho \sigma L_s \frac{d i_{xs}}{dt} + \frac{L_m}{L_r} \frac{d \Psi_{xr}}{dt} - \sigma \omega_e L_s i_{ys} \tag{5.1.17}$$

$$V_{ys} = R_s i_{ys} + \rho \sigma L_s \frac{d i_{ys}}{dt} + \frac{L_m}{L_r} \omega_e \Psi_{xr} - \sigma \omega_e L_s i_{xs} \tag{5.1.18}$$

Equations 5.1.17 and 5.1.18 were developed based on the following flux linkage characterizations:

$$\Psi_{xs} = \frac{L_m}{L_r} \Psi_{xr} + \sigma \omega_e L_s i_{xs} \tag{5.1.19}$$

$$\Psi_{ys} = \sigma L_s i_{ys} \tag{5.1.20}$$

$$\tau_r \frac{d \Psi_{xr}}{dt} + \Psi_{xr} = L_m i_{xs} \tag{5.1.21}$$

where $\tau_r = \frac{L_r}{R_r}$; However, if we keep the rotor flux constant and align the x-axis of the current with rotor frame, the previous steady state equations in (5.1.15-5.1.16) are implied and utilized. The machine torque can be expressed as:

$$T_e = \frac{3}{2} \rho \frac{L_m}{L_r} \Psi_{xr} i_{ys} \tag{5.1.22}$$

While the mechanically rotating mass dynamic based on applied load torque T_L and developed torque T_e can be formulated as:

$$T_e - T_L = J_\Sigma \frac{d \omega_m}{dt} + B \omega_m \tag{5.1.23}$$

where J_Σ is the mechanism moment of inertia. Moreover, the slip speed is given by:

$$\omega_r^{slip} = \frac{L_m i_{ys}^{ref}}{\tau_r \Psi_{xr}} \tag{5.1.24}$$

The angular frequency corresponding to the stator voltages frequency and the orientation angle of the *xy* coordinate system are equal to:

$$\omega_e = \omega_r + \omega_r^{slip} \tag{5.1.25}$$

$$\omega_t = \int \omega_e dt \tag{5.1.26}$$

The employed motors parameters are demonstrated in table 5.1. They have been acquired from the actual drive system of the (РУХЛО) stacker crane application. The squirrel-cage motors specifications were projected into the standard data sheets to estimate the parameters. Motors power ratings, operating voltage, rated currents, and mechanical inertia were imposed by the original design of the company which has been accepted without changes. The flexibility of this work enables the incorporation of all previously developed technologies in the drive system power supply without modifying the internal mechanism of the addressed complex. The crane system, developed in MATLAB/Simulink environment, implemented the demonstrated parameters to simulate the actual performance of the addressed complex. Only one vertical motor is displayed in the table since identical parameters are expected for the double-drive hoist mechanism.

Table 5.1 — ASC motors parameters

Parameters	**Vertical Motor**	**Horizontal Motor**	**Forks Motor**
$Power(kW)$	11	7.5	2.2
$Poles$	2	4	4
$J_\Sigma(Kgm^2)$	0.0482	0.0563	0.009
Nominal Torque $(N.m)$	35.6	49.1	14.7
$R_s(\Omega)$	0.9333	1.322	1.7592
$R_r(\Omega)$	0.393	0.8769	1.7222
$X_s(\Omega)$	1.8031	2.9124	3.8341
$\acute{X}_r(\Omega)$	2.4278	3.4945	5.1882
$X_m(\Omega)$	68.072	90.9684	88.0186

5.1.2 Actual ASC System Performance

As previously illustrated, the study of the ASC system is motivated by an actual device designed by (РУХЛО) company for warehouse applications. Many other companies like HUBMASTER, Jungheinrich, and E80 group produce similar cranes

but with different configurations and specifications. Generally, these ASC systems suffer from reduced performance due to the wasted energy during load-lowering mode. Depending on the power rating and elevation of the warehouse shelves, the vertical hoist mechanism can produce considerable energy during lad lowering, which can be retrieved and stored. The drive system, in this case, is regarded as a renewable source of free energy that can be reincorporated into the power supply of the complex. The existing designs utilize bulky braking resistors to dissipate the regenerated energy, which reduces the overall efficiency of the system. Moreover, their complexes lack the necessary techniques to deal with contingencies like power failure, the disconnection of supplied power through the ground rails because of mechanical wear, and increased power prices during peak hours. The utilization of energy storage devices and hybrid power supply can induce the required operational performance.

To emphasize the tackled issues and prospective advantages, real drive system data were collected from the (РУХЛО) crane device. Figure 5.3 shows the drive system power response when operated with no load and nominal load. It should be mentioned that, during the data collection procedure, the vertical motors operated at (40%) of nominal speed, the horizontal motor at (2%), and the fork motor at (30%) of nominal. A typical test was conducted by moving the mechanisms in different directions to monitor the effect. The regenerated power can clearly be observed as having a peak value of (4kW), which is considered a substantial value for the 5-meter height drop. The full height of (11 meters) was also avoided to prevent mechanism damage. This energy could have been recovered if an energy storage device was employed.

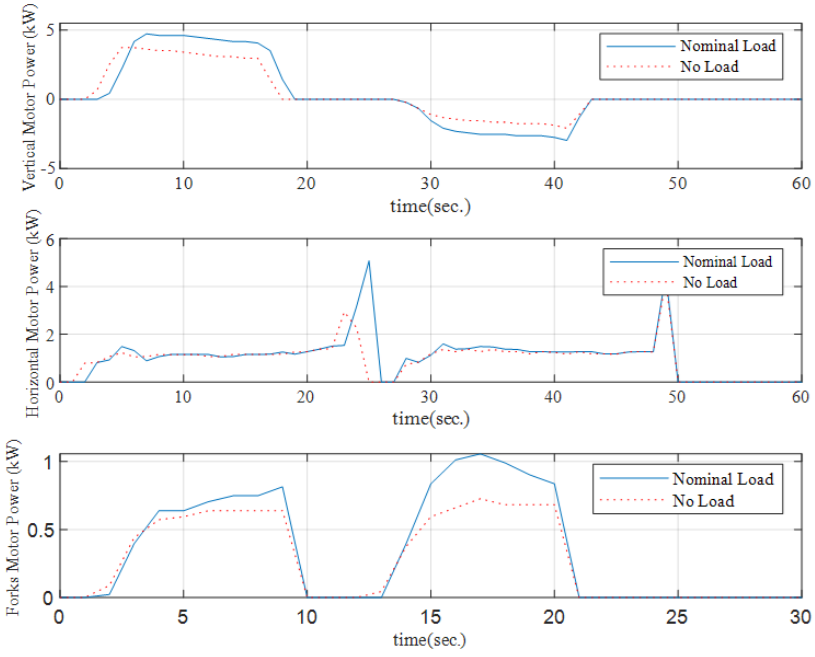

Figure 5.3: Crane drive systems power, with load and no-load operation.

Furthermore, the power supply system with the associated battery capacity is required to correspond with the maximum achievable power during motoring mode.

The vertical and horizontal mechanisms can concur, which means increased stress over power electronic devices during drive systems transient periods. This can be avoided by delaying the vertical motors for a specific period such that drive power peaks are misaligned.

Motor currents were also collected to establish the design requirements for the battery-supported power supply. Figure 5.4 exhibits the driven RMS current of the three-phase asynchronous motors. The misalignment of mechanism operations became more evident when considering the peak current of the four motors. Moreover, this response is essential in assessing the required system capacity and employed converter topologies.

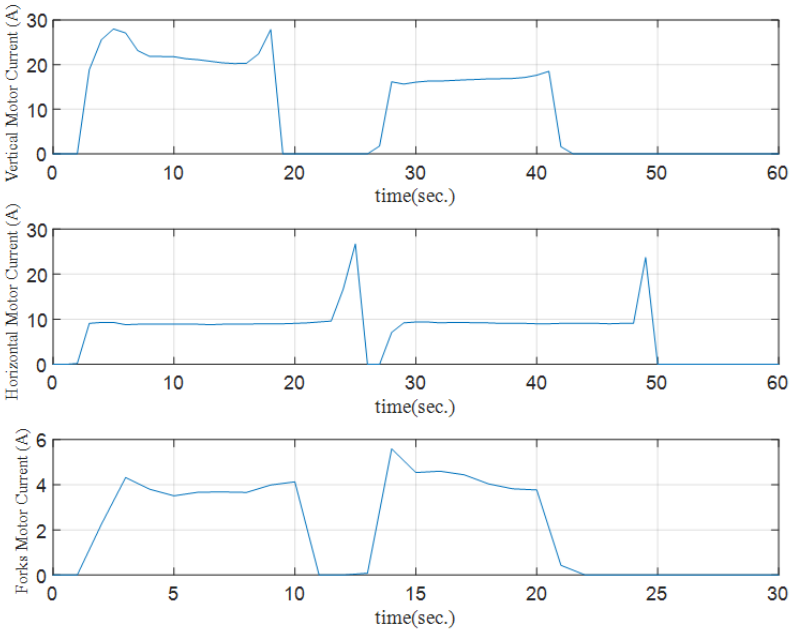

Figure 5.4: Crane drive systems currents.

Other obtained data form the actual crane system are found in Appendix G.

5.2 Battery Integrated Power Supply for ASC

Instigating efficiency and reliability into the stacker crane system requires employing battery battery-supported power supply. The initial proposed design includes an active rectifier, which supplies the energy essential to support the operation of electrical drive systems and charge the onboard battery. This design suggests the exploitation of the crane's ground rails to incorporate the common DC line supplying the complex. Furthermore, figure 5.5 shows the energy storage device configuration depicted by the battery system and capacitor bank. An isolated unidirectional DC/DC charger was used to charge the battery system from the grid during charging mode. The wide voltage range resonant converter developed in Chapter (3) was employed as the charging unit.

A circuit breaker configuration was utilized to switch the battery system from charging to motoring modes depending on operational conditions or when the grid-isolation command is provoked. During motoring mode, the battery system is directly connected to the inverter complex allowing bidirectional energy exchange. In this situation, the circuit breaker between the crane complex and the active rectifier is opened. The battery discharges the required operational energy to the four induction motors and recovers the regenerated energy during braking mode. This power supply configuration enabled the power autonomy of the crane complex, which increases system reliability during power faults, maintenance, and high demand periods.

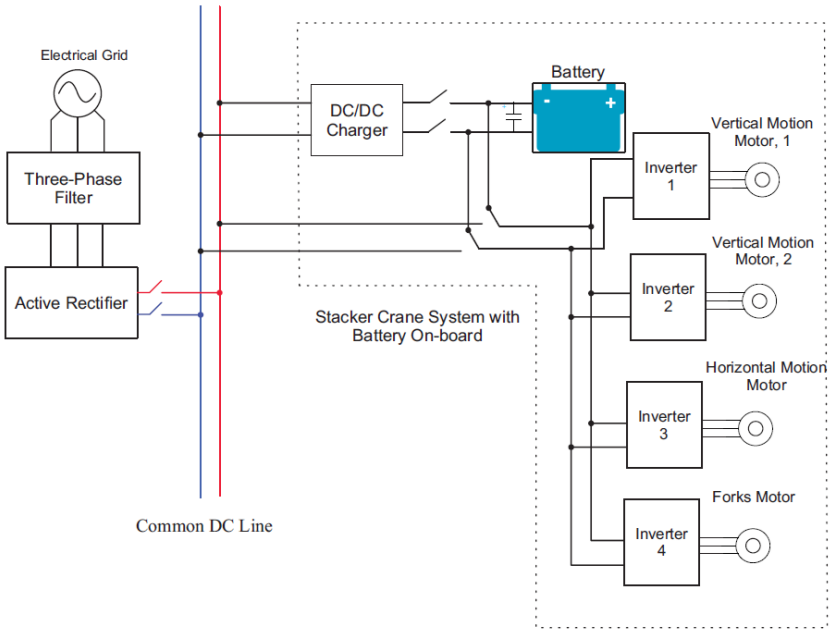

Figure 5.5: Proposed power supply of ASC system.

Finally, it should be mentioned that the employment of AFE topology was intended to permit recovered energy disposed into the electricity grid on the rare occasion of full energy storage capacity is encountered.

5.2.1 Energy Storage Devices

Energy storage devices are vital for the efficient operation of industrial complexes. Many examples of storage devices implemented into various crane systems were reviewed in Chapter (1). However, this research addresses the Li-ion battery system due to the foreshadowed benefits. The life span of these batteries depends on several factors, including the DC/DC charger topology, the depth of discharge, the operating temperature of the device, the SoC operational range, and many others. The complete-sizing problem of the battery system was analyzed and evaluated in [134]. For the addressed crane in that research, the battery system was assumed to have a capacity surpassing 25% of maximum power generation. However, in this research, the battery

system operates the crane with complete power autonomy. This implies that the sizing approach presented in [134] requires to be adapted such that the chosen battery system capacity achieves the required performance. The battery pack is needed to support the loading and unloading cycles for a specific period. The rated power demand of the crane system contributes significantly to the proper battery capacity selection. Moreover, factors like the nominal battery voltage and the typical operation cycles without charging also influence the selection procedure. Recharging the battery from the regenerated braking energy can reduce its size and increase the deployment time. Accounting for all these factors and the technical requirements established by the actual ASC system performance, a (75 kWh-600 V) battery is considered. Such batteries are commonly used in hybrid tracks and can support up to (400 km) of driving on one charge. For the considered crane application, the suggested battery capacity can operate the complex for (2000) full stacking cycles without recharge.

On the other hand, capacitors have higher power density than battery packs, which enables them to respond rapidly to changes on the demand side of the complex. The capacitor bank in figure 5.5 utilizes a parallel capacitor-battery configuration, stabilizing the voltage across battery terminals. Moreover, this configuration allows a faster dynamic reaction of the storage unit to sudden demand peaks in the drive systems. This property significantly reduced the capacitor bank size. In this case, the battery system reacts to extended demand periods, while the capacitor responds to demand fluctuations. Using this approach, additional power electronic devices and control systems for capacitors are deemed redundant. The exact size of the capacitor bank is calculated based on the maximum average current drawn by the drive complex [135].

$$I_{capacitor} = I_{Battery} - I_{avarage} \tag{5.2.1}$$

The average current of the drive complex can be calculated as:

$$I_{avarage} = \frac{\sqrt{3}}{2} \frac{V_{Line}}{V_{DC}} I_{peak} \cos\phi \tag{5.2.2}$$

where I_{peak} is the motor current amplitude, while $\cos\phi$ is the power factor. The average current represents the aggregated current of multiple motors working together in the worst-case scenario. By determining the maximum capacitor current, the minimum capacitance can be calculated based on the capacitor voltage-current relations. The utilized capacitor in this research has a capacity of (3.7 mF).

5.2.2 Vector Control

A three-phase controlled transistor bridge was used to realize the inverter circuit. Four inverters were employed in the stacker crane complex, with each inverter regulating the speed and currents of the associated asynchronous motor. The inverter permits the regenerated energy to flow back into the DC line during braking mode. This free

energy is retrieved by the battery system. The previously illustrated dynamics of the asynchronous motor are utilized to develop the inverter control system. A vector control mechanism was exploited to regulate the associated machine speed. A successfully executed motor controller guarantees the tracking of the desired speed profile and the accomplishment of ASC fundamental functions. Firstly, the reference motor current in the *xy*-frame was developed. The reference *x*-axis current was chosen to be a constant, which produced a fixed rated reference flux of the machine. Whereas, the reference *y*-axis current was generated by a speed controller. Figure 5.6 demonstrates the creation of vector control reference currents, where the slip speed was estimated by incorporating equation 5.1.24. Equations (5.1.25-5.1.26) were used to develop the angular frequency ω_t utilized in transformation between the (*abc*) and the (*xy*) frames.

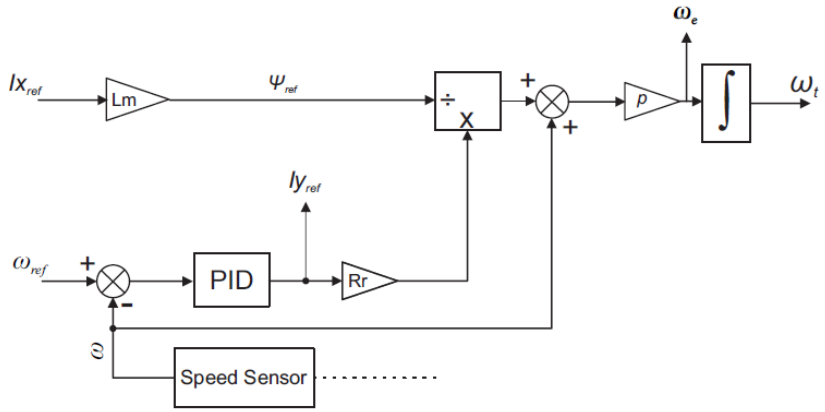

Figure 5.6: Reference signals generation and slip speed estimation.

The second stage of the vector control system is to regulate the internal currents. Motor phase-currents were transformed from the (*abc*) frame to the (*xy*) and compared to the reference signals developed in the previous stage. Equations 5.1.15 and 5.1.16 were employed to establish the control structure of the *x* and *y* channels exhibited in figure 5.7. Thereafter, the three-phase control signals are supplied to a PWM signal generator unit, which produces switching patterns of the inverter. It is important to notice that, although steady-state dynamic equations were employed in controller development, the MATLAB asynchronous machine block uses the variable flux equations (5.1.17-5.1.18). Nevertheless, with the assumed constant reference current on the *x*-axis, the flux stabilizes consequently, which justifies the aforementioned simplification.

5.2.3 Results and Discussion

The developed models and controllers are simulated in MATLAB/Simulink environment. Each asynchronous motor block was set with the parameters presented in table 5.1. Typical transistor-based inverters were utilized, while the AFE rectifier control system presented in figure 1.9 was exploited again. Controllers were designed and

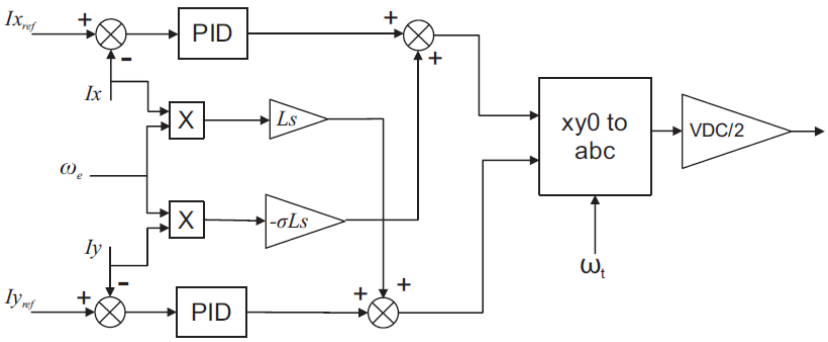

Figure 5.7: Control of the motor currents in the *xy*-frame.

tuned separately for each module and combined with the main Simulink model. In this section, three operational scenarios were tested and evaluated. The purpose of these scenarios is to simulate extreme cases to validate the performance of each component. In the first scenario, the ASC and the onboard battery system are supplied from the main grid through the active rectifier. As illustrated previously, the battery system and the capacitor bank are isolated from the crane's drive systems during such operation. The objective of this scenario is to test the active rectifier and the DC charger performance. Only vertical and horizontal motors were deployed in this scenario, while the load torque is assumed to be variable. Vertical motors were controlled to perform lifting and lowering operations that test the maximum demand and regenerated energy experienced by the stacker crane. Figure 5.8 exhibits the reference and actual speeds of the stacker crane on the vertical and horizontal axes. As seen in the figure, employing a vector control system accomplished perfect tracking results of the reference signals. For the vertical axis motors, the results of only one motor were demonstrated since they have identical responses.

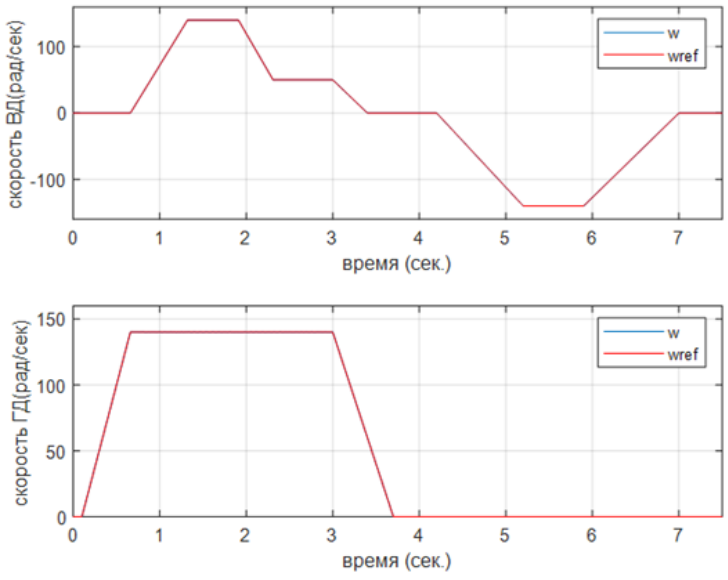

Figure 5.8: Reference and actual speeds of vertical and horizontal motors.

Figure 5.9 shows the actual and load torque of the two addressed motors. The differences between the two torque signals are due to the experienced machine speed changes. Actual torque tends to increase above the applied load torque when accelerating the machine, while a decrease in the torque was observed during deceleration.

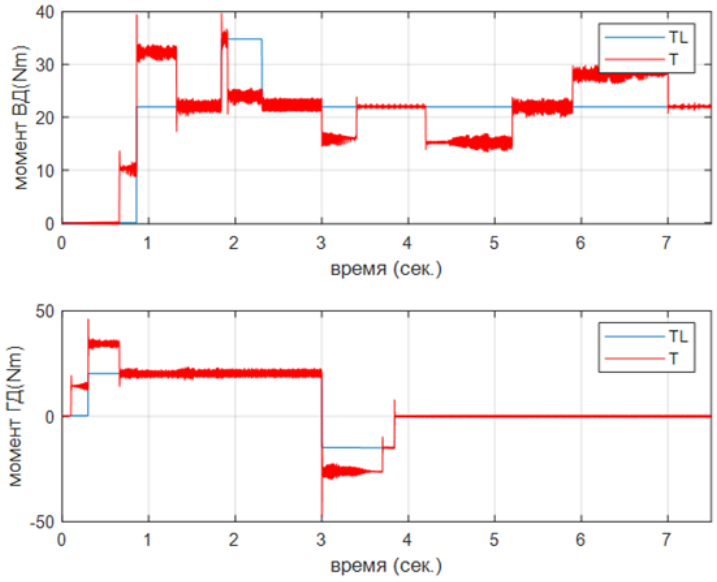

Figure 5.9: Load and actual torques of vertical and horizontal motors.

During this scenario, the battery system was constantly charged from the supply rectifier through the isolated DC/DC charger. The battery charging process is shown in figure 5.10, where the SoC maintained a constant rate.

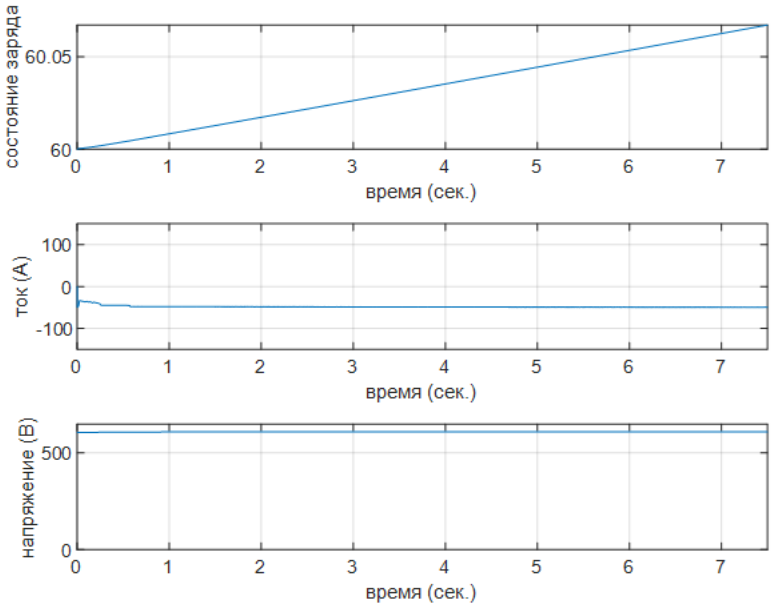

Figure 5.10: Battery response in first scenario.

The second scenario involves executing the same previous maneuver while dis-

connecting the crane from the main grid at (1.5 sec). Torque and speed maintained the same previous responses as in figures 5.9 and 5.10. Whereas, the battery response presented in figure 5.11 with a switching effect observed across all signals. The battery current instantaneously changed its sign to indicate the flip of power direction while maintaining the battery voltage. The battery SoC also decreased in the period between (1.5 sec.) and (4.5 sec.), which implies the discharge mode. However, an increase in the battery charge is experienced during the next period, which is associated with two vertical motor's load lowering. The regenerated energy was successfully recovered to charge the battery system. The power magnitude is significantly lower than the one in the previous mode of charging mode.

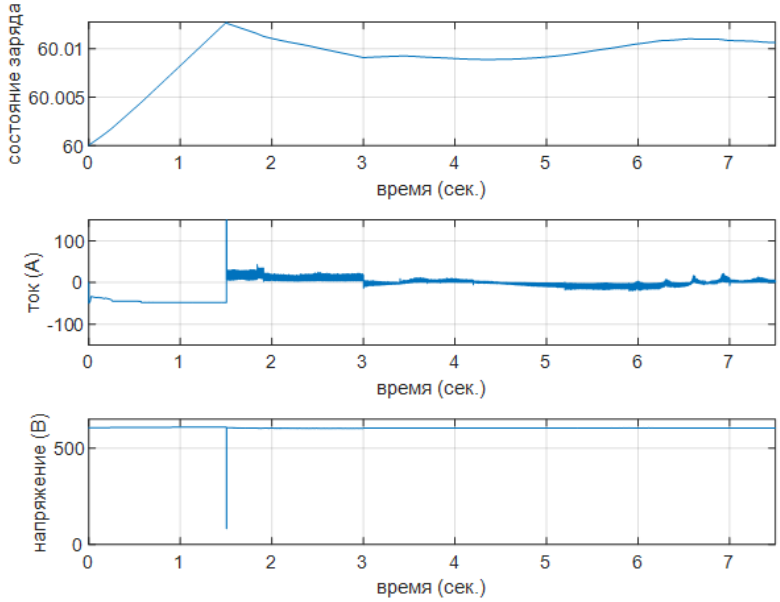

Figure 5.11: Battery response in second scenario.

The third scenario includes the full utilization of the entire drive system of the stacker crane to perform a load delivery maneuver. The vertical and horizontal motors were employed to move the crane shuttle and hoist to the required shelf rack. Then, the fork motor was activated to deliver the cargo to the desired location. Similar to the previous scenario, the automated power supply system switches from grid supply to battery-powered supply at (1.5 sec.). Figure 5.12 illustrates the speed responses of the crane motors. For cargo safety reasons, the vertical and horizontal motors have to be completely stopped before the fork motor initiation. The associated load and actual torque responses of each motor are shown in figure 5.13. The fork motor mechanism is loaded slightly after the motor starts accelerating to allow some time for core magnetization.

The battery system response is demonstrated in Figure 5.14. Unlike the previous scenario, the battery did not experience an obvious charging cycle due to the absence of load-lowering mode. However, a change in the descent rate of the battery's SoC was noticed. This is due to the braking and acceleration of motors accordingly.

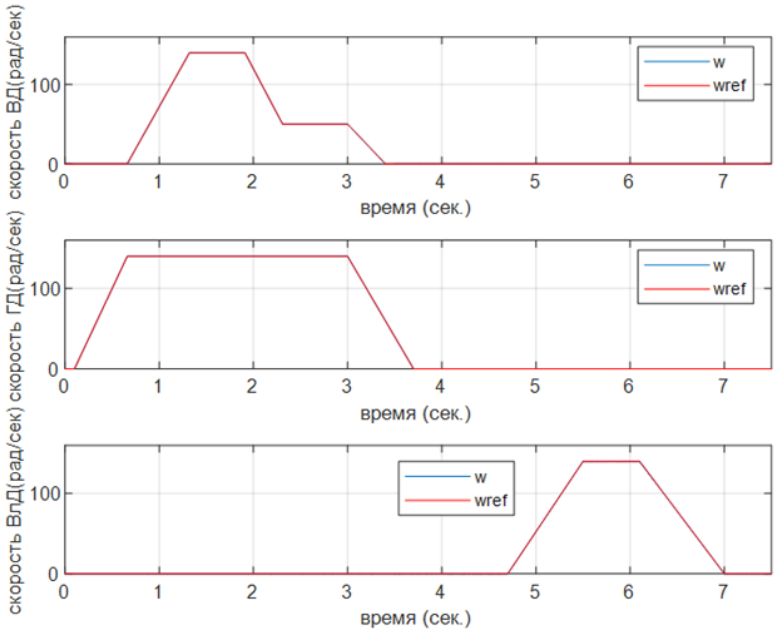

Figure 5.12: Reference and actual speeds of vertical, horizontal, and forks motors.

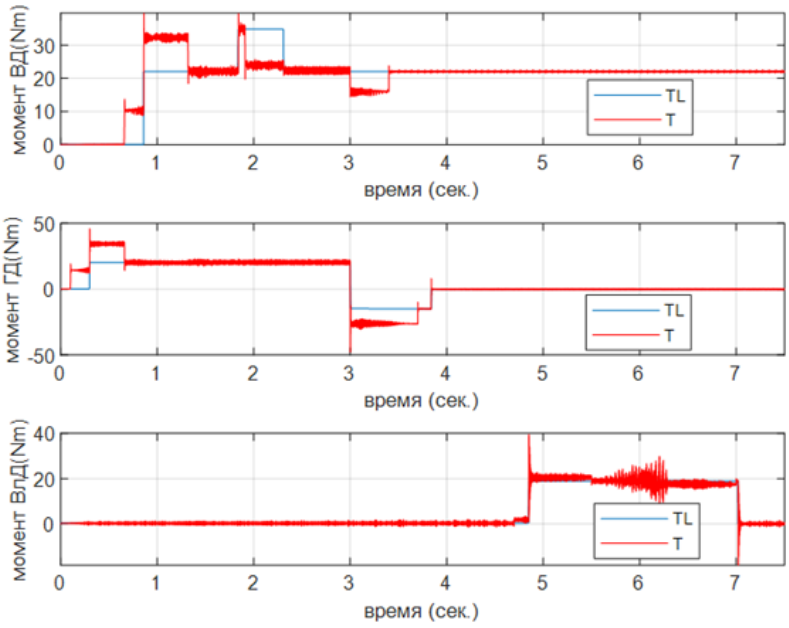

Figure 5.13: Load and actual torques of vertical, horizontal, and forks motors.

Motor currents are exhibited in Figure 5.15. Although vertical motors stopped moving at the top location of the shelf, dynamics in the current were recorded. This is because of the associated weight of the hoist which still has to be supported by the vertical motors.

Thus, the developed battery-supported power supply system achieved the designed targets. The battery system supplied the crane complex during grid disconnection and recovered the regenerated energy during the braking of drive systems.

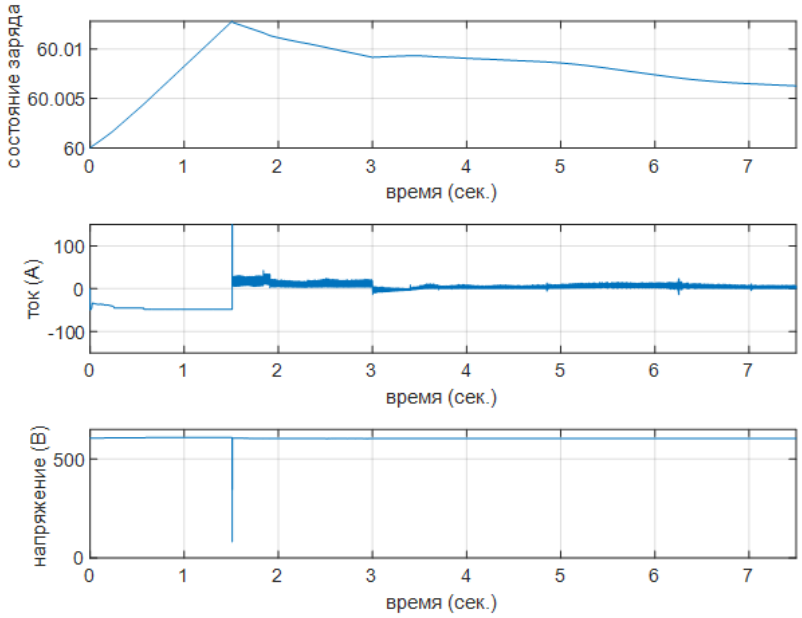

Figure 5.14: Battery response of third scenario.

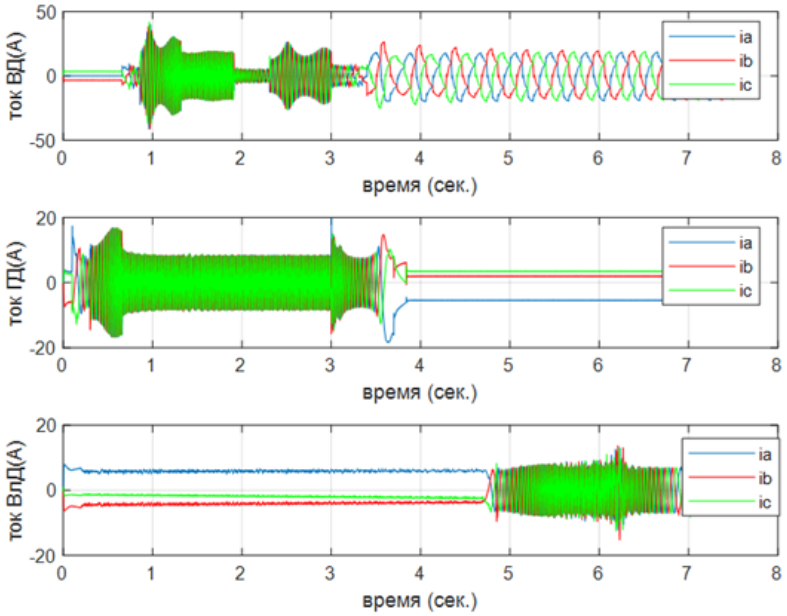

Figure 5.15: Three-phase currents of the stacker crane motors.

5.2.4 Analysis of Energy Consumption and Battery Supported Operation of ASC

In order to determine the energy consumption of the stacker crane complex in one cycle, it is required to calculate the total work for each movement.

1. The applied vertical work to lift the load W_v is equal to:

$$W_v = m * g * h \tag{5.2.3}$$

assuming:

- $m(ratedload) = 220kg$

- $g(gravitationalacceleration) = 9.81\frac{m}{s^2}$
- $h(craneheight) = 10m$

Which gives a nominal load of $W_v = 21.58kJ$. Now, considering a motor efficiency of ($\eta = 90\%$), the required input energy is calculated as:

$$E^v_{consumed} = \frac{W_v}{\eta} = 23.98kJ \tag{5.2.4}$$

Since the vertical movement is powered by two identical motors, the total input energy for vertical mechanism $E^v = 2 * 23.98kJ = 47.96kJ$.

2. For the horizontal movement, it is assumed that the crane travels along a (100 m) warehouse aisle at a constant speed of (2 m/s). The maximum travel time is:

$$Time = \frac{MaximumDistance}{Speed} = 50sec. \tag{5.2.5}$$

The consumed energy for the horizontal movement E^h is:

$$E^h_{consumed} = Power * Time = 7.5kW * 50sec. = 375kJ \tag{5.2.6}$$

assuming a drive system efficiency of ($\eta = 90\%$), the required input energy for horizontal movement is:

$$E^h = \frac{E^h_{consumed}}{\eta} = 416.67kJ \tag{5.2.7}$$

3. Similarly, the fork motor is assumed to operate for around (10 sec.) each cycle, given a total consumed energy of :

$$E^f_{consumed} = Power * Time = 1.1kW * 10sec. = 11kJ \tag{5.2.8}$$

considering the same drive efficiency:

$$E^f = \frac{E^f_{consumed}}{\eta} = 12.22kJ \tag{5.2.9}$$

4. The total energy consumption per one operational cycle can be calculated as:

$$E^total = E^v + E^h + E^f = 476.85kJ = 0.1325kWh \tag{5.2.10}$$

Then, by assuming a median of (100) daily operational cycles for the stacker crane complex, the total per day energy consumption of the stacker crane is 13.25 kWh. The installed battery has a capacity of 75 kWh, but only 70% of this capacity is usable since the state of charge (SOC) cannot go below 30%. Thus, the usable battery energy is:

$$E_{battery} = 75kW * 0.7 = 52.5kWh \tag{5.2.11}$$

This indicates that for the assumed operational conditions of the studied complex, the battery system can support the crane mechanism for 3.96 days of continuous

operation without relaying on the power grid.
By taking the regenerated drive systems energy into consideration, the battery system can be recharged and maintain longer supply period. It is assumed that the process of braking energy re-incorporation has an efficiency of ($\eta_r egen = 70\%$) due to losses in drive system and electrical components. However, the exact number is not known and difficult to anticipate practically. The regenerated vertical motors energy is determined as:

$$E^v_{regen} = 2 * E^v * \eta_{regen} = 30.22kJ \tag{5.2.12}$$

While the horizontal motor regenerated energy during deceleration is harder to calculate due to the obeisance of realistic reference braking energy curve. It would be presumed to have a low value by design which is around (7kJ). Moreover, the forks regenerated braking energy is ignored due to insignificant value. The total regenerated energy is:

$$E_{regen} = E^v_{regen} + E^h_{regen} = 37.22kJ = 0.01034kWhpercycle \tag{5.2.13}$$

For daily operation, this value is accumulated over the assumed number of cycles. The total collected energy by the battery system is:

$$E^{day}_{regen} = 100 * E_{regen} = 1.034kWh \tag{5.2.14}$$

By readjusting the previous calculations and the total consumed energy in equation 5.2.10 with energy saved per cycle, the number of battery supported days of operation becomes (4.29) days. This means that the re-incorporated energy provided approximately 7.6% more rune time to the crane complex. Finally, it is expected that this number would improve by adjusting the regenerated horizontal motor energy with real higher values which further justifies the proposed design.

5. The average daily cycles estimation utilized in the calculations was provided by the crane system manufacturer. However, by consulting warehouse operator websites, the actual estimation for daily cycles of such crane systems is about 200. Employing this number in the previous calculations resulted in a daily complex consumption of 26.5 kWh and a daily regenerated energy of 2.069 kWh. By adjusting the calculations according to the new estimation, the battery system can support a continuous operation of the crane complex for about (2.18) days without recharge.

6. The battery system sizing primarily depends on client operational requirements. The battery capacity, however, significantly affects the economic viability and the overall sizing of the power supply system. According to the previous calculations, the proposed integrated battery can support extended operational periods on the expense of initial system investment. When shorter islanded operational duration are required, a smaller battery system capacity can be proposed. This will decrease the cast, weight, and dimensions of the proposed battery-integrated power supply system. For a daily energy consumption of 26.5 kWh, the battery capacity can be recalculated based on

the client's requested power automated operation period. The following equation determines the battery capacity based on specific randomly suggested periods:

$$BatteryCapacity = EnergyConsumption * Duration \tag{5.2.15}$$

1. For 10 minutes of operation, the proposed battery capacity is 0.184 kWh.
2. For one hour of operation, the proposed battery capacity is 1.104 kWh.
3. For one day of operation, the proposed battery capacity is 26.5 kWh.

5.3 Solar-Based Hybrid Power Supply for ASC

Warehouses and distribution centers consume significant energy because of the cargo handling operations. Increased efficiency and reduced cost can be accomplished by integrating distributed renewable energy sources. Due to the rooftop abandonment in such installations, solar panels are regarded as valuable candidates for local energy generation. This enables warehouse energy autonomy and increases the power supply system reliability. In general, any distributed generator can be incorporated into the ASC power supply due to the employed battery system energy buffering capability. For example, some Russian regions experience harsh weather conditions during winter with low solar insolation levels. In these situations, wind energy installations, especially vertical axis wind turbines, could be employed to compensate for the low solar generation level [18; 19]. A hybrid power supply system can encapsulate renewable and nonrenewable sources, with the ability to store excess energy in battery systems. Many successful implementations of such configurations for hoist mechanisms were reviewed and analyzed in Chapter (1). Figure 5.16 demonstrates the employment of these principles in a warehouse scenario. The energy exchange was conducted on the common DC line, where grid supply and other sources contribute to the ASC group electrification.

In this section, only solar energy integration with the crane complex is considered. The same principle configuration of the solar energy generation unit presented in figure 2.2 was employed with (72.5 kW) generation capacity. The battery-integrated power supply system utilized in the previous section was used to energize the ASC and facilitate solar generation integration. System parameters and designed controllers preserved their values during the new simulation. This is an extremely important indication of the possibility of deploying various sources using the same power supply design. Figure 5.17 exhibits the supply side of the complex. The three-phase voltage and current at the grid side are observed to have a 180-degree phase difference during the exhibited period. This suggests that the solar energy generation at the selected period exceeded the required level to operate the crane complex and the excess energy used to support the grid. This is similar to the V2G and grid-supporting principles introduced in previous chapters. The solar panel output power underwent sudden unrealistic

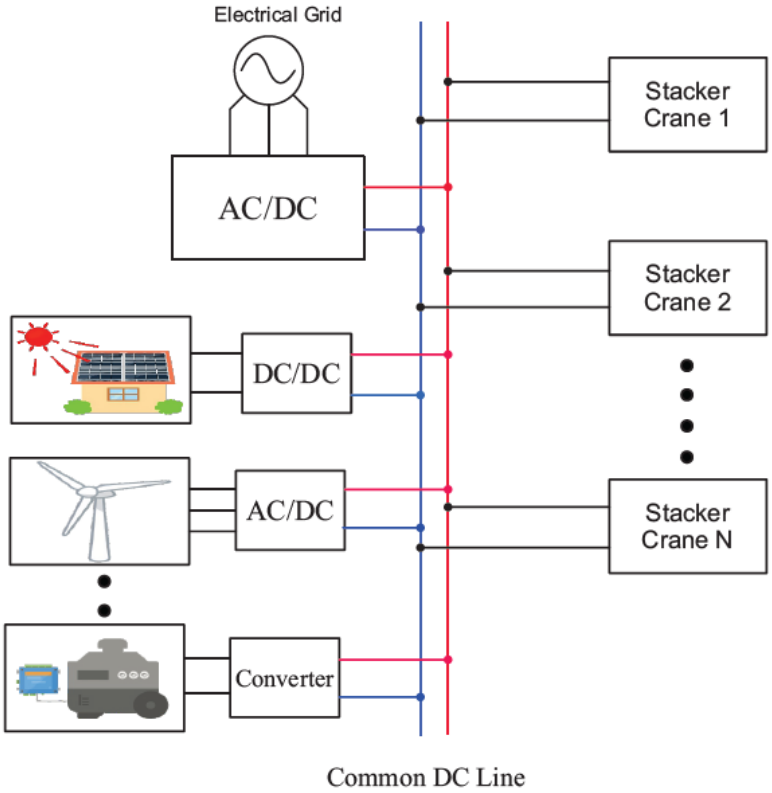

Figure 5.16: A group of stacker cranes powered by hybrid power supply.

drops. The actual changes in solar energy generation are much smoother with longer transition periods. However, these test scenarios are specially designed to evaluate the utilized power supply performance. This is a common control engineering practice to test the simulated designs with high disturbances or rapidly changing signals, exposing the system shortcomings. Additionally, these drops play an important role in reducing simulation time due to the compression of multiple events in short period of time. Concurrently, the DC line voltage fluctuated around the (600 V) level. This fluctuation is instigated by the experienced changes in the system, while the utilized hybrid power supply attempted to compensate and maintain the voltage level.

The third operational scenario examined in the previous section was used to evaluate the drive system performance. Figure 5.18 shows the speed tracking response of the crane motors. Similar to the results in figure 5.12, the vector control system accomplished perfect tracking performance and maintained the desired speed profile. It is important to notice that, the changes in the crane complex supply did not affect the operation of the crane drive systems. This highlights the successful utilization of the proposed power supply configuration.

The actual and load torques of the motors are exhibited in figure 5.19, where differences resulted from the acceleration and deceleration of the associated machine. The battery system response, shown in figure 5.20, is similar to the one obtained in figure 5.11. The power supply system switched from grid-supported to isolated operation at (1.5 sec.), where the battery discharged the crucial power to operate the drive com-

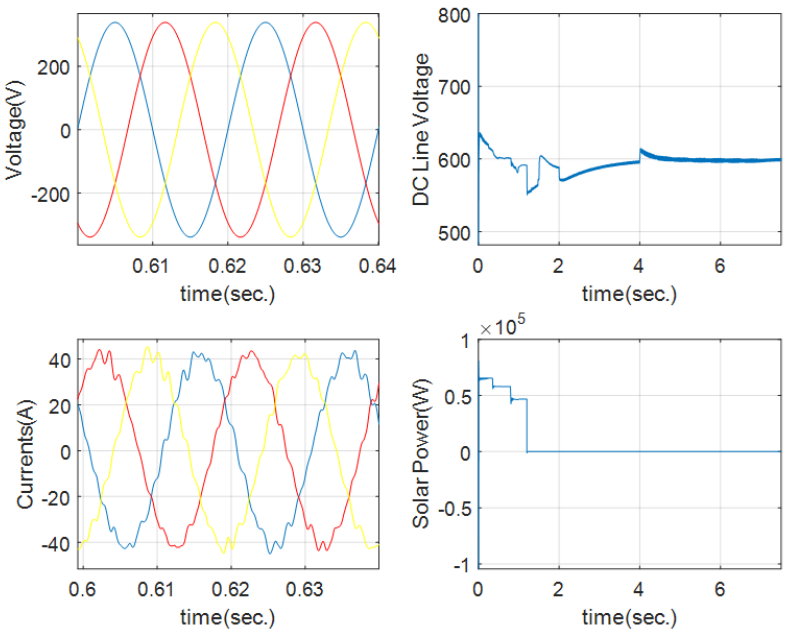

Figure 5.17: Hybrid power supply response.

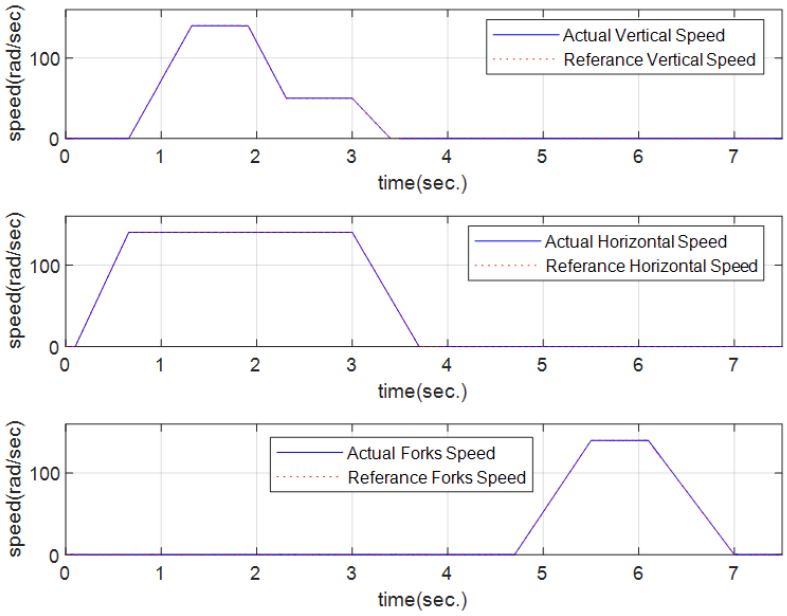

Figure 5.18: Speed response of crane motors for the hybrid power supply.

plex. The moment of supply switching concurs with the solar energy fading to reduce over-dependency on the grid-supplied energy.

5.4 ASC System as a Microgrid

The crane system is composed of four electrical drive systems representing the load maneuvering mechanisms. These loads and the associated power supply and converters can be considered as mini-grids, where energy management methods are appli-

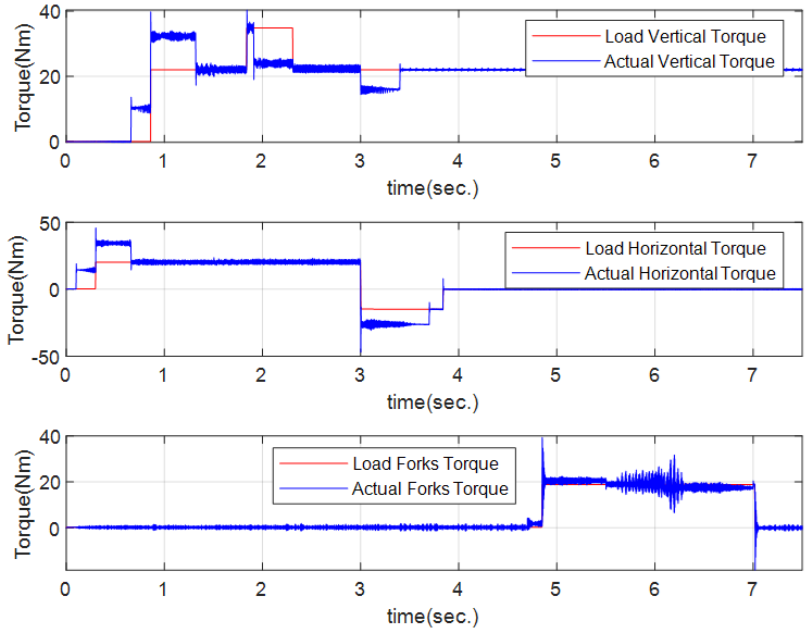

Figure 5.19: Torque response of crane motors for the hybrid power supply.

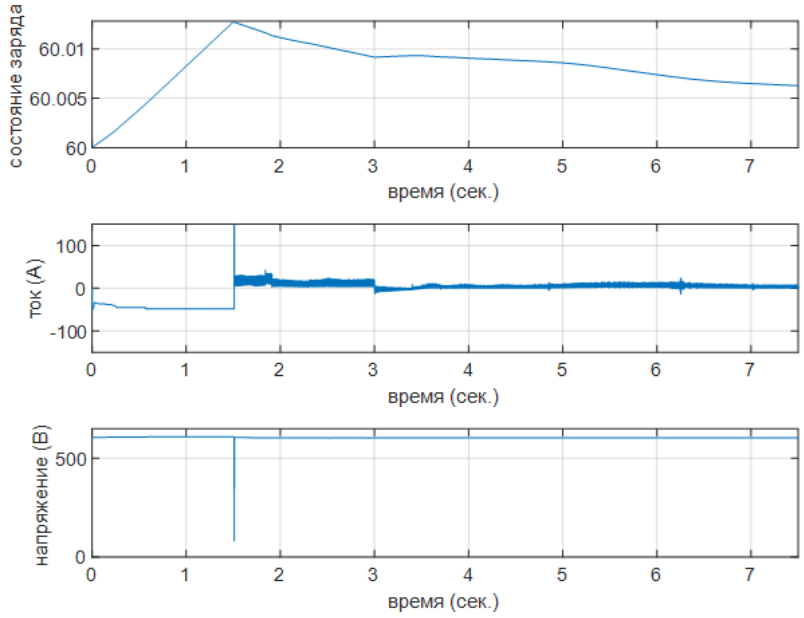

Figure 5.20: Battery response for the hybrid power supply.

cable. However, the objective of this section is to address the crane's complex interaction with surrounding technologies and devices. This interconnection between energy-exchanging complexes with internal energy storage capabilities holds more relevance to the Microgrid energy management algorithms addressed in Chapter(2). Those algorithms have the potential to regulate the extracted, consumed, and stored energy in each crane complex. In chapter (2), grid-tied and islanded configurations are addressed and studied. Grid-supporting droop controllers and fuzzy management control methods were proposed for the two operational circumstances. The focus of droop-based controllers is to organize the shared active and reactive power between different power

complexes and the grid, while the fuzzy management controller establishes a regulated energy transfer mechanism between isolated power systems. These concepts are re-examined and utilized in this section with an emphasis on ASC power supply system exploitation to facilitate energy exchange operations while maintaining internal crane performance. Furthermore, it is assumed that the crane's power supply system is integrated into solar energy generator. As in the previous case, the solar energy system experience significant unrealistic drops utilized to examine the proposed power supply performance in maintaining uninterrupted crane complex operation. In practice, solar energy variations are expected to be much smoother.

5.4.1 ASC with Droop Control

The operational scenario proposed in figure 2.4 is adapted to represent a grid-tied ASC system. The schematic configuration is demonstrated in figure 5.21, where the previously developed crane system is combined with an energy management algorithm. This is similar to warehouse applications where the crane system functions along several connected loads and devices. The objective of the droop controller, in this case, is to support the grid by reducing the three-phase connected load consumed power. Instead of extracting the DC sub-microgrid energy like in section (2.4), the employed controller utilizes the stored and generated energy in the hybrid power supply to achieve the required function. The three-phase load symbolizes any warehouse utility load like heating and lighting devices that consume power from the main grid. Thus, the aim is to reduce the total warehouse energy consumption. The second operational scenario examined in section (5.3.3) is re-explored to identify the droop control utilization advantages. Moreover, the solar energy used in the configuration is the same as in the previous section.

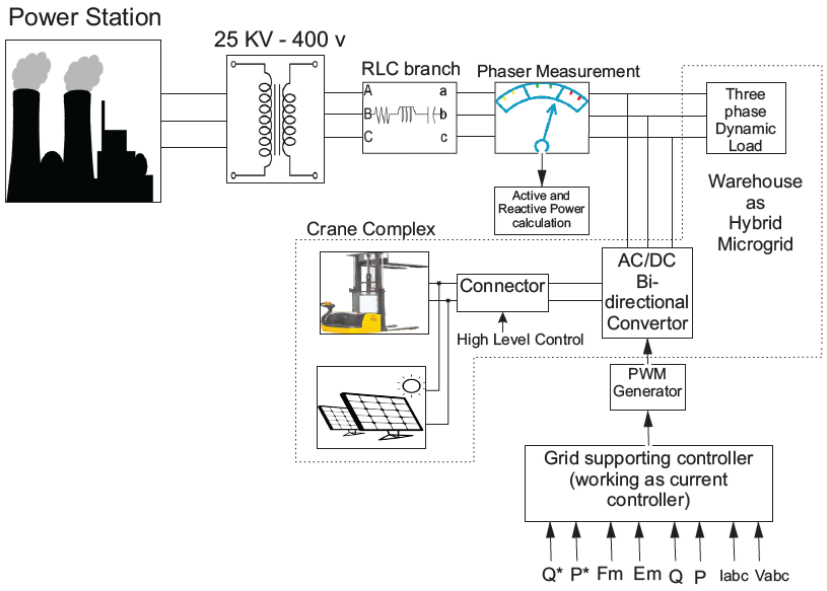

Figure 5.21: Warehouse configuration with grid-supporting functionality.

Figure 5.22 shows the solar energy generation of the hybrid power supply system along with the active and reactive power responses of the connected load. Two major drops were experienced in the solar generation, indicating the lack of solar irradiation required to support both load and crane operations. However, the load active and reactive power responses exhibit no variations, and each steady-state value is near their rated (10 kW) level. This implies that the load is being served by another source of energy in the complex.

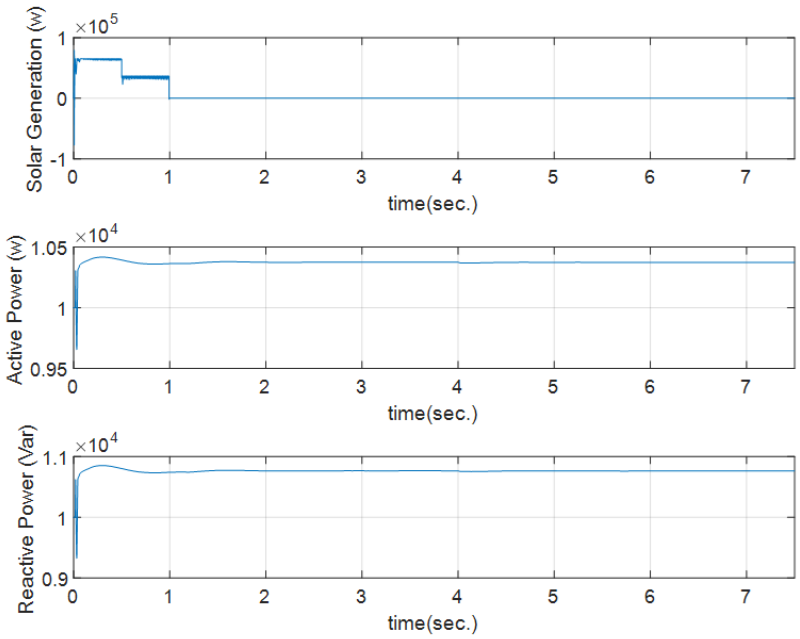

Figure 5.22: Grid controller performance on warehouse side.

Figure 5.23 exhibits the grid-side response of the addressed warehouse configuration. Rapid frequency regulation is witnessed in the figure where the fluctuation level did not exceed the maximum allowable transit range. The active and reactive powers absorbed from the grid are varying according to the hybrid power supply system contribution. Firstly, the grid injected high active power to regulate the connected load and other power elements like transformers. Then, the droop control action contributed to the load operation, reducing the active power and injecting reactive power into the grid. The experienced solar energy drops activated the high-level controller, isolating the crane side from the rest of the complex. This implies that the grid was required to compensate for the energy deficiency, which explains the increased active and reactive power levels. Finally, the crane-load connection is re-established when the braking mode is experienced in the explored operational scenario. This led to a decline in the active power level, reducing grid contribution once again.

The battery system response obtained from the droop control implementation was identical to the one in figure 5.20. The response is presented in figure 5.24. Although the crane experienced regenerative braking, the battery system continued to discharge power. This indicates that the discharged and regenerated powers are utilized in grid-

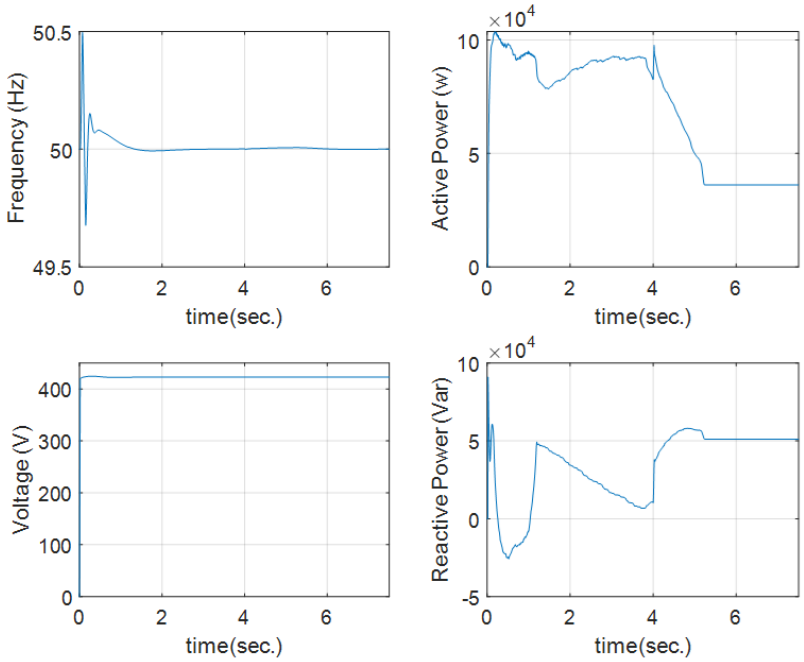

Figure 5.23: Droop controller performance on grid side.

support action. On the other hand, no degradation in crane performance was encountered during the test. The crane drive systems perfectly tracked their desired profile speeds, accomplishing the required maneuver. The crane performance is similar to figures5.8 and 5.9. ASC responses are not demonstrated to avoid repatriation.

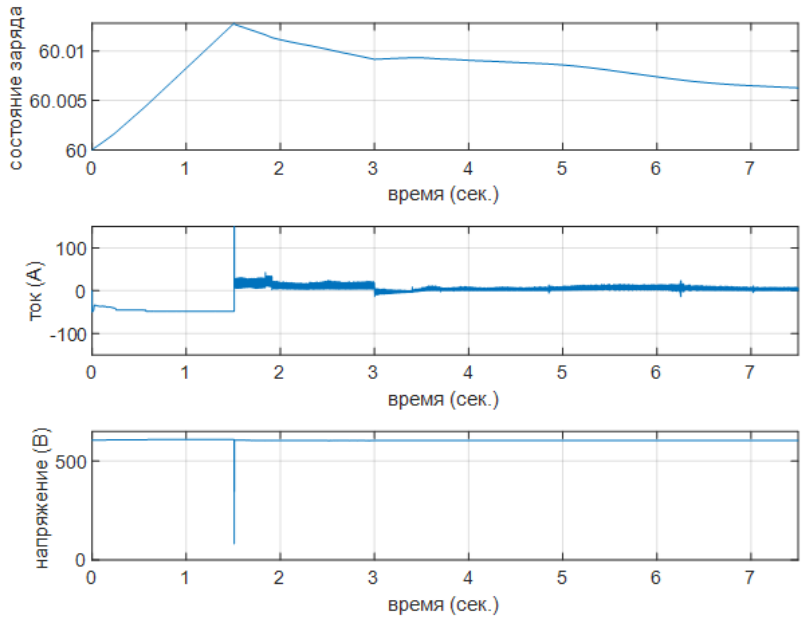

Figure 5.24: Battery response with droop controller.

5.4.2 Line-to-Line Power Transfer in Warehouse Scenario

A hybrid power supply system encompasses distributed generators and battery systems integrated within the crane complex. This configuration allows sustainable warehouse operation depending on local generation and storage capacity. This operational scenario is similar to the islanded Microgrid presented in section (2.5). In order to prevent the extinction of battery stored capacity during generation insufficiency, energy sharing between multiple ASC complexes is enabled. A bidirectional DC/DC converter is utilized to perform the energy transfer between different power lines. The energy-sharing principles were studied and broadly evaluated in Chapter (2). The energy is extracted from a crane system undergoing an extended halt period and injected into an active crane complex. This decreases the operational burden of the active crane battery system by preventing over-depletion, which will result in battery state-of-health SoH improvement. The fuzzy management control algorithm presented in (2.5.2) is employed to regulate the shared energy between the two power lines. The fundamental structure of such a system is demonstrated in figure 5.25. An isolated DC/DC converter is preferred for power transfer between different lines because of the shock prevention properties and ensured galvanic isolation. However, in the studied islanded complex, even a non-isolated converter can be employed due to the absence of a main grid connection. The exchanged current capacity and direction are decided by the fuzzy management controller, providing reference current signals based on local generation level and load demand. After comparison with the real current, a PID controller was used to regulate the DC/DC converter operation.

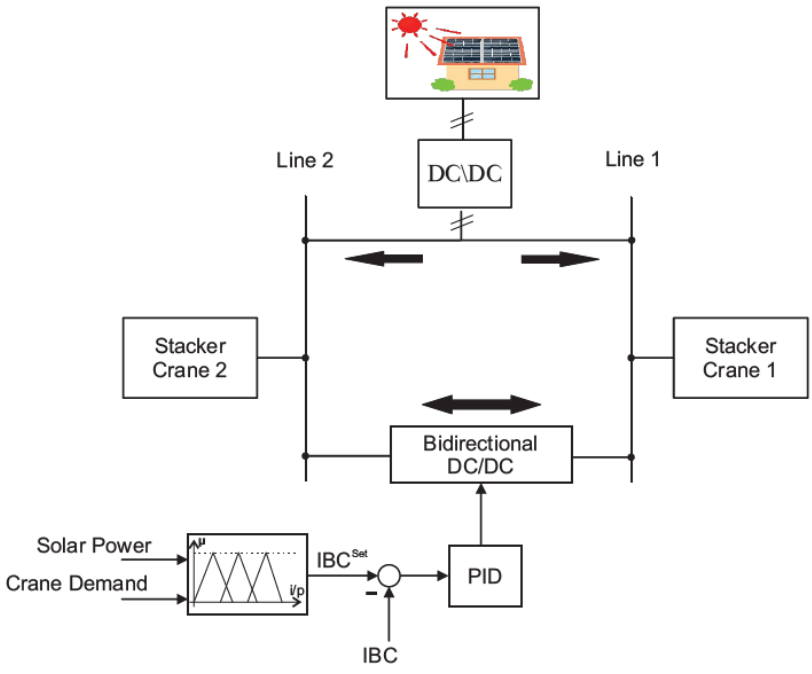

Figure 5.25: Energy sharing power lines in automated warehouse.

The PV solar panels generate adequate energy to operate the crane complex and

charge the onboard batteries. Nevertheless, renewable energy fluctuation issues are tackled using the battery system and the shared power from paused cranes. Although the interactions between only two crane complexes are considered in this study, dozens of ASC are usually deployed in typical warehouses to transfer produce between stacking shovels. The ASC system structure is illustrated in figure 5.26, where the bidirectional converter is viewed as a distributed generator connected to the common DC line. The internal architecture of the crane system and the utilized power supply were maintained, which again highlights the flexibility and adaptability of the proposed power supply system.

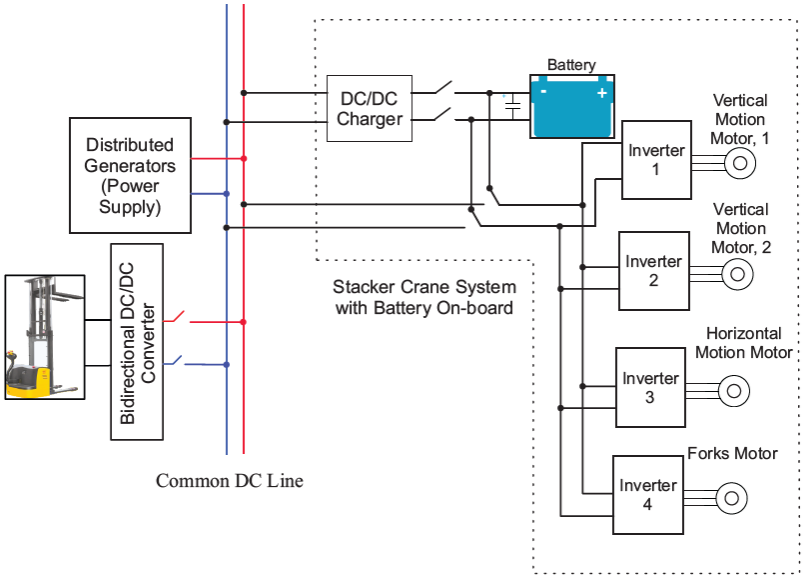

Figure 5.26: Structure of ASC with multiple line contribution.

Figure 5.27 exhibits the fuzzy management system normalized inputs and output. The fuzzy system uses membership functions and the internal mechanism to determine the best injected current value. In the figure, the solar generation experiences three drops, while the negative normalized demand values represent the regenerated energy during the braking mode of drive systems. During excess energy generation, the fuzzy manager utilized the interlinking converter to charge the donor crane battery with a negative current, indicating that operation. Meanwhile, the solar drop provoked a reversed power direction toward the active crane complex. The current settled at zero level during the braking mode of the active crane since no power contribution is required. This implies that the employed fuzzy management controller operates efficiently to inject only the required power and reduce losses. On the other hand, the current response shows that the actual current was excellently tracked using the deployed PID controller.

The associated active crane speed and torque responses are displayed in figures 5.28 and 5.29. Again, the results of only one of the vertical motors are shown because of the assumed symmetrical design. Speed controllers achieved successful tracking of

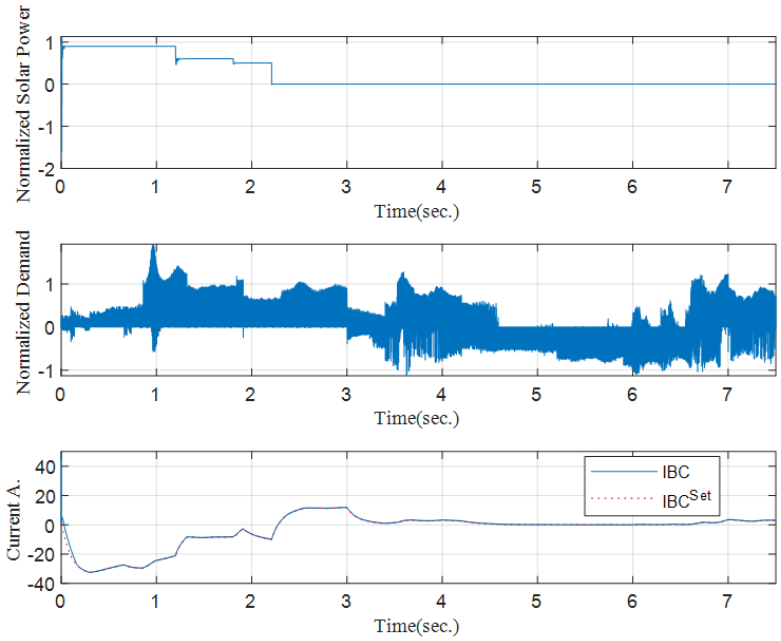

Figure 5.27: Energy management system inputs and output.

the speed profile with no apparent influence of the experienced changes in the power supply part of the system. As previously explained, the differences between the actual and load torque responses are the product of speed variations.

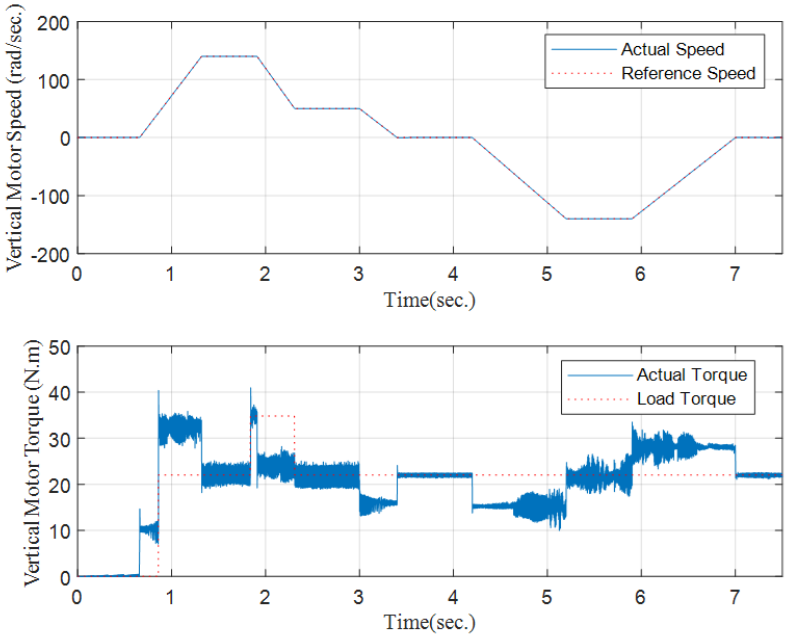

Figure 5.28: Vertical motion motor response.

The donor crane battery response is illustrated in figure 5.30. The battery current was directly observed similar to the response presented in figure 5.27. This is an anticipated result since the current passed through the interlinking DC/DC converter is supplied by the donor battery. The SoC response reveals the charging and discharging stages encountered during the operational scenario. The degradation in solar generation

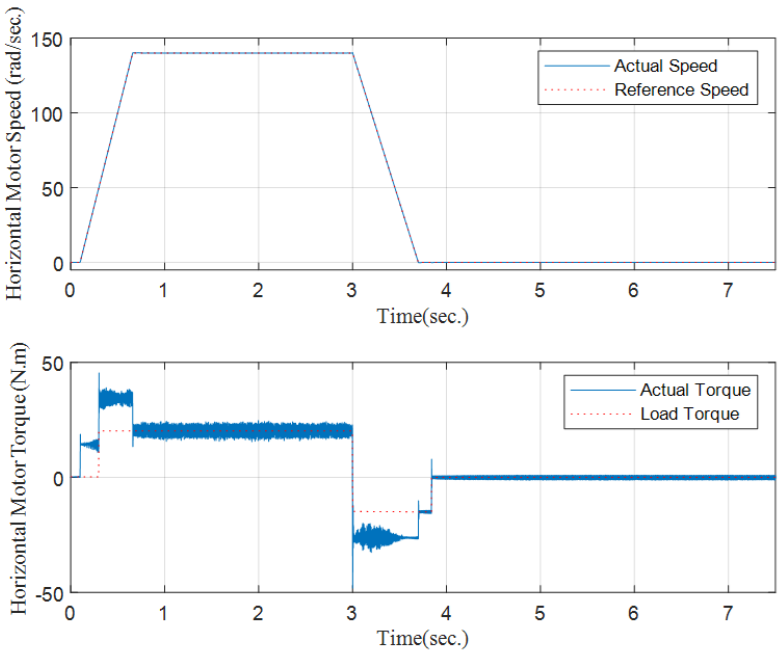

Figure 5.29: Horizontal motion motor response.

slowed the charging rate of the battery before flipping to the discharge mode. In the last stage of the response, the almost flat SoC curve corresponds to the braking mode in the active crane complex, which indicates no power was extracted from the donor battery system.

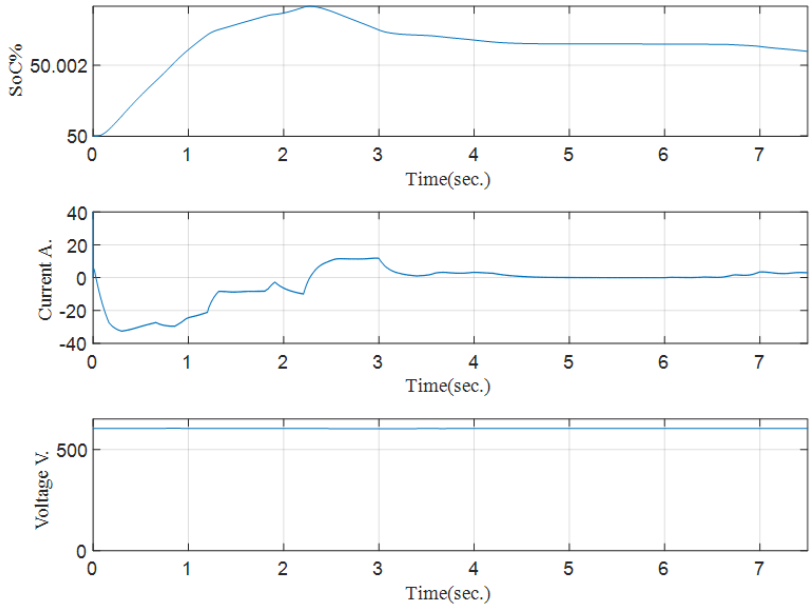

Figure 5.30: Donor crane battery response.

On the other hand, the active crane battery response is shown in figure 5.31, where the SoC increased during the first stage and stabilized when line-to-line power transfer mode was initiated. The response implies that the battery did not contribute to the electrification of the crane complex during that period. However, the occurrence

of braking mode reactivated the battery system to recover the regenerated energy from the drive systems. This is evident by the slight increase in SoC rate and the negative current value exhibited at that period.

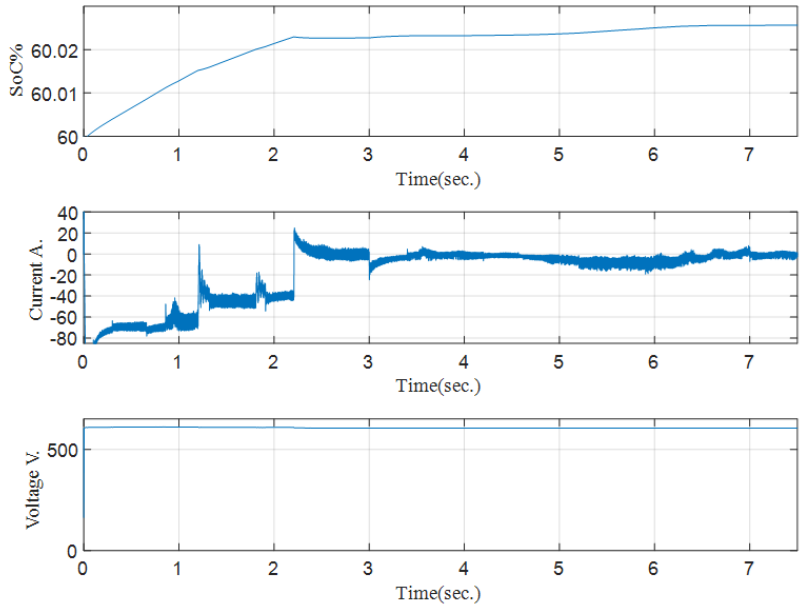

Figure 5.31: Active crane battery response.

5.5 Conclusion of chapter five

The effectiveness of the previously developed battery-supported power supply system components has been investigated. An automated stacker crane complex was selected and studied as one of many hoist and transport applications. The addressed ASC system was inspired by an actual implementation manufactured by the (РУХЛО) company. Power converters and drive systems were modeled and simulated according to the obtained parameters and specifications of the existing crane complex. The exploitation of a battery system in the crane power supply can reduce dependency on the electricity grid, which boosts the system's reliability. Moreover, it can retrieve the regenerated energy produced by braking mode and load-lowering maneuvers. This energy is usually dispersed using dump loads, which limits the overall electrical complex efficiency. By exploring the actual crane system power and current responses, design specifications for the power supply system, including the battery capacity and employed converter's topological limitation, were obtained. The proposed modified crane complex can charge from the grid during normal operation, while a circuit barker unit can isolate the battery and drive complex during the standalone mode. The designed battery system can maintain the crane's full functionality for (2000) cycles without recharge. During that period, the recovered drive system energy can further extend the operational range of the isolated crane complex. Integrating renewable distributed generators like

solar panels can prompt warehouse power autonomy and add reliability to the complex. The proposed power supply system facilitated the new source integration without additional system or controller adjustments, which is considered one of the most significant achieved advantages. Furthermore, the complex's switching operational modes correspond to the previously studied and evaluated Microgrid configurations with energy management controllers. Therefore, the correlation between functionalities established the applicability of grid-tied and islanded Microgrid scenarios in warehouse applications. A grid-supporting droop controller was utilized to assist in regulating warehouse-connected load. Frequency and voltage across the load were maintained, while the active and reactive powers extracted from the grid were minimized. On the other hand, to prevent over-depletion of an active crane battery capacity during the islanded mode, energy transfer between power lines of different crane complexes was invoked. This was enabled by utilizing a bidirectional DC/DC converter controlled by a fuzzy management algorithm. The power is donated by an extensively paused crane complex, which assisted in reducing the charge/discharge cycles of the active crane battery system. This can enhance the overall battery state of health. In conclusion, the proposed integration of battery-supported power supply systems can increase efficiency, induce reliability, and facilitate the interaction of ASC systems with surrounding complexes in warehouse applications.

Conclusion

The proposed modernization of power supply systems operating electric drives of hoist and transport mechanisms, integrates energy storage devices to induce increased efficiency, stability and reliability of their operation. Battery-supported power supply system facilitates the incorporation of various local energy, prevents interruptions in the energy supply, and recovers the regenerated braking energy in electric motors. The dissertation demonstrated that the power supply control system of such a multi-motor electrical complex is built on a multi-level principle. For each level, various energy management algorithms were synthesized, power regulators and converters were constructed, and new operational structures were proposed. The following results were accomplished:

1. The efficiency and scope of application of control algorithms regulating transferred and stored energy in electrical complexes for various operational scenarios were explored. It is illustrated that, based on the basic configuration of the local power system and operating conditions of the electrical complex, the employed type of energy management regulator varies significantly. A number of regulators were proposed for grid-tied and isolated electrical complexes operating with various load configurations. Fundamental recommendations were proposed for the implementation of each developed energy management algorithm in the warehouse power supply system operated as a Microgrid. Based on the availability of local energy sources and stored energy in the battery system, the proposed energy management methods can ensure power supply autonomy and load profile peak reduction of the electrical complexes.
2. A comprehensive study evaluated battery charger topologies and their associated control systems. Consequently, a wide voltage-range LLC resonant converter was developed and practically implemented. The proposed charger can achieve a wide regulation range while maintaining relatively low switching losses. Furthermore, the accuracy of the computer-based converter model was evaluated by comparing simulation and practical results.
3. A battery system emulation testbench was constructed for the assessment and validation of newly designed battery technologies. The developed testbench can safely and efficiently imitate lithium-ion battery dynamics while interacting with a charging device. Based on the model development environment, two versions of the testbench were proposed and evaluated. The LabView-based battery emulator can

achieve battery model reparameterization flexibility, while the STM-based battery emulator is more compact and application-oriented. Compared with commercially available battery emulators, the proposed test bench has lower price and high reconfiguration.

4. A Battery-supported power supply system for electric drives of automated warehouse stacker cranes was proposed. An extensive study was provided where different operational scenarios and the influence of internal and external system variations were examined. Recommendations were proposed for the implementation and selection of battery capacity depending on the complex's autonomous operation mode duration. Compared with the original configuration used by the crane manufacturer, the proposed system demonstrated economic and operational advantages.

The achieved results are encouraging and offer future research prospects in various fields. Currently, a test-bed is being developed to investigate the energy interaction between the electric drive complex and the battery system. The test-bed configuration is based on the HiL technique principles, where both electric complex and battery models are modeled and deployed on different processors. The objective of such an experimental setup is to investigate the applicability and performance of various control algorithms operating on both devices. Such a test-bed will assist researchers and developers in constructing power-efficient and reliable controllers. Another prospect includes the reconstruction of the battery emulator testbench to operate on the charging station at full power. This research direction is commercially motivated by companies requesting test platforms for their developed charging technologies. However, the requested device power rating is challenging and requires redesigning the entire testbench structure.

List of Figures

References

1. A. Khalid, A. Stevenson, A. I. Sarwat. Overview of technical specifications for grid-connected microgrid battery energy storage systems // IEEE Access. — 2021. — Vol. 9. — P. 163554–163593.
2. A. Turksoy, A. Teke, A. Alkaya. A comprehensive overview of the dc-dc converter-based battery charge balancing methods in electric vehicles // Renewable and Sustainable Energy Reviews. — 2020. — Vol. 133. — P. 110274.
3. T. Haniszewski, M. Cieśla. Energy harvesting in the crane-hoisting mechanism // Energies. — 2022. — Vol. 15, no. 24. — P. 9366.
4. Lift Energy Storage Technology: A solution for decentralized urban energy storage / J. D. Hunt, A. Nascimento, B. Zakeri, J. Jurasz, P. B. Dabek, P. S. F. Barbosa, R. Brandao, N. J. de Castro, W. Leal Filho, K. Riahi // Energy. — 2022. — Vol. 254. — P. 124102.
5. P. A. Aranaga Decori. Implementation of energy recovery and storage systems in cranes in the Port of Gävle. — 2020.
6. Modeling and Controls of Flywheel Energy Storage Systems for Energy Harvesting from Harbor Electrical Cranes / N. B. B. Ahamad, C.-L. Su, Z. Xiao, J. C. Vasquez, J. M. Guerrero // 2018 IEEE Industry Applications Society Annual Meeting (IAS). — Portland, OR, USA : IEEE, 2018. — P. 1–8.
7. M. M. Flynn, P. McMullen, O. Solis. High-Speed Flywheel and Motor Drive Operation for Energy Recovery in a Mobile Gantry Crane // APEC 2007 – Twenty-Second Annual IEEE Applied Power Electronics Conference and Exposition. — Anaheim, CA, USA : IEEE, 2007. — P. 1151–1157.
8. Power Balancing in STS Group Cranes with Flywheel Energy Storage Based on DSM Strategy / M. Kermani, G. Parise, L. Martirano, L. Parise, B. Chavdarian //

2018 IEEE 59th International Scientific Conference on Power and Electrical Engineering of Riga Technical University (RTUCON). — Riga, Latvia : IEEE, 2018. — P. 1–5.

9. D. Iannuzzi, L. Piegari, P. Tricoli. Use of Supercapacitors for Energy Saving in Overhead Travelling Crane Drives // 2009 International Conference on Clean Electrical Power (ICCEP). — Capri, Italy : IEEE, 2009. — P. 562–568.
10. S.-M. Kim, S.-K. Sul. Control of rubber tyred gantry crane with energy storage based on supercapacitor bank // IEEE transactions on power electronics. — 2006. — Vol. 21, no. 5. — P. 1420–1427.
11. The ultracapacitor-based controlled electric drives with braking and ride-through capability: Overview and analysis / P. J. Grbović, P. Delarue, P. Le Moigne, P. Bartholomeus // IEEE Transactions on Industrial Electronics. — 2010. — Vol. 58, no. 3. — P. 925–936.
12. H. Yoshihara. Energy Saving System Trend for Harbor Crane with Lithium-Ion Battery // 2018 International Power Electronics Conference (IPEC-Niigata 2018 - ECCE Asia). — Niigata, Japan : IEEE, 2018. — P. 219–226.
13. Hybridization of rubber tired gantry (RTG) cranes / M. Antonelli, M. Ceraolo, U. Desideri, G. Lutzemberger, L. Sani // Journal of Energy Storage. — 2017. — Vol. 12. — P. 186–195.
14. K. Lewczuk, M. Klodawski, P. Gepner. Energy consumption in a distributional warehouse: A practical case study for different warehouse technologies // Energies. — 2021. — Vol. 14, no. 9. — P. 2709.
15. A. Meneghetti, F. Dal Magro, P. Simeoni. Fostering renewables into the cold chain: how photovoltaics affect design and performance of refrigerated automated warehouses // Energies. — 2018. — Vol. 11, no. 5. — P. 1029.
16. H. M. Jassim, M. Mudrov, A. Zyuzev. Hybrid Solar-Based Power Supply for a Stacker Crane System // 2024 International Conference on Industrial Engineering, Applications and Manufacturing (ICIEAM). — Location TBD : IEEE, 2024. — P. 299–304.

17. S. Hajdu, P. Gáspár. Distributed parameter modeling of single-mast stacker crane structures // Periodica Polytechnica Transportation Engineering. — 2014. — Vol. 42, no. 1. — P. 1–9.

18. L. Proskuryakova. Russia's renewable energy sector: Policy recommendations // Centrum Balticum Foundation, BSR Policy Briefing Series. — 2022.

19. Green energy development in an industrial region: A case-study of Sverdlovsk region / A. Karaeva, E. Magaril, V. Torretta, M. Ragazzi, E. C. Rada // Energy Reports. — 2021. — Vol. 7. — P. 137–148.

20. N. M. Tabatabaei, E. Kabalci, N. Bizon. Microgrid architectures, control and protection methods. — Springer, 2019.

21. R. Lasseter, M. Erickson. Integration of battery-based energy storage element in the CERTS microgrid // University of Wisconsin-Madison, Oct. — 2009.

22. D. Kanakadhurga, N. Prabaharan. Demand side management in microgrid: A critical review of key issues and recent trends // Renewable and Sustainable Energy Reviews. — 2022. — Vol. 156. — P. 111915.

23. C. Yuan, M. A. Haj-Ahmed, M. S. Illindala. Protection strategies for medium-voltage direct-current microgrid at a remote area mine site // IEEE Transactions on Industry Applications. — 2015. — Vol. 51, no. 4. — P. 2846–2853.

24. Leading the charge: Microgrids for domestic military installations / S. Van Broekhoven, N. Judson, J. Galvin, J. Marqusee // IEEE Power and Energy Magazine. — 2013. — Vol. 11, no. 4. — P. 40–45.

25. Hybrid Microgrid Management Using Optimized Grid Support Controller / H. Jassim [et al.] // Bulletin of the Moscow Power Engineering Institute. — 2023. — No. 5. — P. 11–19.

26. F. Tlili, A. Kadri, F. Bacha. Advanced control strategy for bidirectional three phase AC/DC converter // Electric Power Systems Research. — 2020. — Vol. 179. — P. 106078.

27. Q.-C. Zhong, G. C. Konstantopoulos. Current-limiting droop control of grid-connected inverters // IEEE Transactions on Industrial Electronics. — 2016. — Vol. 64, no. 7. — P. 5963–5973.

28. Control and modulation of bidirectional single-phase AC–DC three-phase-leg SPWM converters with active power decoupling and minimal storage capacitance / H. Wu, S.-C. Wong, K. T. Chi, Q. Chen // IEEE Transactions on Power Electronics. — 2015. — Vol. 31, no. 6. — P. 4226–4240.

29. Model predictive control—Based distributed control algorithm for bidirectional interlinking converter in hybrid microgrids / S. U. Ali, M. Aamir, A. R. Jafri, U. Subramaniam, F. Haroon, A. Waqar, M. Yaseen // International Transactions on Electrical Energy Systems. — 2021. — Vol. 31, no. 10. — e12817.

30. G. Melath, S. Rangarajan, V. Agarwal. A novel control scheme for enhancing the transient performance of an islanded hybrid AC–DC microgrid // IEEE Transactions on Power Electronics. — 2019. — Vol. 34, no. 10. — P. 9644–9654.

31. M. J. Rana, M. A. Abido. Energy management in DC microgrid with energy storage and model predictive controlled AC–DC converter // IET Generation, Transmission & Distribution. — 2017. — Vol. 11, no. 15. — P. 3694–3702.

32. Control of hybrid AC/DC microgrid under islanding operational conditions / G. Ding, F. Gao, S. Zhang, P. C. Loh, F. Blaabjerg // Journal of Modern Power Systems and Clean Energy. — 2014. — Vol. 2, no. 3. — P. 223–232.

33. T. Ma, M. H. Cintuglu, O. A. Mohammed. Control of a hybrid AC/DC microgrid involving energy storage and pulsed loads // IEEE Transactions on industry applications. — 2016. — Vol. 53, no. 1. — P. 567–575.

34. K. Rajesh, S. Dash. Load frequency control of autonomous power system using adaptive fuzzy based PID controller optimized on improved sine cosine algorithm // Journal of Ambient Intelligence and Humanized Computing. — 2019. — Vol. 10. — P. 2361–2373.

35. H. M. Jassim, Z. Anatoliy. FUZZY MANAGEMENT CONTROLLER FOR AUTONOMOUS POWER SUPPLY SYSTEM BASED ON ACTIVE NEUTRAL MULTILEVEL INVERTER // Perm National Research Polytechnic University, Bul-

letin. Electrotechnics, information technologies, control systems. — 2023. — No. 45. — P. 5–30.

36. A. Yasin. Energy management of a stand-alone DC microgrid based on PV/Wind/Battery/Diesel Gen. combined with super-capacitor // International Journal of Renewable Energy Research. — 2019. — Vol. 9, no. 4. — P. 1811–1826.

37. P. J. Corral-Vega, P. García-Triviño, L. M. Fernández-Ramírez. Design, modelling, control and techno-economic evaluation of a fuel cell/supercapacitors powered container crane // Energy. — 2019. — Vol. 186. — P. 115863.

38. S. R. A. Bolonne, D. P. Chandima. Narrow band state of charge (SOC) control strategy for hybrid container cranes // Energies. — 2019. — Vol. 12, no. 4. — P. 743.

39. Cooperative synchronization in distributed microgrid control / A. Bidram, V. Nasirian, A. Davoudi, F. L. Lewis, [et al.]. — Springer, 2017.

40. Comparison of hierarchical control and distributed control for microgrid / X. Feng, A. Shekhar, F. Yang, R. E. Hebner, P. Bauer // Electric Power Components and Systems. — 2017. — Vol. 45, no. 10. — P. 1043–1056.

41. H. M. Jassim, A. Ziuzev. Dual Droop-Based Controllers for Hybrid Microgrid with Photovoltaic and Wind Turbine Distributed Generators // 2022 International Ural Conference on Electrical Power Engineering (UralCon). — Yekaterinburg, Russia : IEEE, 2022. — P. 417–422.

42. A. Bidram, A. Davoudi. Hierarchical structure of microgrids control system // IEEE Transactions on Smart Grid. — 2012. — Vol. 3, no. 4. — P. 1963–1976.

43. Coordination control of hybrid AC/DC microgrid / B. Liang, L. Kang, J. He, F. Zheng, Y. Xia, Z. Zhang, Z. Zhang, G. Liu, Y. Zhao // The Journal of Engineering. — 2019. — Vol. 2019, no. 16. — P. 3264–3269.

44. Decentralized economic operation control for hybrid AC/DC microgrid / P. Yang, M. Yu, Q. Wu, P. Wang, Y. Xia, W. Wei // IEEE Transactions on Sustainable Energy. — 2019. — Vol. 11, no. 3. — P. 1898–1910.

45. M. M. Mahdi, E. M. Thajeel, A. Z. Ahmad. Load Frequency Control for Hybrid Microgrid Using MRAC with ANN under Sudden Load Changes // 2018 Third Scientific Conference of Electrical Engineering (SCEE). — Baghdad, Iraq : IEEE, 2018. — P. 220–225.

46. M. M. Mahdi, A. Z. Ahmad. Load Frequency Control in Microgrid Using Fuzzy Logic Table Control // 2017 11th IEEE International Conference on Compatibility, Power Electronics and Power Engineering (CPE-POWERENG). — Madrid, Spain : IEEE, 2017. — P. 318–323.

47. H. M. Jassim, A. Ziuzev. Optimized-Fuzzy Droop Controller for Load Frequency Control of a Microgrid with Weak Grid Connection and Disturbances // 2022 29th International Workshop on Electric Drives: Advances in Power Electronics for Electric Drives (IWED). — Location TBD : IEEE, 2022. — P. 1–7.

48. U. Datta, J. Shi, A. Kalam. Primary frequency control of a microgrid with integrated dynamic sectional droop and fuzzy based pitch angle control // International Journal of Electrical Power & Energy Systems. — 2019. — Vol. 111. — P. 248–259.

49. M. A. Mosa, A. Ali. Energy management system of low voltage dc microgrid using mixed-integer nonlinear programing and a global optimization technique // Electric Power Systems Research. — 2021. — Vol. 192. — P. 106971.

50. Smart microgrids operation considering a variable neighborhood search: The differential evolutionary particle swarm optimization algorithm / J. Garcia-Guarin, D. Rodriguez, D. Alvarez, S. Rivera, C. Cortes, A. Guzman, A. Bretas, J. R. Aguero, N. Bretas // Energies. — 2019. — Vol. 12, no. 16. — P. 3149.

51. R. Zahedi, M. Ardehali. Power management for storage mechanisms including battery, supercapacitor, and hydrogen of autonomous hybrid green power system utilizing multiple optimally-designed fuzzy logic controllers // Energy. — 2020. — Vol. 204. — P. 117935.

52. Z. Roumila, D. Rekioua, T. Rekioua. Energy management based fuzzy logic controller of hybrid system wind/photovoltaic/diesel with storage battery // Interna-

tional Journal of Hydrogen Energy. — 2017. — Vol. 42, no. 30. — P. 19525–19535.

53. Performance improvement strategy for parallel-operated virtual synchronous generators in microgrids / H. Zhang, R. Zhang, K. Sun, W. Feng // Journal of Power Electronics. — 2019. — Vol. 19, no. 2. — P. 580–590.

54. I. Serban, C. P. Ion. Microgrid control based on a grid-forming inverter operating as virtual synchronous generator with enhanced dynamic response capability // International Journal of Electrical Power & Energy Systems. — 2017. — Vol. 89. — P. 94–105.

55. H. M. Jassim, P. Pustokhin, A. Zyuzev. Supervised Droop Controller Based on Virtual Synchronous Generator for Islanded Microgrid // 2023 5th International Conference on Control Systems, Mathematical Modeling, Automation and Energy Efficiency (SUMMA). — Moscow, Russia : IEEE, 2023. — P. 1070–1075.

56. A comprehensive review of power converter topologies and control methods for electric vehicle fast charging applications / M. Safayatullah, M. T. Elrais, S. Ghosh, R. Rezaii, I. Batarseh // IEEE Access. — 2022. — Vol. 10. — P. 40753–40793.

57. A. Khaligh, M. D'Antonio. Global trends in high-power on-board chargers for electric vehicles // IEEE Transactions on Vehicular Technology. — 2019. — Vol. 68, no. 4. — P. 3306–3324.

58. Hybrid three-phase rectifiers with active power factor correction: A systematic review / J. T. Gonçalves, S. Valtchev, R. Melicio, A. Gonçalves, F. Blaabjerg // Electronics. — 2021. — Vol. 10, no. 13. — P. 1520.

59. High-voltage stations for electric vehicle fast-charging: trends, standards, charging modes and comparison of unity power-factor rectifiers / I. Aretxabaleta, I. M. De Alegria, J. Andreu, I. Kortabarria, E. Robles // IEEE Access. — 2021. — Vol. 9. — P. 102177–102194.

60. J. Halbig. 15kW Bidirectional Vienna PFC // 2014 IEEE Applied Power Electronics Conference and Exposition (APEC). — Location TBD : IEEE, 2020.

61. High Efficiency Three-Phase Interleaved Buck-Type PFC Rectifier Concepts / M.-C. Ancuti, C. Sorandaru, S. Musuroi, V.-N. Olarescu // IECON 2015-41st Annual Conference of the IEEE Industrial Electronics Society. — Location TBD : IEEE, 2015. — P. 004990–004995.

62. Design and implementation of a two-channel interleaved Vienna-type rectifier with> 99% efficiency / Q. Wang, X. Zhang, R. Burgos, D. Boroyevich, A. M. White, M. Kheraluwala // IEEE Transactions on Power Electronics. — 2017. — Vol. 33, no. 1. — P. 226–239.

63. A digital control strategy with simple transfer matrix for three-phase buck rectifier under unbalanced AC input conditions / Q. Chen, J. Xu, R. Huang, W. Wang, L. Wang // IEEE Transactions on Power Electronics. — 2020. — Vol. 36, no. 4. — P. 3661–3666.

64. H. Haga, F. Kurokawa. Modulation method of a full-bridge three-level LLC resonant converter for battery charger of electrical vehicles // IEEE Transactions on Power Electronics. — 2016. — Vol. 32, no. 4. — P. 2498–2507.

65. H. Wang, S. Dusmez, A. Khaligh. Design and analysis of a full-bridge LLC-based PEV charger optimized for wide battery voltage range // IEEE Transactions on Vehicular technology. — 2013. — Vol. 63, no. 4. — P. 1603–1613.

66. T. Mishima, K. Akamatsu, M. Nakaoka. A high frequency-link secondary-side phase-shifted full-range soft-switching PWM DC–DC converter with ZCS active rectifier for EV battery chargers // IEEE Transactions on Power Electronics. — 2013. — Vol. 28, no. 12. — P. 5758–5773.

67. J. Dudrik, M. Bodor, M. Pástor. Soft-switching full-bridge PWM DC–DC converter with controlled output rectifier and secondary energy recovery turn-off snubber // IEEE Transactions on Power Electronics. — 2013. — Vol. 29, no. 8. — P. 4116–4125.

68. M. Safayatullah, I. Batarseh. Small Signal Model of Dual Active Bridge Converter for Multi-Phase Shift Modulation // 2020 IEEE Energy Conversion Congress and Exposition (ECCE). — Location TBD : IEEE, 2020. — P. 5960–5965.

69. Securing full-power-range zero-voltage switching in both steady-state and transient operations for a dual-active-bridge-based bidirectional electric vehicle charger / Y. Yan, H. Bai, A. Foote, W. Wang // IEEE Transactions on Power Electronics. — 2019. — Vol. 35, no. 7. — P. 7506–7519.

70. Lithium-ion battery aging mechanisms and life model under different charging stresses / Y. Gao, J. Jiang, C. Zhang, W. Zhang, Z. Ma, Y. Jiang // Journal of Power Sources. — 2017. — Vol. 356. — P. 103–114.

71. R. Abousleiman, A. Al-Refai, O. Rawashdeh. Charge capacity versus charge time in CC-CV and pulse charging of Li-ion batteries : tech. rep. / SAE Technical Paper. — 2013.

72. E. Ayoub, N. Karami. Review on the Charging Techniques of a Li-Ion Battery // 2015 Third International Conference on Technological Advances in Electrical, Electronics and Computer Engineering (TAEECE). — Location TBD : IEEE, 2015. — P. 50–55.

73. State-of-the-art review on soft-switching technologies for non-isolated DC-DC converters / X.-F. Cheng, C. Liu, D. Wang, Y. Zhang // IEEE Access. — 2021. — Vol. 9. — P. 119235–119249.

74. J.-H. Kim, I.-O. Lee, G.-W. Moon. Analysis and design of a hybrid-type converter for optimal conversion efficiency in electric vehicle chargers // IEEE Transactions on Industrial Electronics. — 2016. — Vol. 64, no. 4. — P. 2789–2800.

75. Half-bridge integrated phase-shifted full-bridge converter with high efficiency using center-tapped clamp circuit for battery charging systems in electric vehicles / C.-Y. Lim, Y. Jeong, M.-S. Lee, K.-H. Yi, G.-W. Moon // IEEE Transactions on Power Electronics. — 2019. — Vol. 35, no. 5. — P. 4934–4945.

76. TOPOLOGIES AND TECHNOLOGIES OF FAST CHARGING STATIONS FOR ELECTRIC VEHICLES: A REVIEW AND COMPARISON / H. Jassim, A. M. Zyuzev, A. V. Kostylev, M. V. Mudrov, A. I. Khabarov // Bulletin of Perm National Research Polytechnic University. Electrical engineering, information technology, control systems. — 2023. — No. 46. — P. 5–46.

77. C. Farkas, G. Szűcs, L. Prikler. Grid Impacts of Twin EV Fast Charging Stations Placed Alongside a Motorway // 2013 4th International Youth Conference on Energy (IYCE). — Location TBD : IEEE, 2013. — P. 1–6.

78. F. H. Malik, M. Lehtonen. Analysis of Power Network Loading Due to Fast Charging of Electric Vehicles on Highways // 2016 Electric Power Quality and Supply Reliability (PQ). — Location TBD : IEEE, 2016. — P. 101–106.

79. H. Jassim, M. Mudrov, A. Khabarov. Investigating the Operating Principles of Vehicle-to-Vehicle Charging // 2023 XIX International Scientific Technical Conference Alternating Current Electric Drives (ACED). — Location TBD : IEEE, 2023. — P. 1–6.

80. H. M. Jassim, A. Zyuzev, S. Valtchev. Analyzing G2V and V2G Functionalities for Electric Vehicle Charging Station // 2022 4th International Conference on Control Systems, Mathematical Modeling, Automation and Energy Efficiency (SUMMA). — Location TBD : IEEE, 2022. — P. 884–890.

81. An Application of the Multi-Port Bidirectional Three-Phase AC-DC Converter in Electric Vehicle Charging Station Microgrid / R. A. da Câmara, L. M. Fernández-Ramírez, P. P. Praça, D. d. S. Oliveira, P. García-Triviño, R. Sarrias-Mena // 2019 IEEE 15th Brazilian Power Electronics Conference and 5th IEEE Southern Power Electronics Conference (COBEP/SPEC). — Location TBD : IEEE, 2019. — P. 1–6.

82. R. Xiong, L. Li, J. Tian. Towards a smarter battery management system: A critical review on battery state of health monitoring methods // Journal of Power Sources. — 2018. — Vol. 405. — P. 18–29.

83. A comprehensive review of battery modeling and state estimation approaches for advanced battery management systems / Y. Wang, J. Tian, Z. Sun, L. Wang, R. Xu, M. Li, Z. Chen // Renewable and Sustainable Energy Reviews. — 2020. — Vol. 131. — P. 110015.

84. A. I. Maswood, F. Liu. A unity power factor front-end rectifier with hysteresis current control // IEEE transactions on Energy Conversion. — 2006. — Vol. 21, no. 1. — P. 69–76.

85. An improved active-front-end rectifier using model predictive control / M. Parvez, S. Mekhilef, N. M. Tan, H. Akagi // 2015 IEEE Applied Power Electronics Conference and Exposition (APEC). — Location TBD : IEEE, 2015. — P. 122–127.

86. Command generation for wide-range operation of hysteresis-controlled Vienna rectifiers / N. C. Foureaux, J. H. Oliveira, F. D. de Oliveira, B. d. J. Cardoso Filho, R. S. de Faria // IEEE Transactions on Industry Applications. — 2014. — Vol. 51, no. 3. — P. 2373–2380.

87. A novel hysteresis current control for three-phase three-level PWM rectifiers / L. Dalessandro, U. Drofenik, S. Round, J. W. Kolar // Twentieth Annual IEEE Applied Power Electronics Conference and Exposition, 2005. APEC 2005. Vol. 1. — IEEE, 2005. — P. 501–507.

88. Variable-frequency and phase-shift with synchronous rectification advance on-time hybrid control of LLC resonant converter for electric vehicles charger / J.-Y. Lin, H.-Y. Yueh, Y.-F. Lin, P.-H. Liu // IEEE Journal of Emerging and Selected Topics in Industrial Electronics. — 2022. — Vol. 4, no. 1. — P. 348–356.

89. A. Purvins, I. T. Papaioannou, L. Debarberis. Application of battery-based storage systems in household-demand smoothening in electricity-distribution grids // Energy conversion and management. — 2013. — Vol. 65. — P. 272–284.

90. A. Poullikkas. A comparative overview of large-scale battery systems for electricity storage // Renewable and Sustainable energy reviews. — 2013. — Vol. 27. — P. 778–788.

91. M. Chen, G. A. Rincon-Mora. Accurate electrical battery model capable of predicting runtime and IV performance // IEEE transactions on energy conversion. — 2006. — Vol. 21, no. 2. — P. 504–511.

92. Optimal charging of li-ion batteries via a single particle model with electrolyte and thermal dynamics / H. Perez, S. Dey, X. Hu, S. Moura // Journal of The Electrochemical Society. — 2017. — Vol. 164, no. 7. — A1679.

93. Electro-thermal analysis of Lithium Iron Phosphate battery for electric vehicles / L. Saw, K. Somasundaram, Y. Ye, A. Tay // Journal of Power Sources. — 2014. — Vol. 249. — P. 231–238.

94. Lithium iron phosphate based battery–Assessment of the aging parameters and development of cycle life model / N. Omar, M. A. Monem, Y. Firouz, J. Salminen, J. Smekens, O. Hegazy, H. Gaulous, G. Mulder, P. Van den Bossche, T. Coosemans, [et al.] // Applied Energy. — 2014. — Vol. 113. — P. 1575–1585.

95. O. Tremblay, L.-A. Dessaint, A.-I. Dekkiche. A generic battery model for the dynamic simulation of hybrid electric vehicles // 2007 IEEE Vehicle Power and Propulsion Conference. — IEEE, 2007. — P. 284–289.

96. E. Gómez-Luna, L. Palacios-Bocanegra, J. E. Candelo-Becerra. Real-time Simulation with OPAL-RT Technologies and Applications for Control and Protection Schemes in Electrical Networks. // Journal of Engineering Science & Technology Review. — 2019. — Vol. 12, no. 3.

97. Evaluation of system-integrated smart grid devices using software-and hardware-in-the-loop / B. Lundstrom, S. Chakraborty, G. Lauss, R. Bründlinger, R. Conklin // 2016 IEEE Power & Energy Society Innovative Smart Grid Technologies Conference (ISGT). — IEEE, 2016. — P. 1–5.

98. Real-time simulation technologies for power systems design, testing, and analysis / M. O. Faruque, T. Strasser, G. Lauss, V. Jalili-Marandi, P. Forsyth, C. Dufour, V. Dinavahi, A. Monti, P. Kotsampopoulos, J. A. Martinez, [et al.] // IEEE Power and Energy Technology Systems Journal. — 2015. — Vol. 2, no. 2. — P. 63–73.

99. F. Mocera. A model-based design approach for a parallel hybrid electric tractor energy management strategy using hardware in the loop technique // Vehicles. — 2020. — Vol. 3, no. 1. — P. 1–19.

100. A power hardware-in-the-loop based method for FAPR compliance testing of the wind turbine converters control / Z. Ahmad, J. R. Torres, N. Veera Kumar, E. Rakhshani, P. Palensky, M. Van Der Meijden // Energies. — 2020. — Vol. 13, no. 19. — P. 5203.

101. A. Ziuzev, H. M. Jassim. Power Hardware-in-Loop Implementation for Power Grids and Devices: Report and Review // 2021 XVIII International Scientific Technical Conference Alternating Current Electric Drives (ACED). — IEEE, 2021. — P. 1–6.

102. A review on the thermal hazards of the lithium-ion battery and the corresponding countermeasures / D. Ouyang, M. Chen, Q. Huang, J. Weng, Z. Wang, J. Wang // Applied Sciences. — 2019. — Vol. 9, no. 12. — P. 2483.

103. D. Lisbona, T. Snee. A review of hazards associated with primary lithium and lithium-ion batteries // Process safety and environmental protection. — 2011. — Vol. 89, no. 6. — P. 434–442.

104. H. M. Jassim, A. M. Zyuzev, M. V. Mudrov. Power hardware-in-loop emulation of a battery for charging systems and grid applications // Bulletin of the Tomsk Polytechnic University Geo Assets Engineering. — 2024. — Vol. 335, no. 4. — P. 200–211.

105. An advanced HIL simulation battery model for battery management system testing / J. V. Barreras, C. Fleischer, A. E. Christensen, M. Swierczynski, E. Schaltz, S. J. Andreasen, D. U. Sauer // IEEE Transactions on Industry Applications. — 2016. — Vol. 52, no. 6. — P. 5086–5099.

106. An Advanced Hardware-in-the-Loop Battery Simulation Platform for the Experimental Testing of Battery Management System / T. M. Bui, M. F. Niri, D. Worwood, T. Q. Dinh, J. Marco // 2019 23rd International Conference on Mechatronics Technology (ICMT). — IEEE, 2019. — P. 1–6.

107. Y. Li, Z. Sun, J. Wang. Design for Battery Management System Hardware-in-Loop Test Platform // 2009 9th International Conference on Electronic Measurement & Instruments. — IEEE, 2009. — P. 3–399.

108. Li-ion Battery Discharge Emulator Based on Three-Phase Interleaved DC-DC Boost Converter / R. Hidalgo-León, J. Urquizo, J. Litardo, P. Jácome-Ruiz, P. Singh, J. Wu // 2019 IEEE 39th Central America and Panama Convention (CONCAPAN XXXIX). — IEEE, 2019. — P. 1–6.

109. Design and implementation of a parametric battery emulator based on a power converter / R. Li, Y. Ji, Y. Fu, B. Hu, H. Hu // IET Electric Power Applications. — 2022. — Vol. 16, no. 11. — P. 1300–1316.

110. Z. Taylor, H. Akhavan-Hejazi, H. Mohsenian-Rad. Power Hardware-in-Loop Simulation of Grid-Connected Battery Systems with Reactive Power Control Capability // 2017 North American Power Symposium (NAPS). — IEEE, 2017. — P. 1–6.

111. C. Babu, S. Ashok. Optimal utilization of renewable energy-based IPPs for industrial load management // Renewable Energy. — 2009. — Vol. 34, no. 11. — P. 2455–2460.

112. A comprehensive review of standards for distributed energy resource grid-integration and microgrid / J. Shi, L. Ma, C. Li, N. Liu, J. Zhang // Renewable and Sustainable Energy Reviews. — 2022. — Vol. 170. — P. 112957.

113. Efficiency and energy-loss analysis for hybrid AC/DC distribution systems and microgrids: A review / S. Charadi, Y. Chaibi, A. Redouane, A. Allouhi, A. El Hasnaoui, H. Mahmoudi // International Transactions on Electrical Energy Systems. — 2021. — Vol. 31, no. 12. — e13203.

114. Up-to-date literature review on Solar PV systems: Technology progress, market status and R&D / A. Allouhi, S. Rehman, M. S. Buker, Z. Said // Journal of Cleaner Production. — 2022. — Vol. 362. — P. 132339.

115. S. Obukhov, A. Ibrahim, R. Aboelsaud. Maximum Power Point Tracking of Partially Shading PV System Using Particle Swarm Optimization // Proceedings of the 4th International Conference on Frontiers of Educational Technologies. — IEEE, 2018. — P. 161–165.

116. Sliding mode fixed frequency current controller design for grid-connected NPC inverter / F. Sebaaly, H. Vahedi, H. Y. Kanaan, N. Moubayed, K. Al-Haddad // IEEE Journal of Emerging and Selected Topics in Power Electronics. — 2016. — Vol. 4, no. 4. — P. 1397–1405.

117. K. Zuo, L. Wu. A review of decentralized and distributed control approaches for islanded microgrids: Novel designs, current trends, and emerging challenges // The Electricity Journal. — 2022. — Vol. 35, no. 5. — P. 107138.

118. Grid forming inverters: A review of the state of the art of key elements for microgrid operation / S. Anttila, J. S. Dohler, J. G. Oliveira, C. Bostr”om // Energies. — 2022. — Vol. 15, no. 15. — P. 5517.

119. L. F. A. Pereira, A. S. Bazanella. Tuning rules for proportional resonant controllers // IEEE Transactions on Control Systems Technology. — 2015. — Vol. 23, no. 5. — P. 2010–2017.

120. R. Aboelsaud, A. Ibrahim, A. G. Garganeev. Review of three-phase inverters control for unbalanced load compensation // International Journal of Power Electronics and Drive Systems. — 2019. — Vol. 10, no. 1. — P. 242.

121. M. Blej, M. Azizi. Comparison of Mamdani-type and Sugeno-type fuzzy inference systems for fuzzy real time scheduling // International Journal of Applied Engineering Research. — 2016. — Vol. 11, no. 22. — P. 11071–11075.

122. A. G. Garganeev, R. Aboelsaud, A. Ibrahim. Voltage Control of Autonomous Three-Phase Four-Leg VSI Based on Scalar PR Controllers // 2019 20th International Conference of Young Specialists on Micro/Nanotechnologies and Electron Devices (EDM). — IEEE, 2019. — P. 558–564.

123. H. Jassim, A. Zyuzev, A. Kostylev. Supervised Grid-Supporting Droop Controllers for Islanded Microgrid Operated by Scattered Parallel Inverters // 2023 XIX International Scientific Technical Conference Alternating Current Electric Drives (ACED). — IEEE, 2023. — P. 1–6.

124. Analysis on load-adaptive phase-shift control for high efficiency full-bridge LLC resonant converter under light-load conditions / J.-H. Kim, C.-E. Kim, J.-K. Kim, J.-B. Lee, G.-W. Moon // IEEE Transactions on Power Electronics. — 2015. — Vol. 31, no. 7. — P. 4942–4955.

125. Hybrid modulation of parallel-series *LLC* resonant converter and phase shift full-bridge converter for a dual-output DC–DC converter / G. Li, J. Xia, K. Wang, Y. Deng, X. He, Y. Wang // IEEE Journal of Emerging and Selected Topics in Power Electronics. — 2019. — Vol. 7, no. 2. — P. 833–842.

126. H. Wu, X. Zhan, Y. Xing. Interleaved LLC resonant converter with hybrid rectifier and variable-frequency plus phase-shift control for wide output voltage range applications // IEEE Transactions on Power Electronics. — 2016. — Vol. 32, no. 6. — P. 4246–4257.

127. S. Abdel-Rahman. Resonant LLC converter: Operation and design // Infineon Technologies North America (IFNA) Corp. — 2012. — Vol. 19, no. 4.

128. A. Sharma, S. Sharma. Review of power electronics in vehicle-to-grid systems // Journal of Energy Storage. — 2019. — Vol. 21. — P. 337–361.

129. MV and LV residential grid impact of combined slow and fast charging of electric vehicles / N. Leemput, F. Geth, J. Van Roy, P. Olivella-Rosell, J. Driesen, A. Sumper // Energies. — 2015. — Vol. 8, no. 3. — P. 1760–1783.

130. A control strategy for smart energy charging of warehouse material handling equipment / R. Carli, S. Digiesi, M. Dotoli, F. Facchini // Procedia Manufacturing. — 2020. — Vol. 42. — P. 503–510.

131. R. D. Lorenz, T. A. Lipo, D. W. Novotny. Motion control with induction motors // Proceedings of the IEEE. — 1994. — Vol. 82, no. 8. — P. 1215–1240.

132. B. K. Bose. Power electronics and AC drives // Englewood Cliffs. — 1986.

133. R. M. Prasad, M. A. Mulla. A novel position-sensorless algorithm for field-oriented control of DFIG with reduced current sensors // IEEE Transactions on Sustainable Energy. — 2018. — Vol. 10, no. 3. — P. 1098–1108.

134. S. R. Bolonne, D. Chandima. Sizing an energy system for hybrid li-ion battery-supercapacitor RTG cranes based on state machine energy controller // Ieee Access. — 2019. — Vol. 7. — P. 71209–71220.

135. K. B. Tawfiq, A. S. Mansour, P. Sergeant. Mathematical Design and Analysis of Three-Phase Inverters: Different Wide Bandgap Semiconductor Technologies and DC-Link Capacitor Selection // Mathematics. — 2023. — Vol. 11, no. 9. — P. 2137.

Appendix A

Particle Swarm Optimization

One of the metaheuristics optimization algorithms used to solve scientific problems and tune design parameters. This algorithm formulates the addressed sophisticated problem as multidimensional-nonlinear search space representing the design parameters and the evaluated cost. The objective of this algorithm is to minimize the cost by maximizing performance index. Based on the index, multiple solutions can be found for the same problem. The optimization is conducted based on virtual particles navigating through the search space. The general scheme of the PSO algorithm can be structured as follows:

- **Step1:** generate random initial locations of the particles based on the design parameters required to be tuned.
- **Step2:** evaluate the performance index and calculate the cost for each particle. This step may include simulation for the entire design based on the particle location.
- **Step3:** modify position and velocity of each particle based on the PSO general equations that differ depending on the utilized version of this method.
- **Step4:** re-evaluate the performance index for new particle location and velocity.
- **Step5:** iterate the algorithm between step 3 and 5, until the required performance is achieved or maximum iterations number is reached.

Appendix B

Three-Levels Four-Legs Converter

This converter commonly used in industrial applications where neutral line compensation is required. The fourth leg plays an important rule in regulating output power quality degradation caused by asymmetrical, unbalanced, and nonlinear loads. The multi-level design allowed smoother inverted output signal, while maintaining low voltage stress over switches.

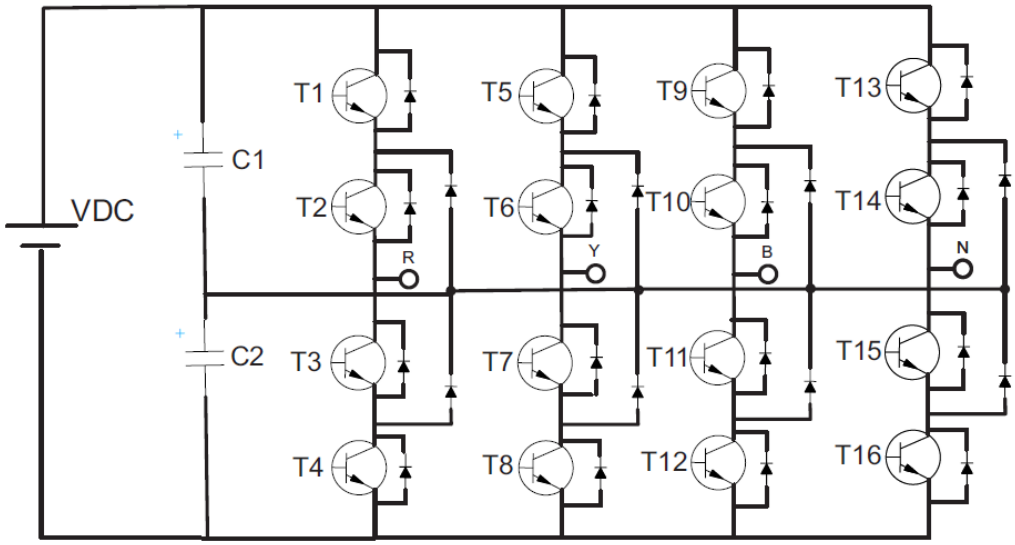

Figure B.1: Three-levels Four-legs converter.

Appendix C

DC/DC Converters Controllers

C.1 Variable Frequency Pulse Generator

C.2 Phase-Shift Function

This function receives current time, switching frequency, and the phase shift between legs of the converter. It produces the switching patterns of the input bridge transistors.

$function[PWM1, PWM2] = fcn(time, freq, phase)$
$PWM1 = 0;$
$PWM2 = 0;$
$swtchingtime = 1/freq;$
$y1 = mod(time, swtchingtime);$
$if y1 < swtchingtime/2$
$PWM1 = 1;$
end
$t - phase = swtchingtime * phase/360;$
$y2 = mod(time + t - phase, swtchingtime);$
$if y2 < swtchingtime/2$
$PWM2 = 1;$
end
end

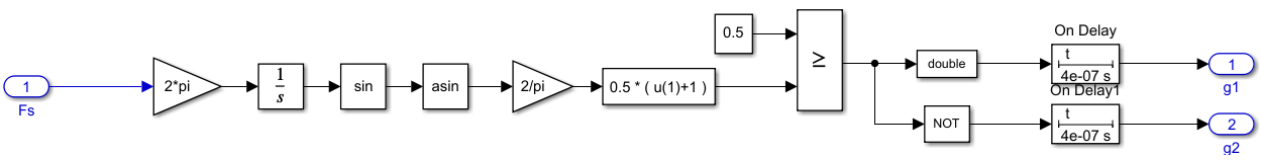

Figure C.1: Variable frequency Pulse Generator.

Appendix D

Wide Range LLC converter - Extra Results

In this appendix, extra simulated results of the phase-shift controlled resonant converter are presented. In chapter three, the test was conducted with a switching frequency of (52 kHz) which is slightly lower than resonant frequency. Figures D.1 and D.2 demonstrate that by further reducing the switching frequency, lower losses can be achieved by sacrificing output current range.

On the other hand, increasing the frequency higher than the resonant results in ex-

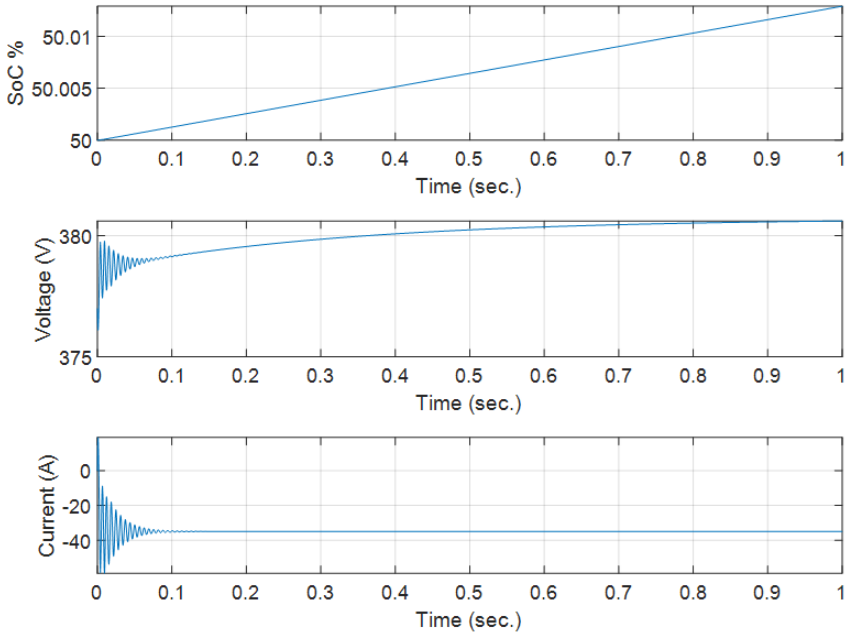

Figure D.1: Battery response of the converter operating at 40kHz.

tended current regulation range but escalates the losses level as seen in figures D.3 and D.4. The voltage and current switching states of one of the converter's transistors are shown in figure D.5. The top figure represents the (52kHz) frequency, the middle is the (40kHz) frequency, while the bottom is the (60kHz) switching-frequency. As seen in the figure, due to the extended negative value of the transistor current before voltage-on state, soft-switching is maintained. Whereas, the voltage current interactions in the bottom figure indicated increased hard-switching.

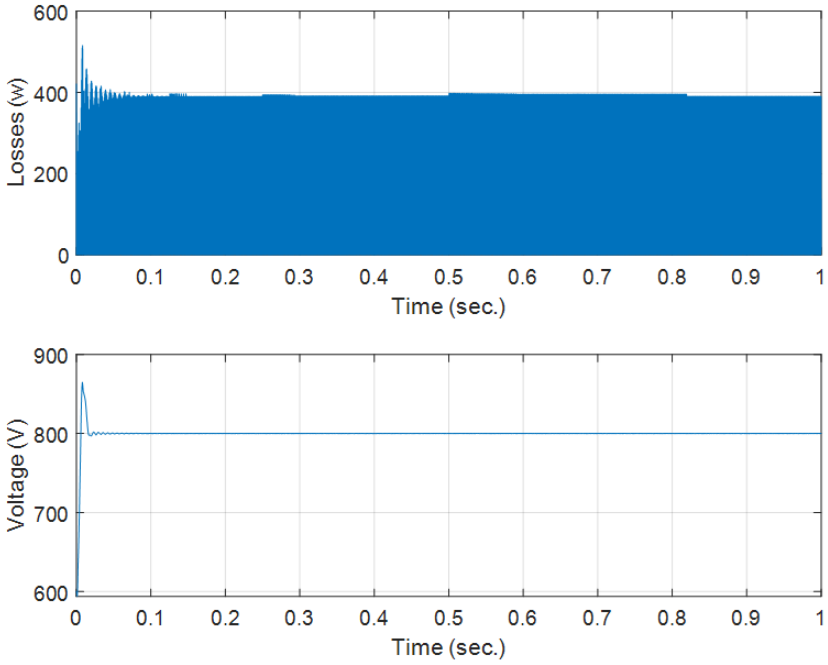

Figure D.2: Losses and DC voltage response at 40kHz.

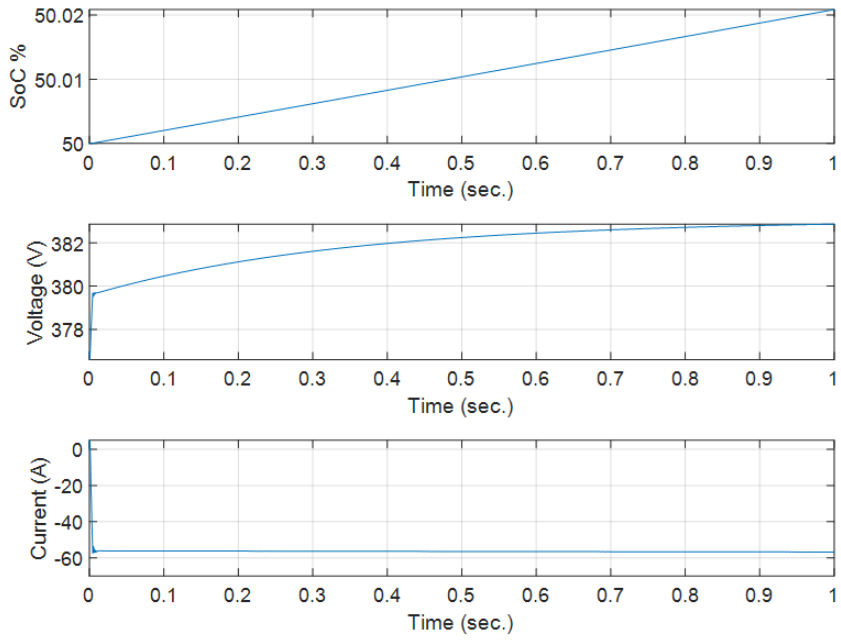

Figure D.3: Battery response of the converter operating at 60kHz.

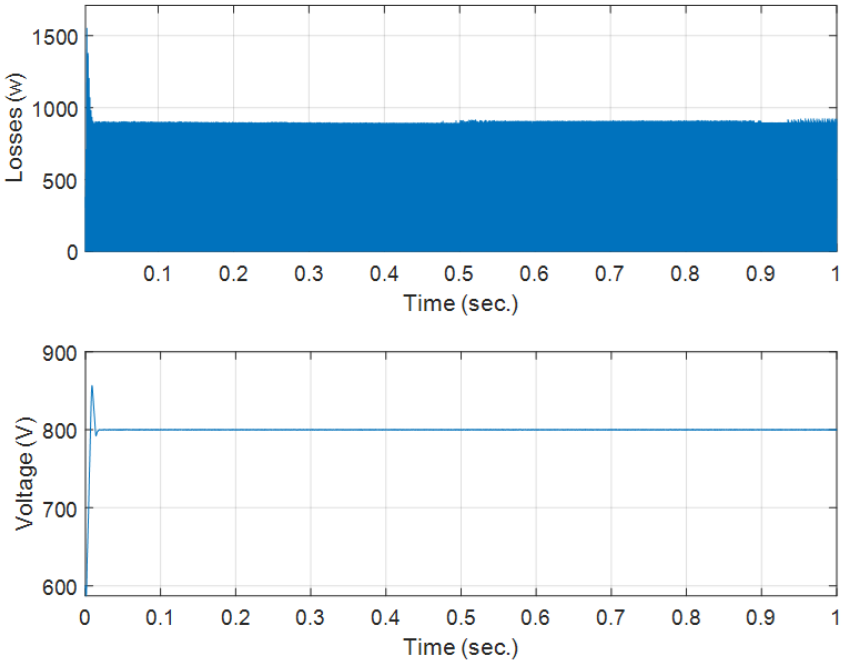

Figure D.4: Losses and DC voltage response at 60kHz.

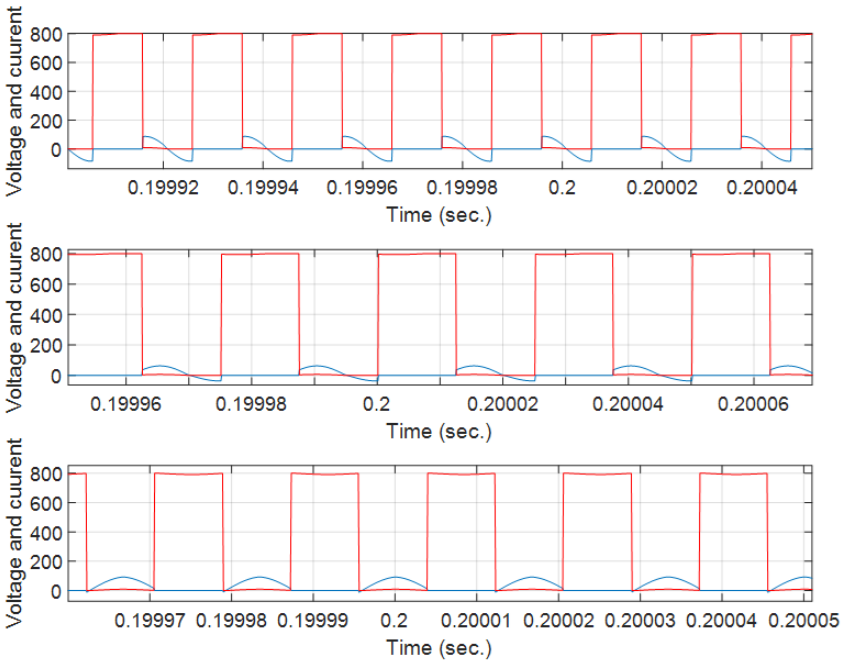

Figure D.5: upper-right transistor voltage and current.

Appendix E

Real-time LABVIEW-based Battery Model

РОССИЙСКАЯ ФЕДЕРАЦИЯ

СВИДЕТЕЛЬСТВО

о государственной регистрации программы для ЭВМ

№ 2024612062

Эмулятор аккумуляторной батареи в реальном времени.

Правообладатель: ***Федеральное государственное автономное образовательное учреждение высшего образования «Уральский федеральный университет имени первого Президента России Б.Н. Ельцина» (RU)***

Авторы: ***Зюзев Анатолий Михайлович (RU), Джассим Хайдер Майтам Джассим (IQ), Мудров Михаил Валентинович (RU)***

Заявка № **2024610308**

Дата поступления **15 января 2024 г.**

Дата государственной регистрации в Реестре программ для ЭВМ ***29 января 2024 г.***

Руководитель Федеральной службы по интеллектуальной собственности

ДОКУМЕНТ ПОДПИСАН ЭЛЕКТРОННОЙ ПОДПИСЬЮ
Сертификат 429b6a0fe3853364baf96f83b73b4aa7
Владелец Зубов Юрий Сергеевич
Действителен с 10.05.2023 по 02.08.2024

Ю.С. Зубов

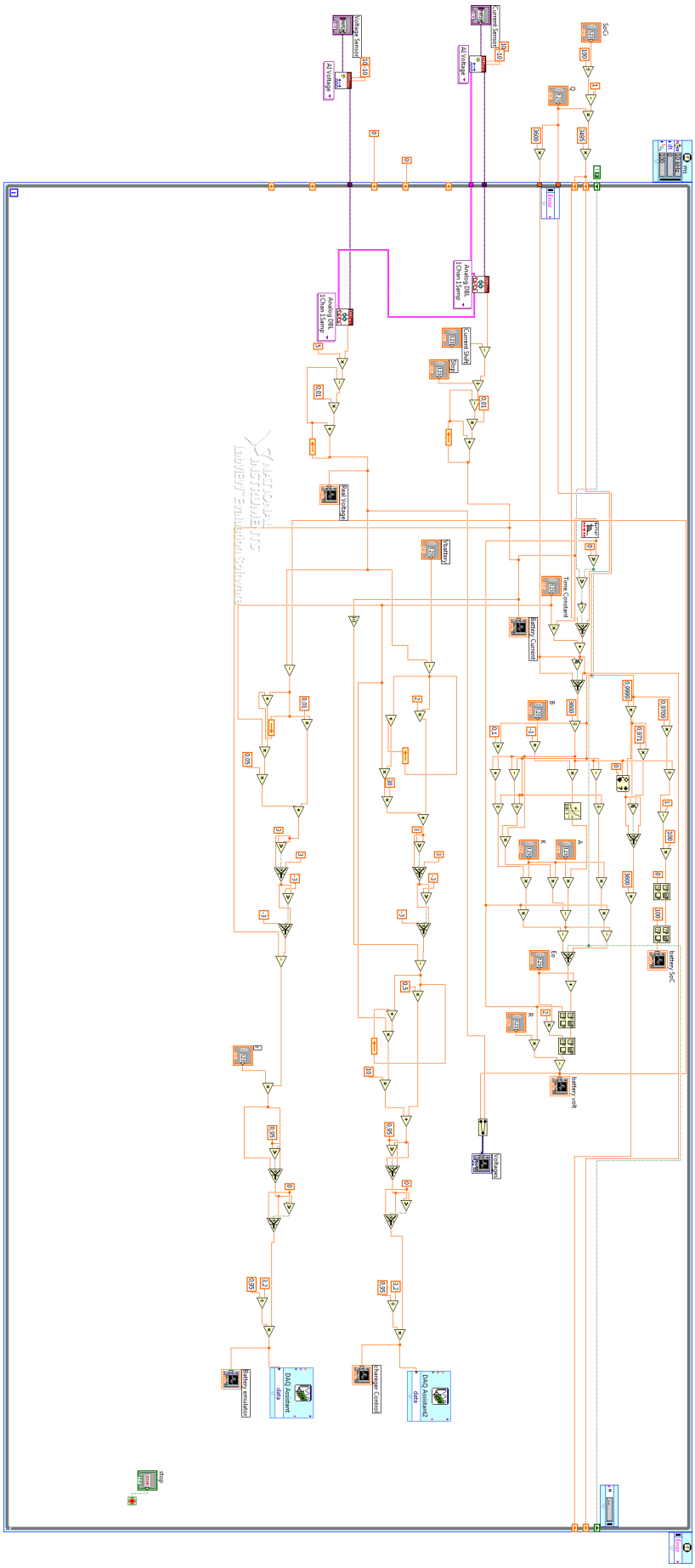

Figure E.1: Real-time battery model.

Appendix F

STM-Microcontroller Based Battery Model

РОССИЙСКАЯ ФЕДЕРАЦИЯ

СВИДЕТЕЛЬСТВО

о государственной регистрации программы для ЭВМ

№ 2024662960

Эмулятор аккумуляторной батареи на базе микроконтроллера STM32.

Правообладатель: ***Федеральное государственное автономное образовательное учреждение высшего образования «Уральский федеральный университет имени первого Президента России Б.Н.Ельцина» (RU)***

Авторы: ***Зюзев Анатолий Михайлович (RU), Джассим Хайдер Майтам Джассим (IQ), Вакорин Никита Иванович (RU), Мудров Михаил Валентинович (RU)***

Заявка № **2024661627**

Дата поступления **24 мая 2024 г.**

Дата государственной регистрации в Реестре программ для ЭВМ ***03 июня 2024 г.***

Руководитель Федеральной службы по интеллектуальной собственности

ДОКУМЕНТ ПОДПИСАН ЭЛЕКТРОННОЙ ПОДПИСЬЮ

Сертификат 429b6b0fe3653164baf96f83b73b4aa7

Владелец Зубов Юрий Сергеевич

Действителен с 19.05.2023 по 02.08.2024

Ю.С. Зубов

Appendix G

Additional Test-bench Results

This appendix demonstrates additional results representing the full charging cycle of the emulated battery in Chapter (4).

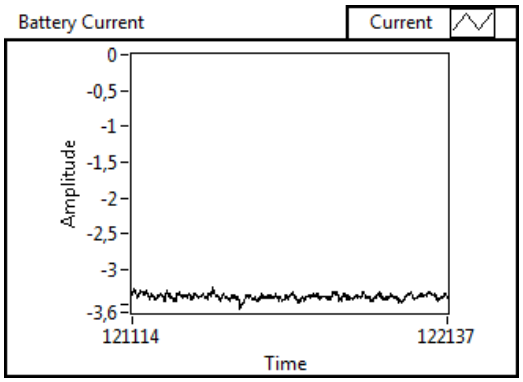

Figure G.1: Charging current 10%.

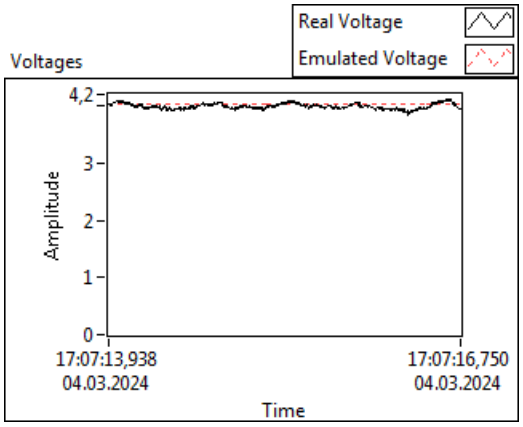

Figure G.2: Battery voltage 10%.

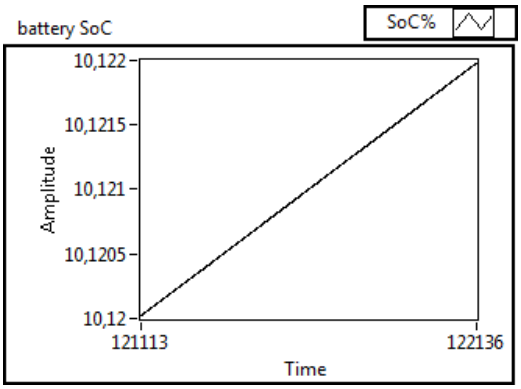

Figure G.3: Battery SoC 10%.

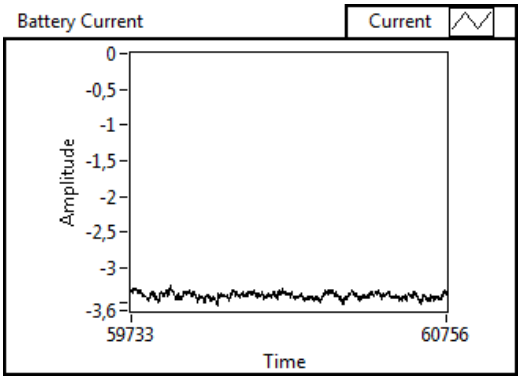

Figure G.4: Charging current 30%.

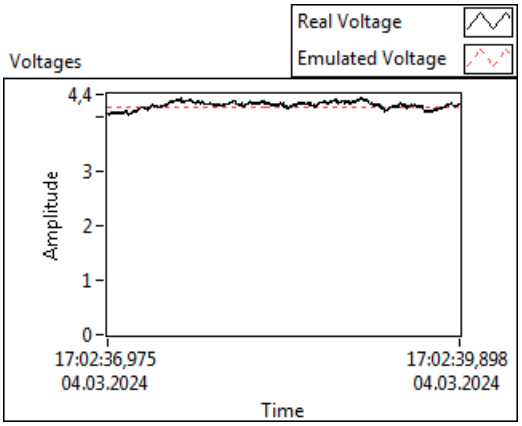

Figure G.5: Battery voltage 30%.

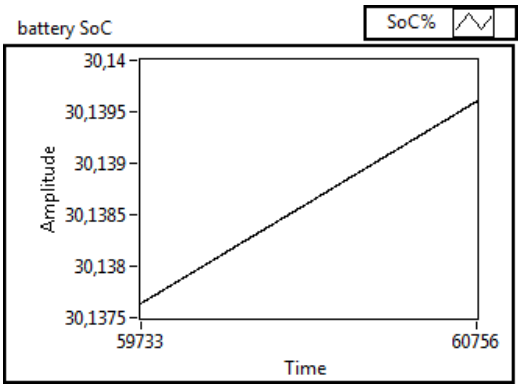

Figure G.6: Battery SoC 30%.

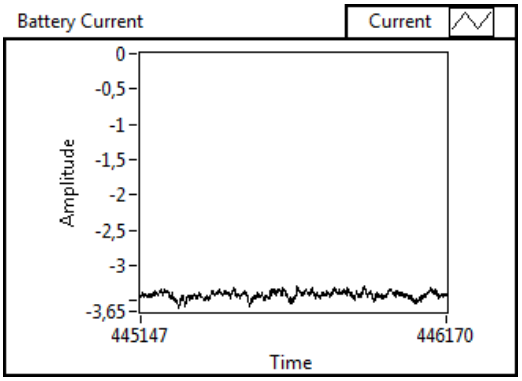

Figure G.7: Charging current 70%.

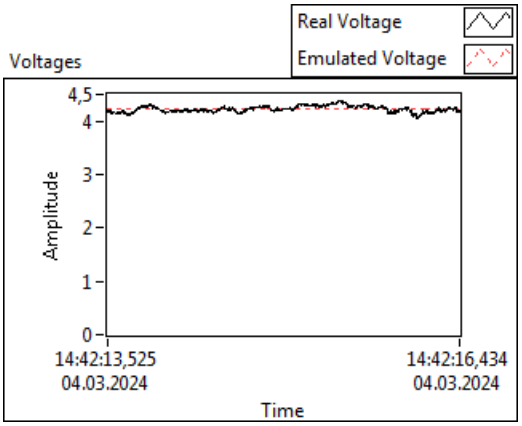

Figure G.8: Battery voltage 70%.

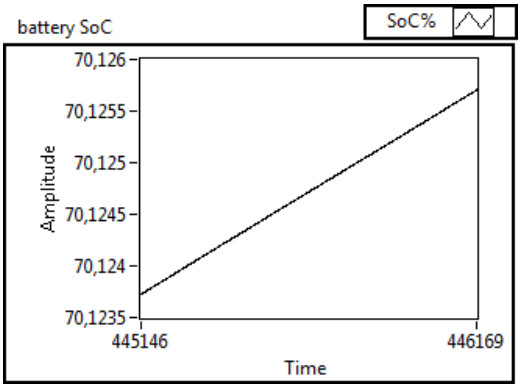

Figure G.9: Battery SoC 70%.

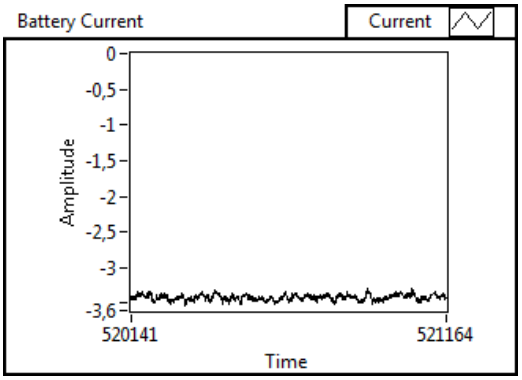

Figure G.10: Charging current 80%.

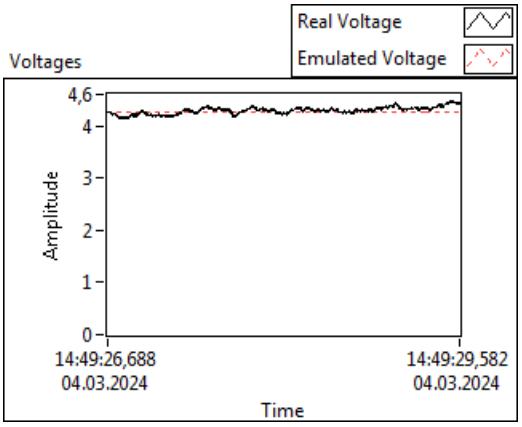

Figure G.11: Battery voltage 80%.

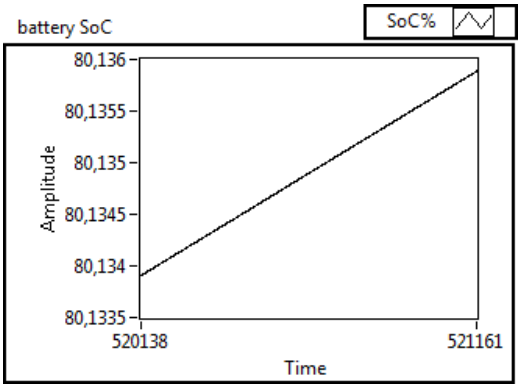

Figure G.12: Battery SoC 80%.

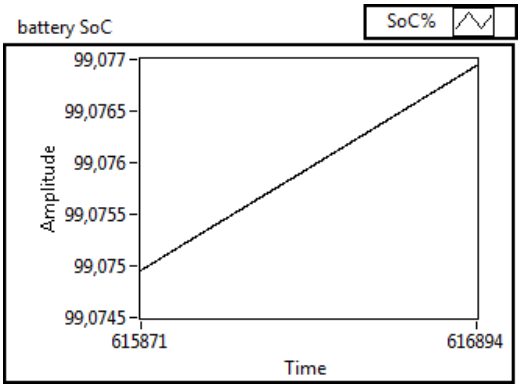

Figure G.13: Charging current 99%.

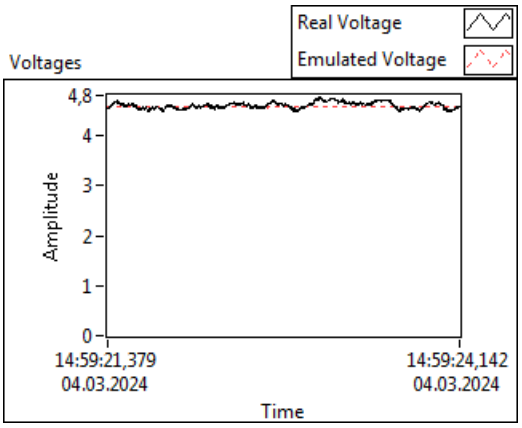

Figure G.14: Battery voltage 99%.

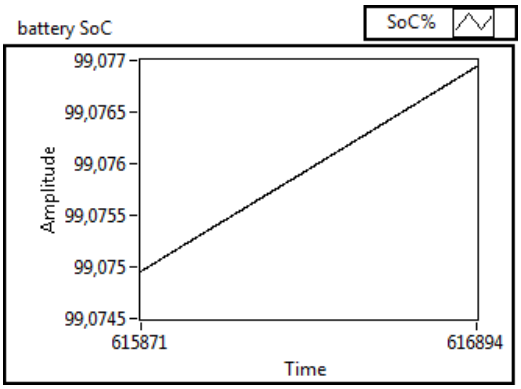

Figure G.15: Battery SoC 99%.

Appendix H

Real-time Battery Emulator Patent

РОССИЙСКАЯ ФЕДЕРАЦИЯ

ПАТЕНТ

НА ИЗОБРЕТЕНИЕ

№ 2837554

УСТРОЙСТВО ДЛЯ ИСПЫТАНИЙ ПОЛУПРОВОДНИКОВЫХ ПРЕОБРАЗОВАТЕЛЕЙ ЗАРЯДНЫХ УСТРОЙСТВ АККУМУЛЯТОРНЫХ БАТАРЕЙ

Патентообладатель: ***Федеральное государственное автономное образовательное учреждение высшего образования "Уральский федеральный университет имени первого Президента России Б.Н. Ельцина" (RU)***

Авторы: ***Зюзев Анатолий Михайлович (RU), Джассим Хайдер Майтам Джассим (RU), Мудров Михаил Валентинович (RU)***

Заявка № **2024120676**
Приоритет изобретения **23 июля 2024 г.**
Дата государственной регистрации
в Государственном реестре изобретений
Российской Федерации **01 апреля 2025 г.**
Срок действия исключительного права
на изобретение истекает **23 июля 2044 г.**

Руководитель Федеральной службы по интеллектуальной собственности

ДОКУМЕНТ ПОДПИСАН ЭЛЕКТРОННОЙ ПОДПИСЬЮ
Сертификат 0692e7d1a6300bf5442d0f670cca2026
Владелец Зубов Юрий Сергеевич
Действителен с 10.07.2024 по 03.10.2025

Ю.С. Зубов

Appendix I

Stacker Crane System - Additional

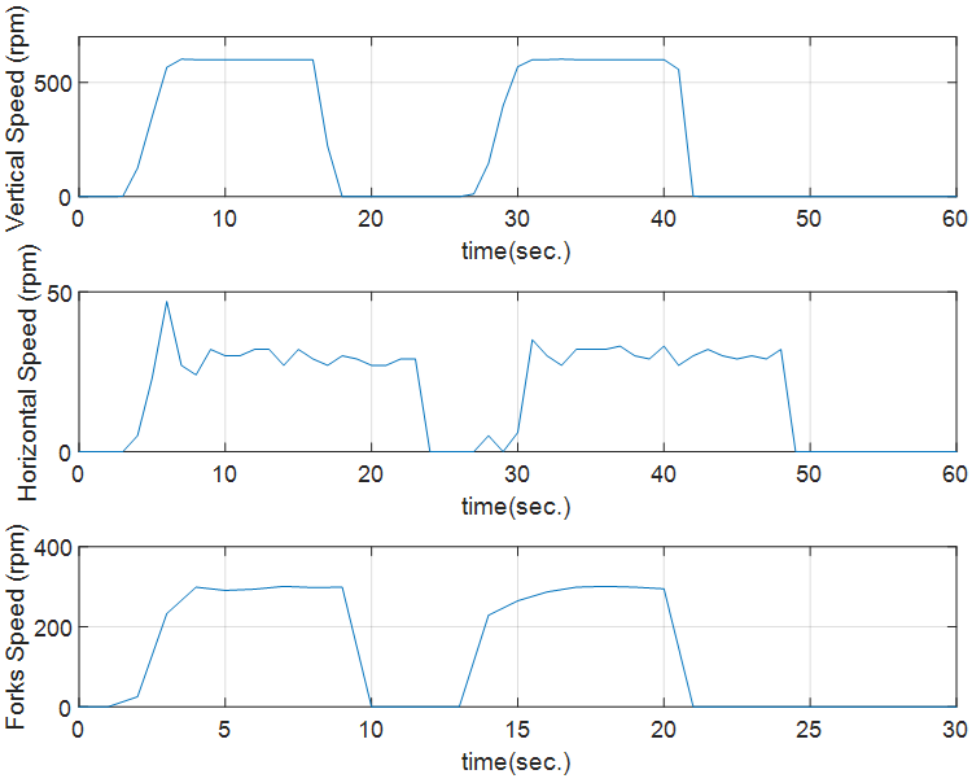

Figure I.1: Crane drive systems speeds.

Утверждаю:

Директор общества с ограниченной ответственностью «РУХЛО»

Вешкурцев Денис Анатольевич

АКТ

внедрения результатов диссертации
Хайдера Майтама Джассима
на соискание учёной степени кандидата технических наук по специальности 2.4.2 – Электротехнические комплексы и системы
«Разработка и исследование системы бесперебойного электроснабжения электроприводов подъемно-транспортных механизмов».

Под руководством и с непосредственным участием Джассима Х. М. разработана система электроснабжения автоматизированных кранов-штабелёров, производимых ООО «Рухло» для складских комплексов, основанная на технологиях «умных сетей» с применением аккумуляторных батарей и солнечных панелей, которая эффективно сохраняет энергию торможения электроприводов всех механизмов и способна поддерживать их длительное (до 4-х суток) питание во время отключений электроэнергии. На созданном Джассимом Х. М. экспериментальном стенде-эмуляторе аккумуляторной батареи показано, что отладку и испытания устройств зарядки аккумуляторных батарей можно выполнять без самой батареи, что повышает безопасность пуско-наладочных работ. Использование подобного стенда в условиях лаборатории позволило подтвердить преимущества предлагаемой системы электроснабжения без проведения натурных экспериментов на реальном объекте.

Предлагаемая Джассимом Х. М. система электроснабжения кранов-штабелёров принята отделом перспективных разработок компании ООО «Рухло» для дальнейшего внедрения в систему энергоснабжения механизмов кранов-штабелёров вновь проектируемых складских комплексов.

Генеральный директор ООО «Рухло» Д.А. Вешкурцев

25 февраля 2025 г.

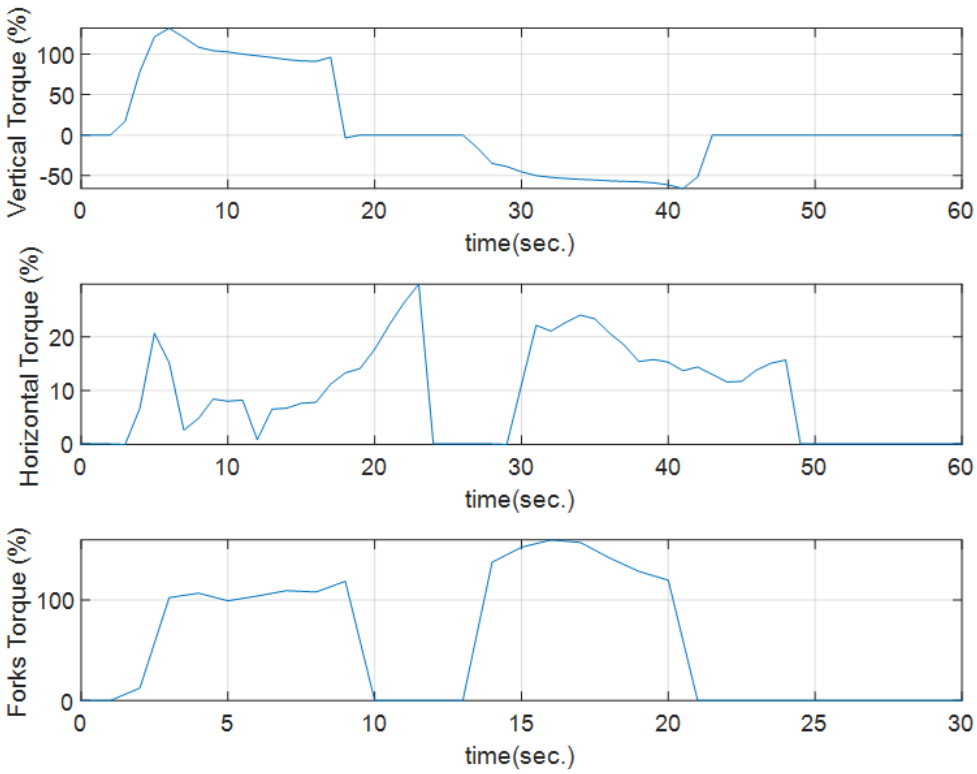

Figure I.2: Crane drive system torque.

Appendix J

Economic Viability of the Proposed Complex

In chapter five, the proposed battery integrated crane complex demonstrated effectiveness in autonomously supplying the system for extended periods. Regenerated braking energy can further extend the battery-supported power supply capacity and reduce system losses. In terms of energy, the following findings were obtained:

- Total energy consumption per one cycle: 476.85 kJ - 0.1325 kWh
- Average daily energy consumption: 13.25 kWh
- Total recovered regenerative energy per one cycle (Minimum assumption): 37.22 kJ - 0.01034 kWh
- Average daily recovered regenerative energy (Minimum assumption): 1.034 kWh
- Average daily consumption with the regenerative braking energy: 12.216 kWh

Inspecting the economic viability of the complex require calculating the return of investment (RoI) period. Considering the current average price of Lithium-ion battery system at $(115\$/kWh)$ provides a gross price of $(8,625\$)$ for the utilized (75 kWh) battery. The annual energy consumption without regenerative energy is determined as:

$$\begin{aligned} AnnualEnergy &= DailyEnergyConsumption * AnnualWorkingDays \\ &= 13.25kWh * 260 = 3445kWh \end{aligned} \tag{J.0.1}$$

While the annual complex consumption with the regenerated energy is:

$$\begin{aligned} AnnualEnergy_{+regen} &= (DailyEnergyConsumption - RecoveredEnergy) * AnnualWorkingI \\ &= 12.216kWh * 260 = 3176.16kWh \end{aligned} \tag{J.0.2}$$

The average annual saving is:

$$Energy^{saving}_{annual} = AnnualEnergy - AnnualEnergy_{withregenration} = 268.84kWh \tag{J.0.3}$$

If a minimum price of electricity is considered, according to the Russian market, at rate of $(0.1\$/kWh)$. Then the RoI is calculated as:

$$RoI = \frac{InitialInvestment}{Energy^{saving}_{annual} * 0.1\$} = 320.8years \tag{J.0.4}$$

This results indicates that the investment is not economically viable. Nevertheless, considering other factors like the energy independence, increased overall efficiency, and environmental benefits can justify the installation. Now, as in the fifth chapter, the integration of (72 kWh) solar energy sources is examined and costs are reevaluated. The current avarage cost of solar installation is (1000$perkW$), which gives a total initial investment of (72000$). The aggregated investment of both battery and solar systems becomes (80625 USD). Depending on the geographical location, Russian cities receive different irradiation intensities which results in variable peak generation of PV solar systems. If an average location is selected, 4 hours of peak energy generation is assumed. Thus, the daily solar energy, disregarding seasonal changes, is:

$$DailySolarEnergy = 72kWh * 4hours = 288kWh/day \tag{J.0.5}$$

The daily consumption of one crane working for an average of (100) cycles per day is (12.216 kWh/day) with regenerated braking energy recovery. The excess energy of the electrical complex can be calculated as:

$$ExcessEnergy = DailySolarEnergy - DailyConsumption = 275.784kWh/day \tag{J.0.6}$$

When the excess energy is employed in offsetting the grid electricity, the annual solar energy saving ASES can be calculated as:

$$ASES = 275.784kWh/day260days/year0.10USD/kWh = 7170.4USD/year \tag{J.0.7}$$

The total annual saving including the solar energy system and the regenerated energy is accumulated to (7196 USD/year). Therefore, the RoI coefficient is adjusted to be:

$$RoI = \frac{TotalInvestments}{AnnualSaving} = 11.2years \tag{J.0.8}$$

The results demonstrate colossal improvement as compared to the previous case which clearly indicate the economic viability of proposed electrical complex. Furthermore, the previous analysis did not consider the situation of dynamic pricing which can significantly improve the annual returns of the project. Aligning the peak price with the peak solar generation can obviously further justify the integration of solar energy to the warehouse complex.

The economic viability of the proposed design significantly affected by the system deployment geographical location and government policies. The previous calculations were conducted based on the Russian situation, however considering different country with higher annual irradiation can improve the results and provide more solid implantation justification. For example, considering the climate situation in Iraq with over 5 hours of maximum annual solar generation, can be extended to 6.5 hours during summer, implicates more excess daily energy generated by the electrical complex. Furthermore, the country has just adopted new policies to encourage investments in renewable energy and long term incentive programs for businesses that incorporate the local re-

newable generators. In addition to the increased energy market prices and the implantation of dynamic pricing policies, the feasibility and expected economic benefits of the proposed battery-integrated power supply system tremendously improve.